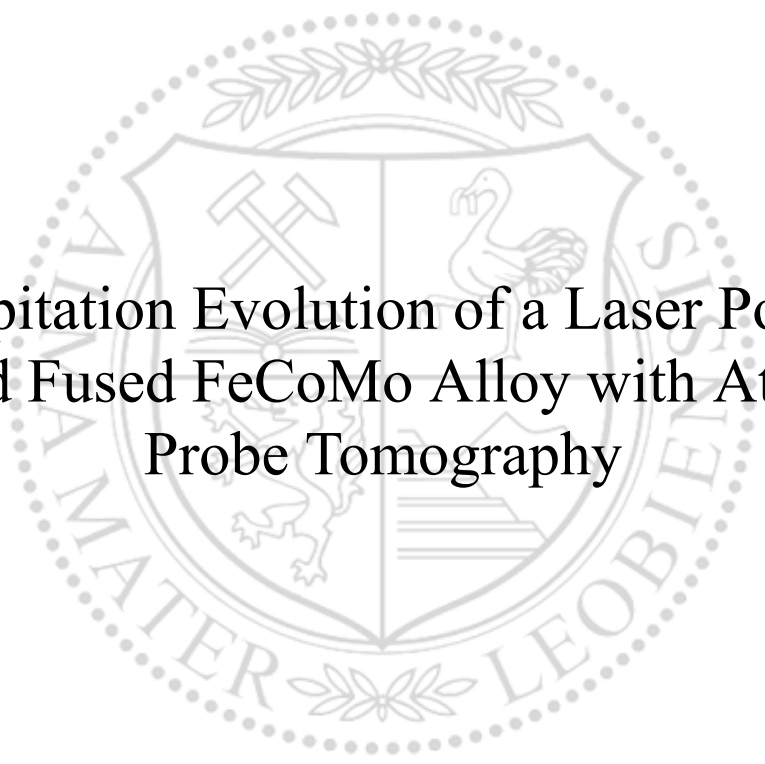




Chair of Design of Steels

Master's Thesis



Precipitation Evolution of a Laser Powder
Bed Fused FeCoMo Alloy with Atom
Probe Tomography

Charlotte Cui, BSc

September 2021



EIDESSTÄTTLICHE ERKLÄRUNG

Ich erkläre an Eides statt, dass ich diese Arbeit selbständig verfasst, andere als die angegebenen Quellen und Hilfsmittel nicht benutzt, und mich auch sonst keiner unerlaubten Hilfsmittel bedient habe.

Ich erkläre, dass ich die Richtlinien des Senats der Montanuniversität Leoben zu "Gute wissenschaftliche Praxis" gelesen, verstanden und befolgt habe.

Weiters erkläre ich, dass die elektronische und gedruckte Version der eingereichten wissenschaftlichen Abschlussarbeit formal und inhaltlich identisch sind.

Datum 08.09.2021

Unterschrift Verfasser/in
Charlotte Cui

Acknowledgements

I want to thank Univ.-Prof. Dr. mont. Ronald Schnitzer for providing and reviewing this thesis and for monitoring its course.

Dipl.-Ing. Jan Platl for supervising this thesis, being the first point of contact, giving useful advice and spending late nights at the FIB together.

Special thanks to Dr. mont. Harald Leitner, whose guidance and support helped overcome several obstacles in the course of this thesis. The conversations, brainstorming and mentoring are deeply appreciated.

Dr. mont. Christina Hofer for sharing her APT-expertise and setting time aside to review and discuss the analysis.

I wish to thank the Department Materials Science in general and the following people in particular for their help: Dr. Francisca Mendez Martin, Gerhard Hawranek and Silvia Pözl.

I wish to express my gratitude to Dr. mont. Christoph Turk and the entire R&D department at voestalpine Böhler Edelstahl GmbH, Kapfenberg, who provided this thesis and accompanied me through the course of my studies.

Abstract

During the fabrication of a FeCoMo alloy with laser powder bed fusion (LPBF), cracks are formed in the material. Coarse grains due to epitaxial growth, the brittle *Fe-Co* ordering phase, in-situ precipitation of the strengthening μ -phase and/or embrittlement by *Si*-oxides were identified as possible reasons for cracking. In this thesis, the nanostructure of the LPBF FeCoMo alloy was studied with atom probe tomography (APT). Two as-built conditions were investigated: one without in-process platform preheating and one with a preheating temperature of 500 °C. The results showed that *Mo* and impurity elements segregated to interdendritic spaces during solidification in LPBF and formed *Mo*-rich chain-like structures in the APT reconstruction. These structures were also observed with scanning electron microscopy SEM, but they could not be characterised due to the limited spatial resolution of a SEM. The *Mo*-segregations were partially dissolved by an intrinsic heat treatment (IHT) during LPBF.

The precipitation behaviour during LPBF was investigated for the two conditions. When no preheating was applied, no precipitation occurred, however early stages of spinodal decomposition were observed. It is known that spinodal decomposition is the first stage of precipitation in the investigated FeCoMo alloy. With in-process platform preheating, various stages of precipitation were present in the as-built condition, from spinodal decomposition to early stages of particle growth. As a result, the hardness of as-built specimens increased with incremental distance from the top layer. The existence of precipitates in the preheated condition is also in agreement with preceding differential scanning calorimetry (DSC) measurements. Dilatometer measurements showed that no precipitation occurs from the austenite phase, hence the microstructure during LPBF was (at least partially) martensitic. In order to take into account the temperature increase at the tip apex during laser-APT and to depict the geometry of precipitates more accurately in the APT reconstruction, k_f was adjusted based on a tip profile-based reconstruction using a scanning electron microscopy (SEM) image. As no precipitation occurred without in-process preheating during LPBF and the as-built specimen still cracked during the process, μ -phase precipitation is not the main reason for the cracking of the FeCoMo alloy during LPBF.

With SEM, *Si*-oxides were observed to be homogeneously dispersed in the matrix. In APT, nm-sized *Si*-oxides were found, which exhibited a spherical geometry after k_f was adjusted. These *Si*-oxides could be one reason for cracking.

Kurzfassung

Während der Fertigung einer FeCoMo Legierung mit dem Laser Pulverbett Verfahren (engl. Laser Powder Bed Fusion, LPBF) bilden sich Risse im Material. Als mögliche Rissursachen wurden grobe Körner aufgrund epitaktischen Wachstums, die spröde *Fe-Co* Ordnungsphase, in-situ Ausscheidung der Festigkeitssteigernden μ -Phase und/oder Versprödung durch *Si*-Oxide identifiziert. In dieser Arbeit wurde die Nanostruktur der LPBF gefertigten FeCoMo Legierung mit 3D Atomsondentomographie (engl. Atom Probe Tomography, APT) untersucht. Zwei as-built Zustände wurden betrachtet: Einer, bei dem das Pulver auf einer ungeheizten Plattform additiv gefertigt wurde und einer, bei dem eine Plattformheizung von 500 °C verwendet wurde. *Mo* und Verunreinigungselemente segregierten in interdendritischen Bereichen während der Erstarrung im LPBF Verfahren und bildeten *Mo*-reiche kettenförmige Strukturen in der APT Rückkonstruktion. Diese Strukturen wurden auch mit dem Rasterelektronenmikroskop (REM) beobachtet, konnten jedoch wegen seiner bedingten räumlichen Auflösung nicht charakterisiert werden. Die *Mo*-Segregationen wurden während der intrinsischen Wärmebehandlung (engl. Intrinsic Heat Treatment, IHT) im LPBF Verfahren aufgelöst.

Das Ausscheidungsverhalten während dem LPBF-Prozess wurde für beide Zustände untersucht. Ohne Plattformheizung bildeten sich keine Ausscheidungen in der Probe, jedoch wurden Anfangsstadien der spinodalen Entmischung beobachtet. Es ist bekannt, dass spinodale Entmischung das erste Stadium der Ausscheidungsbildung in der untersuchten FeCoMo Legierung ist. Wenn jedoch die Plattform während des Prozesses beheizt wurde, waren unterschiedliche Stadien der Ausscheidungsbildung im as-built Zustand vorhanden, von spinodaler Entmischung bis zu frühen Stadien des Partikelwachstums. Folglich nahm die Härte der as-built Proben mit zunehmendem Abstand von der letzten Lage zu. Das Vorhandensein von Ausscheidungen und deren Vorstufen stimmt mit Ergebnissen der dynamischen Differenzkalorimetrie (engl. Differential Scanning Calorimetry DSC) überein. Dilatometermessungen zeigten, dass es zu keiner Ausscheidungsbildung in der Austenitphase kommt. Daraus wurde geschlossen, dass die Mikrostruktur während des LPBF-Prozesses (zumindest teilweise) martensitisch war. Um die Erwärmung der Spitze während der Laser-Messung zu berücksichtigen und die wahre Geometrie der Ausscheidungen realitätsnahe darzustellen, wurde k_f in der APT Rückkonstruktion angepasst. Der angepasste Wert für k_f wurde aus einer Rückkonstruktion basierend auf dem Spitzenprofil in einem REM Bild abgeleitet. Da sich ohne Plattformheizung keine Ausscheidungen während dem LPBF-Prozess bildeten und die Probe im as-built Zustand trotzdem Risse aufwies, ist die μ -Phasenbildung nicht der Hauptgrund für die Rissbildung der FeCoMo Legierung während LPBF. Mit dem REM wurden homogen in der Matrix verteilte *Si*-Oxide beobachtet. Mit APT wurden auch nm-große *Si*-Oxide gefunden. Nachdem k_f angepasst wurde, wiesen diese Oxide eine kugelige Form auf. Diese *Si*-Oxide könnten auch eine Rissursache sein.

Abbreviations

AM	additive manufacturing
APT	atom probe tomography
BSE	back-scattered electron(s)
DSC	differential scanning calorimetry
FIB	focused ion beam
HIP	hot isostatic pressing
HSS	high-speed steel
IHT	intrinsic heat treatment
LEAP	local electrode atom probe
LOM	light optical microscopy
LPBF	laser powder bed fusion
KNN	K-th nearest neighbour
PH	precipitation hardening
PM	powder metallurgy
PSD	precipitate size distribution
Q&T	quenched and tempered
ROI	region of interest
SDM	spatial distribution mapping
SE	secondary electron(s)
SEM	scanning electron microscopy
TOF	time of flight
VED	volumetric energy density

Contents

Acknowledgements	i
Abstract	ii
Kurzfassung	iii
Abbreviations	iv
1 Introduction	1
2 Theoretical background	4
2.1 Carbide-strengthened tool steels	4
2.2 Intermetallic-strengthened maraging steels	4
2.2.1 Ni-maraging steels	5
2.2.2 FeCoMo(W) alloys	6
2.3 Additive manufacturing	11
2.3.1 Laser powder bed fusion	12
2.3.2 Directional solidification in LPBF	13
2.3.3 Residual stresses in LPBF parts	14
2.3.4 LPBF of maraging steels	15
2.4 Atom probe tomography	16
2.4.1 Measurement principle	17
2.4.2 Local electrode atom probe	21
2.4.3 Specimen geometry	22
2.4.4 Physical conditions at the specimen tip	24
2.4.5 Specimen preparation	26
2.4.6 Data processing and 3D reconstruction	29
2.4.7 Potential measurement errors and corrective measures	31
3 Experimental	35
3.1 Investigated material	35
3.2 Heat treatment variations and hardness measurement	35
3.3 Microstructure and hardness of as-built specimens	36
3.4 Preparation of as-built specimens for APT	38
3.4.1 Electrolytic preparation	38
3.4.2 FIB preparation	39
3.5 APT measurement of as-built specimens	40
3.6 APT reconstruction and analysis	40
3.6.1 Spatial distribution mapping	42
3.6.2 Cluster search	43

3.6.3	Tip profile-based reconstruction from SEM image	44
3.7	Dilatometer measurements	45
4	Results	47
4.1	Microstructure and hardness	47
4.2	APT analysis of as-built specimens	51
4.3	Comparison of precipitation behaviour using dilatometry	58
5	Discussion	60
6	Conclusions	68
7	Outlook	70
	References	71
	Appendix	75

1 Introduction

Additive manufacturing (AM) allows the fabrication of complex geometries that need hardly any post-processing or can be used in the as-built condition directly after the manufacturing process. AM was developed for polymers in the 1980's and has been recently made available for metals, ceramics and composite materials. For steels, AM has great potential, especially for tooling applications. One of the most commonly used AM methods for metals is the laser powder bed fusion (LPBF) process. The ability to build complex geometries with LPBF can, for instance, be used to build surface-near cooling channels in tools to provide enhanced cooling conditions [1, 2].

The investigated FeCoMo alloy is used for cutting applications in its conventionally manufactured condition. Fully heat treated, the alloy exhibits a hardness of ~ 70 HRC, which is owed to the precipitation of intermetallic nm-sized μ -phases during the ageing treatment. Intermetallic phases have a higher temper resistance than secondary hardening carbides in high- C steels, which allows their application at higher service temperatures. Therefore, the investigated FeCoMo alloy is used as high speed steel (HSS), as the surface temperature of the tool can reach up to 600°C during cutting or drilling applications [3–7].

Although the low C -content of the investigated FeCoMo alloy and its moderate hardness (~ 40 HRC) in the as-built condition suggest good printability, the specimens fail during the LPBF process due to crack formation, see figure 1 a). Cracking during LPBF of the investigated FeCoMo alloy occurs whether in-process platform preheating is applied or not. Upon closer examination, the crack formation stems from transgranular brittle fracture, as shown in figure 1 b). Since the origin of brittle fracture cannot be identified on the fracture surface, the cause for these cracks cannot be directly found. However, the cracks are located near the surface, which suggests their formation at the specimen surface and propagation orthogonally to the building direction (see figure 1 a)).

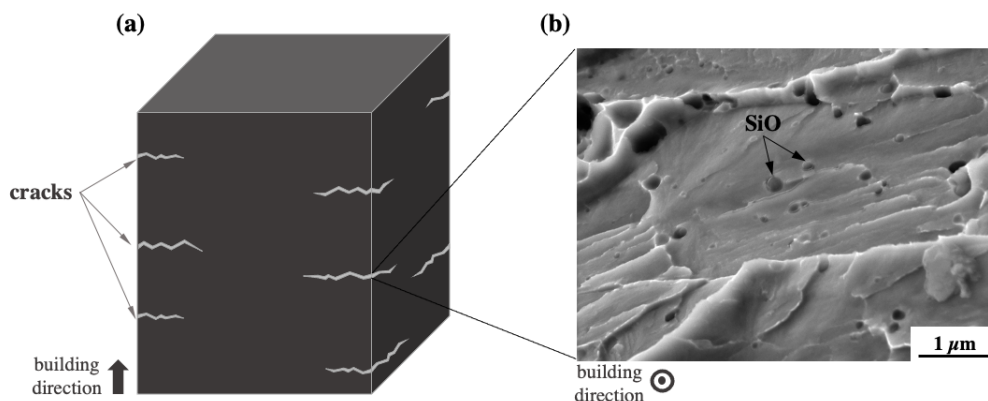


Figure 1: (a) LPBF specimen sketch with schematic cracks (building platform is not depicted). (b) SEM micrograph of a fracture surface with globular SiO particles.

1 Introduction

The formation of the brittle ordering phase, *Si*-oxides, coarse grains from epitaxial growth and in-situ precipitation were identified as potential causes for cracking.

Differential scanning calorimetry (DSC) measurements were carried out in the course of a previous bachelor thesis [8] to determine whether ordering phase and precipitates were present in the material. Conventional slow-cooled (SC) and water-quenched (WQ) samples, AM-powder and LPBF samples with (AM500) and without (AMRT) preheating were investigated. The SC sample represents a condition close to the equilibrium (i.e. ordered), while the WQ sample constitutes a highly disordered state, as the ordering reaction needs a sufficient amount of time. The heat flow graphs for various heating rates (5, 10 and 20 K/min) from that thesis are shown in figure 1 a–c. The peaks I–IV indicate phase transformations. I is associated with the disordering transition of *Fe* and *Co*. II is related to *Mo*-diffusion and clustering, which occurs previous to III, the μ -phase formation. IV indicates the coarsening of μ -phase particles. The disordering peak I was only found in the SC-sample. This indicates the absence of the brittle B2 *Fe-Co* ordering phase in as-built FeCoMo specimens with and without platform preheating, hence the ordering phase is not responsible for cracking. For the AM500 sample, *Mo* diffusion was initiated at higher temperatures than in the AMRT sample and the corresponding DSC-peak (II) was less distinct. This led to the assumption that *Mo*-rich domains have already formed during the LPBF process with platform preheating.

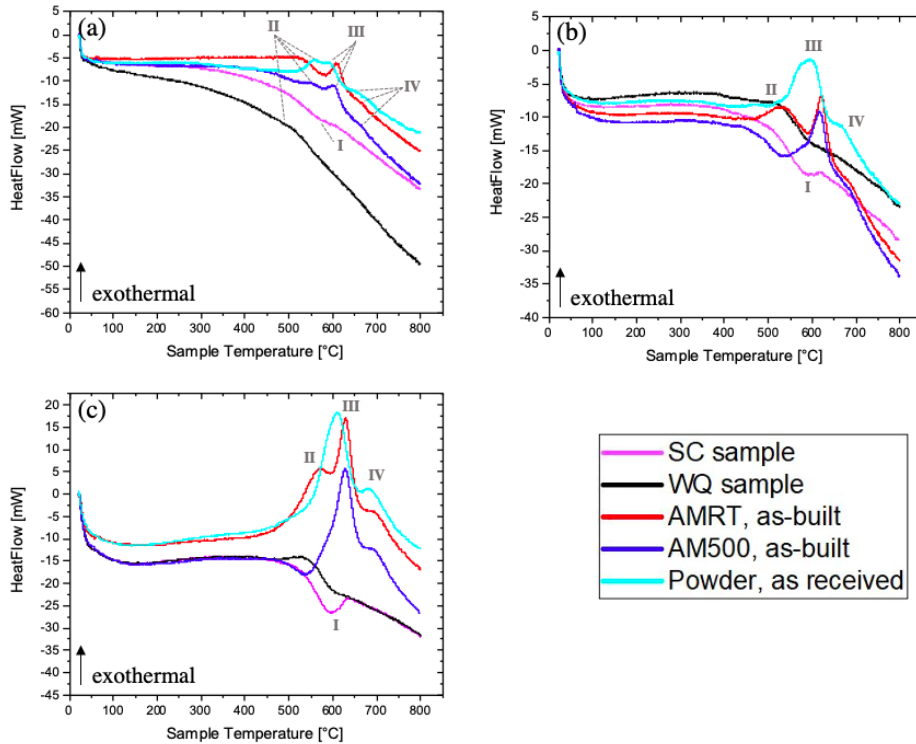


Figure 2: DSC measurements for different samples and heating rates: (a) 5 K/min, (b) 10 K/min and (c) 20 K/min [8].

1 Introduction

With SEM, (sub-)micrometer-sized *Si*-oxide particles were found homogeneously dispersed in the matrix, and also on the fracture surfaces (see figure 1 b). Since oxides are notoriously brittle, they might be the reason for the transgranular fracture during LPBF. However, the small size and globular shape of the *Si*-oxide particles, in addition to their uniform distribution in the rather soft matrix (*N300* as-built: ~ 40 HRC, see table 6 in the appendix) leave room for scepticism regarding their criticality.

Another feature of the additively manufactured FeCoMo alloys microstructure were coarse, elongated grains oriented parallelly to the building direction, i.e. direction of heat flow. The grains extended across several weld bead layers. The coarseness of the grains may also trigger transgranular fracture.

From these four potential causes for brittle fracture, i.e. ordering phases, coarse grains, *Si*-oxides and in-situ precipitation, the former two have been studied in the course of the aforementioned bachelor thesis [8]. The precipitation formation in as-built specimens will be investigated in this thesis. Due to the small size of these precipitates, their chemical composition is inaccessible with electron microscopy techniques, such as energy or wavelength dispersive spectroscopy. 3D atom probe tomography (APT) is a powerful tool to overcome these limitations. The analysis with APT has two main advantages over electron microscopy techniques. Firstly, it allows the examination of a specimen volume rather than a 2D projection of it. Secondly, it provides atomic-scale resolution with a detection limit down to a few ppm. Hence, APT is a popular tool for the investigation of early-stage precipitates in maraging steels and *Al*-alloys. However, the examined volume in APT is very small and extrapolation to large volumes must be done carefully. Therefore, APT and electron microscopy are often used complementary [4, 5].

The aim of this thesis is to analyse the precipitate evolution during LPBF of the investigated FeCoMo steel with APT and correlate the nanostructure to its macroscopic hardness properties in order to gain a deeper understanding of the influence of precipitation reaction on crack formation.

2 Theoretical background

2.1 Carbide-strengthened tool steels

Tool steels are, amongst other applications (e.g. hot forming), used for machining and therefore need to exhibit special properties such as high hardness and wear resistance. There is a common separation of tool steels into three categories: cold work tool steels for applications with surface temperatures below 200 °C, hot work tool steels for applications with surface temperatures higher than 400 °C and HSS for highly demanding applications such as drilling and milling, where surface temperatures of the tool can reach up to 600 °C [3]. In order to provide a hard matrix, tool steels undergo a quenching and tempering (Q&T) heat treatment. While all carbide-strengthened tool steels have a C -martensitic matrix after completed heat treatment, the demand for varying mechanical and thermal properties of the three categories is met by different alloying concepts. Cold work tool steels are typically used for low-temperature cutting applications, which call for high primary hardness and wear resistance. Coarse primary carbides of the MC -type with $M = V, Mo, W$ and M_6C -type carbides with $M = Mo, W, Fe, Cr$ provide for these properties. In hot work tool steels, fine secondary hardening carbides are formed during tempering and result in elevated temper resistance compared to cold work tool steels. Typical secondary hardening carbides comprise of M_2C and MC with $M = Mo, Cr, V$. Lastly, HSS combine both wear and temper resistance. Hence, they contain primary and secondary hardening carbides. The alloying of Co to HSS provides additional solid solution strengthening, which results in higher temper resistance. Moreover, Co lowers the solubility of W and Mo in the martensitic matrix and therefore enhances the formation potential of secondary hardening carbides, which increases the secondary hardness maximum [3, 7, 9, 10].

2.2 Intermetallic-strengthened maraging steels

Unlike C -tool steels, this steel group is not hardened by C but by the precipitation of intermetallic phases. Precipitation hardening (PH) is one of the most effective mechanisms to achieve high strengths in alloys. The precipitation of intermetallic compounds during heat treatment is secondary (i.e. they precipitate from solid solutions), hence they are finer than primary carbides in conventional C -steels that form during solidification. With appropriate particle size, dislocation movement is hindered significantly. The intermetallic strengthening effect is stronger than in carbide-strengthened steels (i.e. higher hardness). C -contents in intermetallic-strengthened steels are kept as low as it is commercially practicable. Intermetallic precipitates provide a higher tempering resistance than the secondary carbides in C -tool steels, which allows them to serve at higher temperatures. Their high-temperature hardness makes intermetallic strengthened steels especially attractive for applications as HSS for e.g. drilling or milling, where surface temperatures can reach up to 600 °C [3, 4, 6, 7, 11].

In contrast to high- C tool steels, no change in volume due to lattice distortion occurs during quenching of intermetallic strengthened steels, so no severe internal stresses are developed. Additionally, the softness of these steels after solution annealing minimises the danger of distortion or cracking. However, the large amount of alloying elements (especially Ni and Co) in maraging steels makes them more expensive than conventional C -tool steels [4, 6, 11].

2.2.1 Ni-maraging steels

The most commonly used type of intermetallic-strengthened steels are Ni -maraging steels, which are a class of high strength steels ($\sigma_s \approx 2000$ MPa, 18Ni300). The name *maraging* refers to the conventional heat treatment of these steels, which intends ageing of a martensitic microstructure. The so-called soft-martensite in maraging steels is obtained rather easily at ordinary cooling rates (i.e. no rapid quenching necessary). The martensite transformation is owed to the high contents of Ni and/or Co . In contrast to C -martensite, this martensite is not tetragonally distorted and therefore softer, but highly dislocated. The final hardness and strength are subsequently attained by an ageing heat treatment (several hours at $480 - 510$ °C [4]), during which intermetallic phases precipitate and dense, fine and complex microstructures are formed. In later ageing stages, metastable martensite decomposes, but the peak hardness is attained before it transforms into ferrite and austenite. Overageing decreases strength, ductility and toughness, but there have been reports of increased toughness due to reverted austenite [4]. The precipitation process and the identification of precipitates have been the focus of previous studies for the development of maraging steels with APT commonly used for the analysis. Maraging steels are weldable under inert gas shielding without pre-heat or post-heat stress relieving treatments, though the solution annealing and ageing treatment must be repeated to harden the weld and the heat affected zone [4, 6, 7, 11]. Within the category of Ni -maraging steels, there is a distinction between Co -free and Co -containing grades. Commercially available Co -containing maraging steels comprise of ~ 18 wt.% Ni , $3 - 5$ wt.% Mo , $8 - 13$ wt.% Co , $0.2 - 1.5$ wt.% Ti and 0.1 wt.% Al , the exact amount of which depends on the desired strength [4].

After solution annealing and air cooling, Ni -maraging steels exhibit a lath martensitic microstructure with no noticeable retained austenite between the laths. An increase in Ni -content provides a higher dislocation density in the martensite matrix. The hardness in this state is ~ 30 HRC for both low- and high- Mo steels. The longer the solution annealing time or the higher the temperature, the coarser the resulting lath martensite, but there is no residual austenite, regardless of the solution annealing temperature and time. In Co -free maraging steels, the η - Ni_3Ti precipitate is the main hardening phase. In the early stages of low-temperature ageing (440 °C), extremely fine Ni_3Ti precipitates ($\varnothing 2 - 3$ nm) grow in Co -free maraging steels. These precipitates coalesce into needle- or rod-shape along the $\langle 111 \rangle_M$ direction with increasing ageing time and exhibit high coarsening resistance at low and intermediate ageing temperatures ($440 - 480$ °C). At later stages of intermediate-temperature ageing, reverted austenite starts to

2 Theoretical background

form at martensite lath boundaries. High-temperature ageing ($> 500\text{ }^\circ\text{C}$) facilitates inhomogeneous Ni_3Ti -precipitation, followed by rapid and severe coarsening. At later ageing stages, these precipitates dissolve and form reverted austenite. Maraging grades with higher Ti -contents (up to 2.6 wt.%) form coarse $Fe_2(Mo, Ti)$ precipitates ($\varnothing 120\text{ nm}$ after ageing at $480\text{ }^\circ\text{C}$ for 3 hours) along the martensite lath boundaries. These precipitates have no coherency or orientation relationship with the matrix and are detrimental for the toughness of the material, as microvoids and microcracks may easily form around them. In Co -containing grades (10.8 and 14.8 wt.%, respectively), there is an increase in the amount of $Ni_3(Mo, Ti)$ precipitates, but there is no precipitation of coarse $\mu-(Fe, Co)_7Mo_6$, $\sigma-Fe_2Mo$ or Ni_4Mo , which might decrease their toughness [4].

2.2.2 FeCoMo(W) alloys

FeCoMoW alloys are a group of maraging steels that exhibit higher hardness and higher thermal stability than C -HSS. The intermetallic compounds in these FeCoMoW alloys start to dissolve at $900\text{ }^\circ\text{C}$ in the austenite phase but a small fraction remains undissolved even at $1300\text{ }^\circ\text{C}$ and inhibits grain growth. The transformation during rapid cooling is martensitic with no precipitation of intermetallics. A FeCoMoW steel with $< 0.2\text{ wt.}\% C$ and $< 0.2\text{ wt.}\% Cr$ contains no retained austenite after quenching and has a hardness of 32 – 38 HRC. During ageing at $500 - 550\text{ }^\circ\text{C}$, disperse intermetallics begin to precipitate. Peak hardness is attained with ageing at $580 - 600\text{ }^\circ\text{C}$ (68 – 69 HRC). FeCoMoW steels have the highest thermal stability (up to $720\text{ }^\circ\text{C}$) attainable in HSS, which can be explained by two effects. Firstly, the A1 transformation temperature ($900 - 950\text{ }^\circ\text{C}$) is $\sim 100\text{ }^\circ\text{C}$ higher than in carbide-strengthened steels and secondly, there is a pronounced strengthening effect of precipitates during ageing. Consequently, the hot hardness of FeCoMoW alloys is higher than of carbide-strengthened steels. At $600\text{ }^\circ\text{C}$, FeCoMoW alloys maintain a hardness of 67 HRC, which reduces to 54 HRC at $700\text{ }^\circ\text{C}$ (compared to 59 and 30 HRC, respectively for C -HSS Grade P18($\sim X80WCrV18-4-1$)). Due to their high hardness and outstanding thermal stability, FeCoMoW alloys are used for turning, cutting and milling of materials that are difficult to machine (e.g. Ti -alloys and austenitic steels). The lifetime for these applications is 30 – 40 times that of Co -free C -HSS and 10 – 20 times that of C -HSS containing Co . This advantage of FeCoMoW alloys over C -based tool steels is depicted in figure 3 with hardness–tempering charts of FeCoMoW alloys, C -HSS, cold work and hot work tool steels [7, 9].

W and Mo induce precipitation hardening and are almost entirely transferred into the intermetallic compound in the equilibrium state that forms after several hours of ageing. Both elements virtually have the same effect on the A1 transformation temperature and on the stability of intermetallic particles against coalescence. Therefore, W and Mo have the same effect on secondary hardness and thermal stability. A combined ($W + Mo$)-content of 17 – 18 wt.%

2 Theoretical background

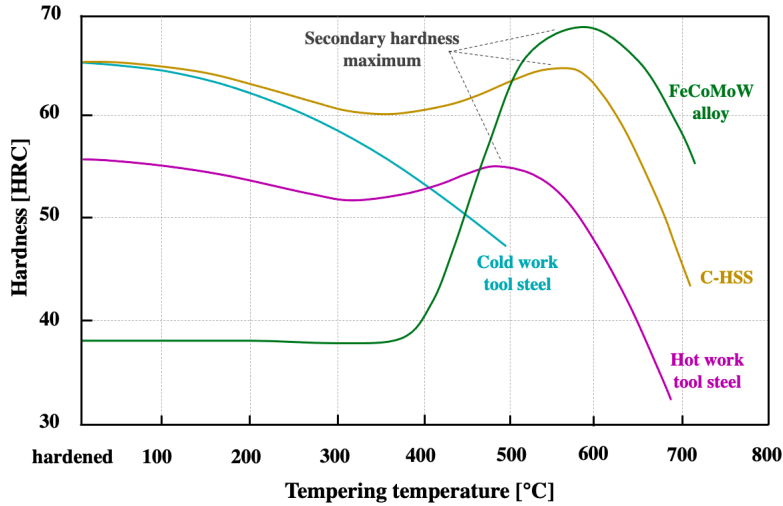


Figure 3: Schematic hardness–tempering diagrams of FeCoMoW alloys, C-HSS, cold work and hot work tool steels (cf. [7, 9]).

results in maximum hardness and thermal stability. Further additions, however, do not improve these properties, but the toughness decreases due to the increasing amount of intermetallic compounds. With a Mo/W ratio > 1 , intermetallic precipitates become smaller in size, which has a favourable effect on the mechanical properties. While a fraction of Co forms $(Fe, Co)_7(W, Mo)_6$ precipitates, the remainder may cause austenitisation. Co -contents of less than 20 wt.% retain the martensitic microstructure at high temperatures, due to the α -stabilising effect of W and Mo . With more than 23–24 wt.% Co , the amount of intermetallic compound increases, which impairs the mechanical properties. C -impurities have no effect on the transformation temperatures, but the presence of 0.15–0.23 wt.% C may facilitate the formation of M_6C carbides along with the intermetallic compound. These carbides are less thermally stable than $(Fe, Co)_7(W, Mo)_6$ and result in a lower hardness, thermal stability and impaired cutting properties [7].

The investigated alloy contains no additions of W . The desire for an alloy with exceptionally high hardness drove the development of the investigated FeCoMo alloy and the alloy design was based on the advantages of spinodal decomposition. The mechanism of spinodal decomposition will be briefly outlined at this point. In infinite, isotropic, defect-free solids, the spinodal $\left(\frac{\partial^2 G}{\partial c^2}\right)_{T,P} = 0$ marks the limit of metastability of solid-solution to infinitesimal concentration fluctuations. Within this spinodal, an initially homogeneous solid solution is unstable to such a fluctuation and there is no nucleation barrier. It is therefore a state that lies between unstable and metastable states. When an alloy is heated to a homogeneous, single-phase field at high temperatures and then quenched to a state within the spinodal, spinodal decomposition occurs everywhere within the sample, although the rate may be different near a structural imperfection. Initial phase separation occurs with a well-defined spatial periodicity and adheres to the lever rule. The amplitude and wavelength of this periodic concentration fluctuations grows

2 Theoretical background

continuously, until a metastable equilibrium is reached [12–15]. Hence, a fine and homogeneous microstructure evolves in spinodally decomposed alloys and this mechanism can be used for the adjustment of properties in steels with high hardness. The advancing stages of spinodal decomposition are schematically shown in figure 4.

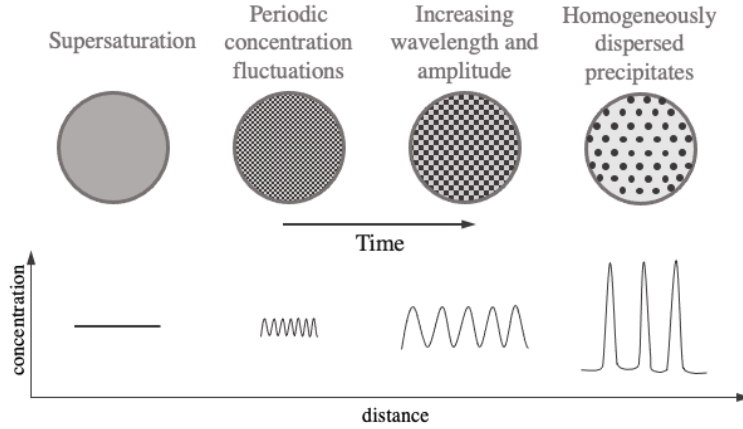


Figure 4: Schematic depiction of the advancing stages of spinodal decomposition according to Cahn [12, 13, 16].

Spinodal decomposition occurs in the *Fe-Mo* binary system. In early ageing-stages of a *Fe-20 Mo* (at.%), a typical modulated structure along the $\langle 100 \rangle$ type directions was observed by Miyazaki *et al.* [17]. These structures are caused by coherent spinodal decomposition. With further ageing, the periodicity of *Mo*-rich and -poor regions disappears and a stable λ -phase (Fe_2Mo) is formed. However, a minimum *Mo*-content of 17 at.% (26 wt.%) is necessary to cause spinodal decomposition. Such high *Mo*-contents cause severe embrittlement of the alloy. Hence, Doi *et al.* [18] sought to expand the spinodal region towards lower *Mo*-contents by alloying a third element. The requirement for that third element is a negative interchange energy with *Fe*, i.e. forming an ordered structure in the equilibrium state. *Co* and *V* exhibit suitable properties [18, 19], however only *Fe-Co-Mo* ternary alloys will be illustrated further in this section. Figures 5 a–c show the binary edges of the ternary *Fe-Co-Mo* system [20, 21]. The ordering transition of the *Fe-Co* system from α to α' in the thermodynamic equilibrium is visualised in figure 5 b. This B2-ordered phase causes embrittlement of the material. According to Sha *et al.* [4], the presence of the disordered phase at room temperature provides good ductility properties. Köster *et al.* [22] investigated the mechanical properties of ternary *FeCoMo* alloys with varying compositions. Figures 5 d–g depict the phase diagrams at varying *Mo*-contents from their study. They found that with increasing *Mo*-content, the hardness of the material increased, but at the expense of ductility. Further investigations by Danninger *et al.* [11] concluded that alloys with *Fe-25 Co-15 Mo* (wt.%) and *Fe-20 Co-15 Mo* (wt.%) for less demanding applications (e.g. slower cutting speed) are the most promising for high-speed cutting. Based on the above-mentioned promising conclusions, a lot of research effort has been made to

2 Theoretical background

study an $Fe-25Co-15Mo$ (wt.%) alloy, in which the intermetallic $(Fe, Co)_7Mo_6$ μ -phase precipitates during ageing. Figure 5 h shows the isothermal ternary $Fe-Co-Mo$ diagram at $1200^\circ C$. Figure 5 i depicts the Fe -rich corner with the calculated spinodal lines. “X” marks the composition of the investigated alloy in figures 5 h and i. This alloy is used for cutting applications as HSS due to its high tempering resistance and high hardness (~ 70 HRC) in the fully heat treated condition. Both phenomena are accounted for by the μ -phase, which is a mixture between the Co_7Mo_6 and the Fe_7Mo_6 intermetallic phases that form in the respective binary systems (see figures 5 a and c). Besides the aforementioned benefits of Co , its addition also increases the defect-density after solution annealing. These defects, namely dislocations and point-defects, act as nucleation sites for precipitation. Closer proximity of such nuclei shortens the diffusion paths of Mo . Co also lowers the solubility of Mo in the matrix, which encourages the precipitation of μ -phase and results in a higher maximum hardness of up to 70 HRC [3, 7, 11, 23].

The high alloying content in the investigated FeCoMo alloy calls for high cooling rates in the manufacturing process to avoid segregations. Powder metallurgy (PM) has proven to be a suitable processing route for high-alloyed steels, yielding homogeneous microstructures. The conventional manufacturing route consists of inert gas powder atomisation, followed by hot isostatic pressing (HIP) and a two-step heat treatment similar to maraging steels (see figure 6 a) [3, 4, 23]. In the first step, the alloy is solution annealed in the austenite region ($1150 - 1220^\circ C$) in order to homogenise the microstructure and dissolve primary μ -phase particles ($\varnothing 1 \mu m$ [5]) that have formed during solidification. Due to the solution of the μ -phase, the austenite matrix enriches in Mo and austenite grain coarsening is facilitated. The remaining primary μ -phase particles have diameters of $1 - 2 \mu m$. Because their diameter is in the same range as the plastic zone of the material, they facilitate brittle fracture [23]. Therefore, the solution annealing temperature is chosen as high as possible, in order to minimise the volume fraction of primary μ -phase particles. The formation of δ ferrite above $1280^\circ C$ poses restrictions on the annealing temperature, because it reduces the ductility, hardness and strength of the material [23, 25–27]. The solution annealing treatment yields a Mo supersaturated Co martensite, which is rather soft. In order to provide the Mo supersaturation, fast cooling rates are necessary. Moreover, the formation of the B2-ordered $Fe-Co$ phase and μ -phase formation at grain boundaries is suppressed by accelerated cooling [23]. The second heat treatment step, i.e. ageing, facilitates PH, which consists of two subsequent mechanisms and is schematically depicted in figure 25 b. First, spinodal decomposition of Mo occurs in the supersaturated matrix at low aging temperatures or short ageing times and Mo -rich clusters are the result. At higher ageing temperatures or longer ageing times, μ -phase particles are formed. The size of μ -phase particles in the hardness maximum is typically about 10 nm. Due to the fact that the μ -phase is formed from spinodally decomposed Mo clusters, the nm-sized μ -phase precipitates are homogeneously dispersed in the matrix and form a sponge-like structure. If the alloy is further aged at higher temperatures or longer times after the μ -phase formation, the precipitates start to coarsen (i.e. overageing), which results in a decrease in hardness, see figure 25 b. The residual Mo content in the matrix decreases towards zero, which results in an overaged matrix that resembles the binary system of 71 at.% Fe and

2 Theoretical background

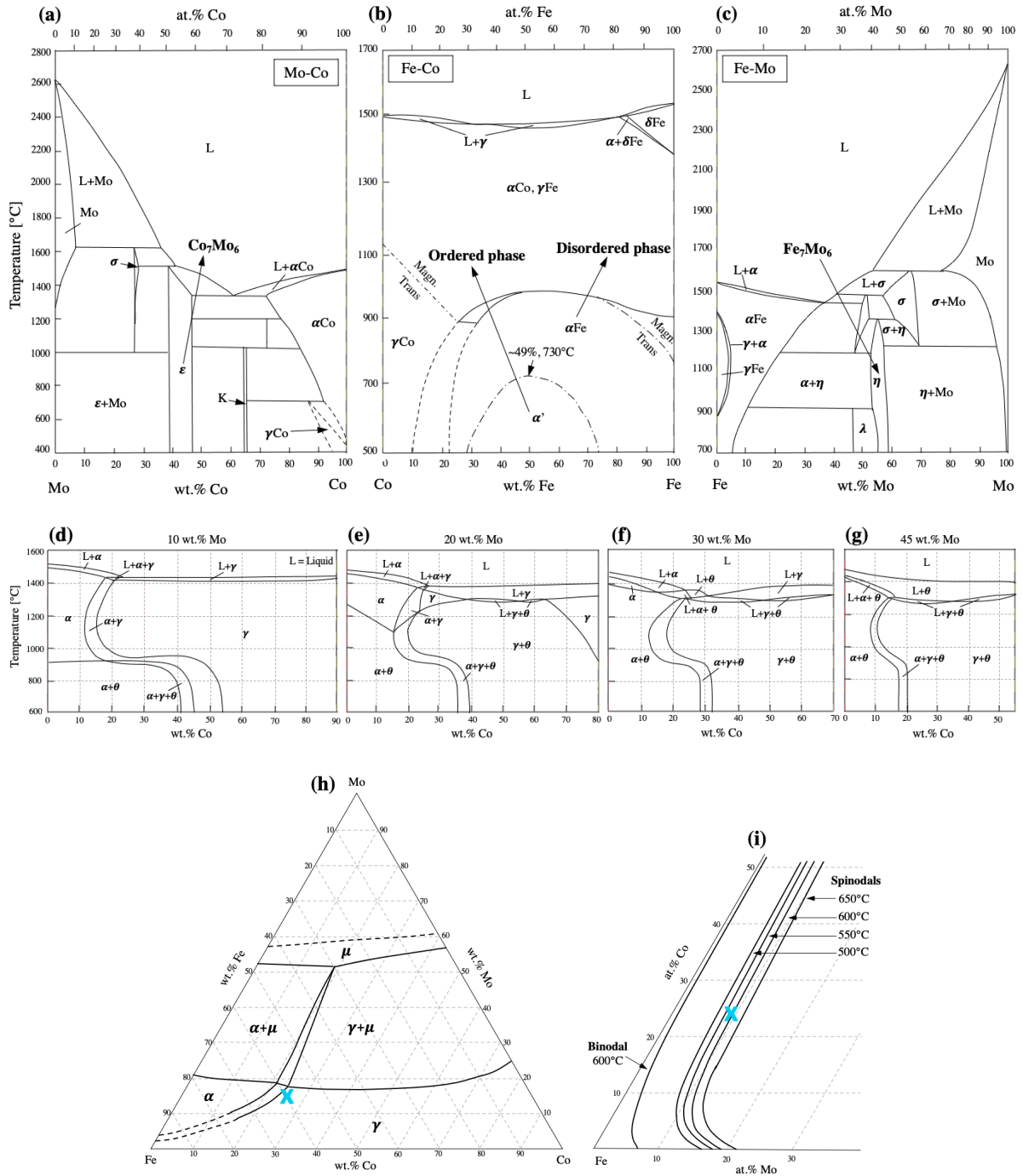


Figure 5: (a-c) Binary phase diagrams: (a) *Mo-Co*, (b) *Co-Fe* and (c) *Fe-Mo* (cf. [20–22]).
 (d-g) *Fe-Co* phase diagrams with varying *Mo*-contents: (d) 10 wt.%, (e) 20 wt.%,
 (f) 30 wt.% and (g) 45 wt.% *Mo* (cf. [22]).
 (h) Isothermal ternary *Fe-Co-Mo* phase diagram at 1200 °C (cf. [24]).
 (i) *Fe*-rich corner with calculated binodal and spinodal lines (cf. [19]).

29 at.% Co [5, 23, 25–27].

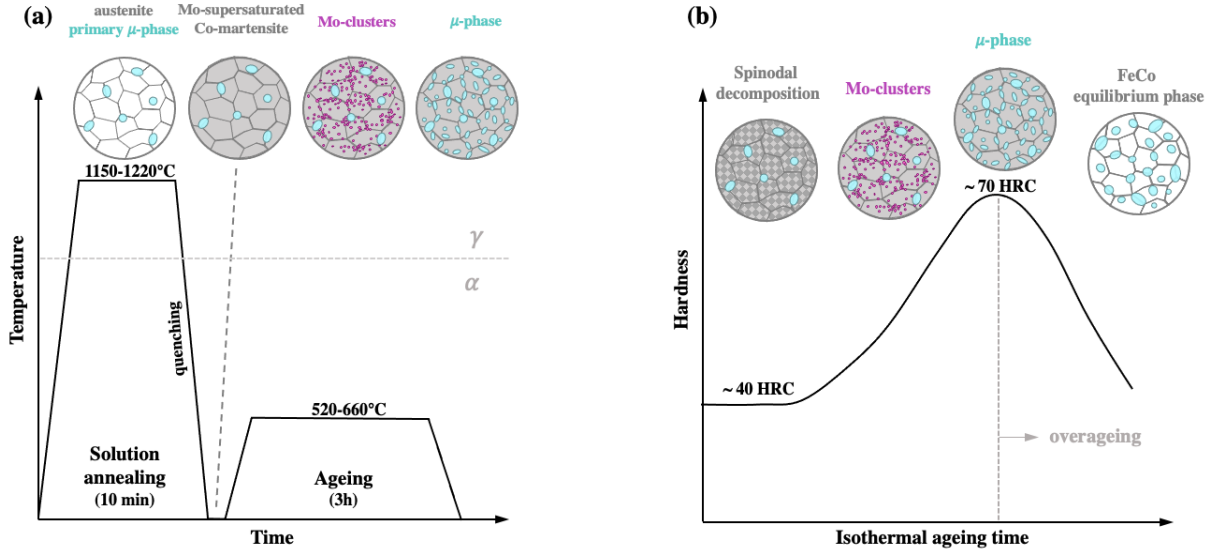


Figure 6: (a) Schematic microstructural development during the conventional heat treatment of a *Fe-25Co-15Mo* alloy (cf. [23, 28]).

(b) Hardness evolution during ageing of a conventionally manufactured *Fe-25Co-15Mo* alloy (cf. [23]).

2.3 Additive manufacturing

AM was first introduced for polymers in the 1980s, when it was discovered that 3D parts from materials that are curable with ultra-violet (UV) light can be produced with a scanning laser. The underlying mechanism for the technique, known today as stereolithography, is photopolymerisation. Since then, multiple AM techniques have evolved for a wide variety of materials, including ceramics, metals and even composite materials. Popular AM techniques include binder jetting, sheet lamination and material extrusion, just to name a few [29].

AM of metals has been the focus of many scientific investigations in recent years. In principle, metal-AM processes build parts from powder or wire feedstock material. The shapeless feedstock is selectively melted by a high-energy source (laser or electron beam) in an inert gas or vacuum atmosphere. AM provides the ability to fabricate parts with complex geometries that cannot be manufactured with conventional methods. Moreover, AM techniques promise to directly build parts from a computer aided design (CAD) model that need hardly any further machining or assembly. For tooling applications, one objective is to build integrated cooling channels in tools (e.g. drills), which follow the surface geometry of the tool as closely as possible to provide optimal cooling. From an environmental point of view, non-subtractive manufacturing may reduce material waste, if the unused metal powder or wire is recycled properly [1, 2, 29, 30].

There are two main AM techniques for producing dense metal parts: LPBF (or electron beam

melting, EBM) and direct energy deposition (DED). In contrast to LPBF, DED directly melts and deposits the feedstock material. Due to thicker layers and higher energy input, the material deposition rate in DED is much higher than in LPBF. DED is also more practical to build small features on curved surfaces and for on-site repairs. Other metal AM processes use binder agents to form a green part, which is then sintered. During sintering, the binder evaporates. This results in porous parts, which can subsequently be infiltrated for higher density or used for lightweight constructions [29, 30].

2.3.1 Laser powder bed fusion

Figure 7 a schematically shows the LPBF process. A rake spreads the powder with a specific layer thickness (usually $30 - 50 \mu\text{m}$ [30]) across the building platform. After the powder is applied, it is selectively melted by a laser, according to the parts cross-section in the CAD model. The laser is guided by a mirroring system and a f-theta lens. After selectively melting one cross-section, the process repeats for the next powder layer. Accordingly, the part is built layer by layer [2, 29, 31].

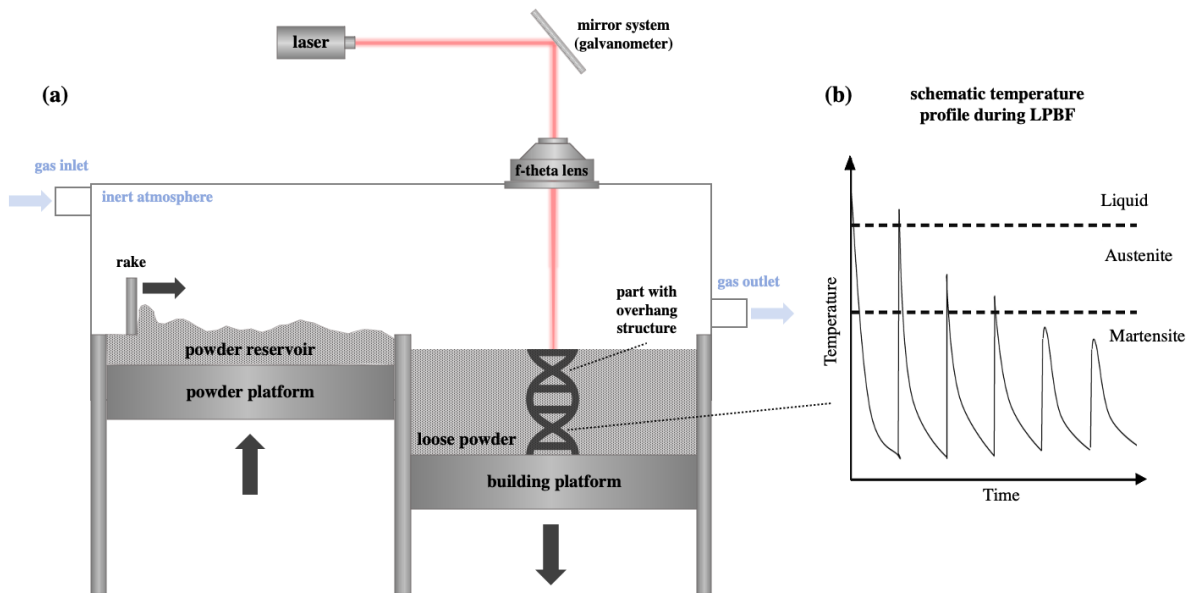


Figure 7: (a) Schematic depiction of the LPBF process (cf. [32]).

(b) Temperature profile of one layer during LPBF fabrication (cf. [31]).

The energy input that is available to fuse the powder particles during LPBF is defined by the volumetric energy density (VED) [31]:

$$VED [J/mm^3] = \frac{P_L}{v_{scan} \cdot h \cdot D}, \quad (1)$$

2 Theoretical background

where P_L is the laser power, v_{scan} the scanning velocity, h the hatch distance (distance between adjacent weld beads) and D the powder layer thickness. D , h and v_{scan} are schematically depicted in figure 9b. During the LPBF process, each layer experiences multiple heating and cooling cycles with each subsequently deposited layer (see figure 7b). These thermal cycles can cause remelting of previously applied layers or phase transformations, depending on the distance from the powder bed surface. Therefore, intrinsic heat treatment (IHT) can be expected during the LPBF process. The cooling rate in LPBF can be as fast as 10^7 K/s [33]. The resulting microstructure is therefore very fine and oriented along the thermal gradient. Since the heat source is moving continuously during LPBF, a variety of solidification modes can be active during the process. In general, the solidification morphology is mainly dependent on the temperature gradient and the grain growth rate. The relation between thermal gradient G and growth rate R is depicted in figure 8. The relation $k = G/R$ is determinant for the solidification structure. Small k -values favour dendritic structures, while high values result in planar structures. The product $G \cdot R$ determines the fineness of the structure, with high values creating microstructural refinement [31, 33, 34].

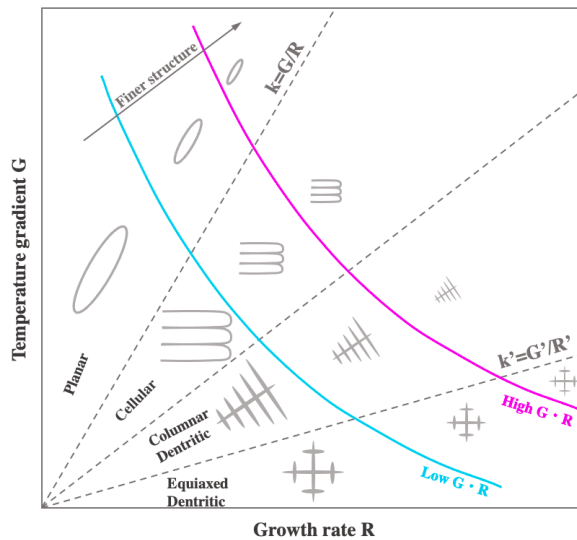


Figure 8: Influence of thermal gradient and growth rate on the solidification morphology (cf. [34]).

2.3.2 Directional solidification in LPBF

The active solidification mechanisms in LPBF are dependent on various processing parameters. Hence, the solidification microstructure can be tailored by adjusting the laser parameters. Sofinowski *et al.* [35] studied the manipulation of directional solidification in 316L stainless steel during LPBF by varying laser scanning angles. The site-specific control over solidification conditions resulted in highly textured microstructures and the integration of dissimilar microstruc-

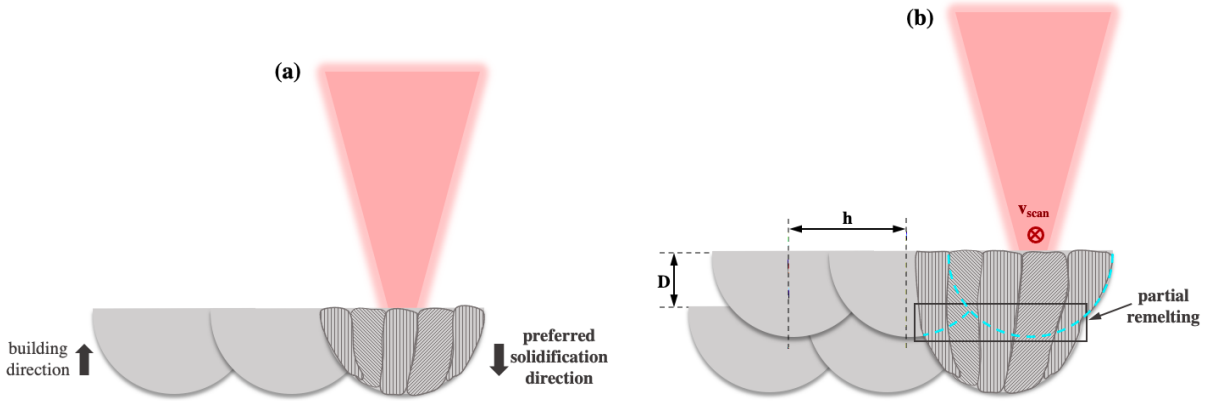


Figure 9: (a) Directional solidification during LPBF.
 (b) Deposition of a subsequent layer, partial remelting of the previous one and epitaxial grain growth (cf. [35]). D , h and v_{scan} are schematically shown.

tures in the same build. Similar investigations have been conducted with *Ni*-based alloys [36, 37]. Sofinowski *et al.* found that intra-layer epitaxial growth with a $\{100\}$ texture parallel to the scanning direction results from bi-directional scanning strategies (i.e. serpentine scanning) in cubic alloys.

During melt pool solidification in metals, multiple grains can nucleate and grow perpendicular to the solidification front. In LPBF materials, grains generally grow epitaxially along the direction of the maximum heat flow, i.e. parallel to the building direction (see figure 9 a and b). Subsequent layers will remelt grains formed near the surface of the melt pool. If they are not fully remelted, these grains may grow epitaxially into subsequent melt pools, as less energy is required for grain growth than for grain nucleation. It is therefore energetically favourable for new grains to grow epitaxially along the direction of already existing ones. The significant driving force for the formation of elongated grains that extend over multiple layers can therefore be explained by the pronounced thermal gradient and partial remelting that occurs during LPBF [35].

2.3.3 Residual stresses in LPBF parts

Formation of residual stress in AM parts originates with the solidification of each new layer and evolves with each subsequently deposited layer. LPBF is characterised by fast heating rates due to high energy inputs and steep thermal gradients. The small size of the melt pool compared to the size of the building platform and the already built part causes rapid solidification with high cooling rates. The rapid cooling of a newly deposited layer leads to material shrinkage, which is partially restrained by the underlying material. As a result, tensile stresses are formed in the top layer. When the next layer is deposited on top of it, the underlying material experiences heating, accompanied by thermal expansion. However, the expansion is hindered by the surrounding material with lower temperature. Thus, compressive stress is formed in the heated zone. When

the heat source moves away, the material is cooled down again. This facilitates shrinking, which is partially inhibited by the plastic strain formed during the heating stage. The yield strength of the material may be exceeded locally, resulting in plastic deformation. Furthermore, the heat input at the top may cause remelting or phase transformations in underlying solidified layers (see figure 7 b), which can induce additional residual stresses. As a result, residual stresses near the surfaces of AM parts tend to be tensile, while they tend to be compressive in the center. These residual stresses are critical for the fabricated parts as they can cause distortion, cracking or delamination from the building platform. The thermal history of LPBF layers and hence the residual stress evolution depends on the scanning pattern and other process parameters, such as P_L or v_{scan} [30, 38].

The most effective preventive method for reducing residual stresses in AM parts is in-process heating of the building platform. With preheating, the thermal gradients are reduced and as a result, the danger of part deterioration is lowered. Because parts may distort or even crack due to residual stresses when they are removed from the building platform, stress-relief annealing can be applied in advance to the removal of the building platform [38].

2.3.4 LPBF of maraging steels

The application of maraging steels in special industries such as aerospace, military and tooling is owed to their superior mechanical properties. These applications usually require limited amounts of parts with complex and custom geometries. Hence, AM promises the optimal use of individualisation- and complexity-for-free advantages. Furthermore, the high cooling rates during LPBF have favourable effects on maraging steels, providing sufficient cooling capacity for the martensite formation and supersaturation. The cyclic heating and cooling during LPBF is subject of recent investigations in regard to triggering in-process precipitation and obliterating the need for subsequent ageing treatments. This IHT has been realised for maraging steel samples manufactured with laser metal deposition. For LPBF maraging steels, the presence of retained austenite is possible, which can contribute to the improvement of toughness and lead to strain hardening due to transformation-induced plasticity (TRIP) [33].

As, to the author's knowledge, no previous investigations of LPBF of the investigated FeCoMo alloy has been conducted, literature on LPBF of other maraging steel grades (i.e. *Ni*-maraging steels) is presented to further understand the micro- and nanostructure development of maraging steels during LPBF.

Due to their low *C*-content and moderate hardness in the as-built condition, *Ni*-maraging steels provide good processability. The processing of such alloys with LPBF without platform preheating is state of the art. Allam *et al.* [33] investigated the nanostructure of LPBF 18Ni300 (X3NiCoMoTi19-9-5 (wt.%) maraging steel with APT. The influence of heterostructures formed during the LPBF process (i.e. cellular and dendritic regions with micro-segregations) on the microstructure evolution was studied. In particular, the formation of nano-sized intermetallic

$(Ni, Fe, Co)_3(Ti, Mo, Al)$ and $(Fe, Ni, Co)_7(Mo)_6$ precipitates during post heat treatment was brought into focus. A fine solidification microstructure was observed, which is typical for parts fabricated with LPBF. The formation of cellular or dendritic solidification structures during LPBF is inherent for maraging steels. Another characteristic feature of LPBF-related heterostructures is the micro-segregation of solutes to the dendrite boundaries [33, 39–41].

Allam *et al.* [33] further found that after solution annealing and ageing, the precipitates were smaller in size and higher in number density compared to the as-built and directly aged state. The as-built state contained heterostructures such as Ni micro-segregations. Subsequent solution annealing dissolved these segregations, which resulted in a highly supersaturated matrix and a higher number of precipitates during ageing. After the precipitation of the intermetallic $(Ni, Fe, Co)_3(Ti, Mo, Al)$ phase, the Ni -depleted matrix inhibited the martensite-austenite reversion. In contrast, the heterostructures in the as-built and aged state promoted the austenite reversion, which led to the formation of reverted austenite during ageing. As a result, the $(Ni, Fe, Co)_3(Ti, Mo, Al)$ number density was decreased.

Jägge *et al.* [41] studied the austenite reversion behaviour of LPBF $Fe-18 Ni-9 Co-3.4 Mo-1.2 Ti$ (wt.%) maraging steel. In the as-built state, neither precipitates nor clusters were found with APT, which led to the assumption that the reheating duration during LPBF was not long enough to facilitate precipitation. Ageing resulted in the successive precipitation of three different phases, the last of which was the μ -phase. Mo -rich Ni_3X precipitates seemed to act as nucleation sites for the μ -phase precipitation.

Jarfors *et al.* [42] studied the anisotropy of LPBF maraging steel (1.2709). In a thermodynamic computation with ThermoCalc™ Scheil segregation analysis, they showed the segregation of a Mo -rich Laves phase during solidification. The composition of this Laves phase may vary significantly under different thermal histories, but it mainly consists of Fe, Ti, Ni, Mo and Si . As Jarfors *et al.* [42] did not find any Co -free precipitates, they suggested the absence of the Laves phase.

2.4 Atom probe tomography

Mechanical properties of materials are not only dependent on microscale features such as microstructure, precipitations and grain size, but also on nanoscale properties like solute atoms, segregations and nanoprecipitates. In order to investigate the latter, APT has developed into one of the most important analytical microscopy techniques because of its ability to map 3D spatial distribution of elements and molecules on an atomic scale. With its combination of chemical and spatial sensitivity, APT can provide 3D reconstructions of nanostructures [43, 44]. While the resolution of the transmission electron microscope (TEM) has been enhanced to the atomic scale in recent years (mainly thanks to spherical aberration correctors), its chemical sensitivity is limited to about one atomic percent. Additionally, the acquired data and images provide only two dimensional information of an electron-transparent specimen. Recent efforts to gain

access to 3D information (TEM tomography) or enhance the chemical sensitivity (secondary ion mass spectroscopy) both forfeit the atomic spatial resolution. Therefore, APT presently has the unique capability to combine 3D information, near-atomic resolution and a chemical sensitivity down to a few atomic parts per million. However, the analysed volumes are very small (typically $50 \times 50 \times 200 \text{ nm}^3$). Information from APT measurements can therefore only be extrapolated for homogeneous materials. Furthermore, APT is a destructive technique, so measurements cannot be conducted on the same sample more than once [43–45].

2.4.1 Measurement principle

The application of a sufficiently high electric field to a specimen breaks atomic bonds at the surface and atoms from that surface leave it as positively charged ions, which are then accelerated in the electric field. This effect, called “field evaporation”, is the basic operating principle of APT measurements. Hence, it is ideally possible to evaporate specimens atom by atom and explore their volume one atomic layer at a time. In other words, the specimens in APT act as field ion emitter sources. The technique exploits the high static electric field that arises at a sharp specimen tip when voltage is applied. The general idea is to create an electric field that is high enough to induce forces so strong that they counterbalance the attractive forces needed to maintain the cohesion of atoms at the specimen surface. A sufficiently high positive electric field (in regard to the specimen surface) leads to the desired field evaporation of surface atoms. The electric field strength necessary to induce field evaporation and generate a controlled emission current is dependent on the chemical nature and environment of the atom being evaporated. The required electric field strength is in the order of 10^{10} V/m [43–45]. Because a maximum of only a few thousand elementary charges are drained from the sample per second, the electrostatic approximation (i.e. standard Maxwell’s equations) provides a good description of the actual field generation mechanisms [43].

APT measurements can be carried out in two different modes: voltage and laser mode. The basic principle of both modes is the evaporation of ions from the surface of the specimen tip during electric or thermal pulses. These pulses occur periodically (typically with a frequency of some hundred kHz [43]) and are superimposed to a positive standing voltage $V_{standing}$ (in the range of 1-30 kV [43]). The mechanisms of voltage and laser pulsing are schematically depicted in figure 10. Field evaporation may be triggered by either increasing the applied voltage at the specimen tip (voltage pulsing) or by increasing the temperature (laser pulsing).

2 Theoretical background

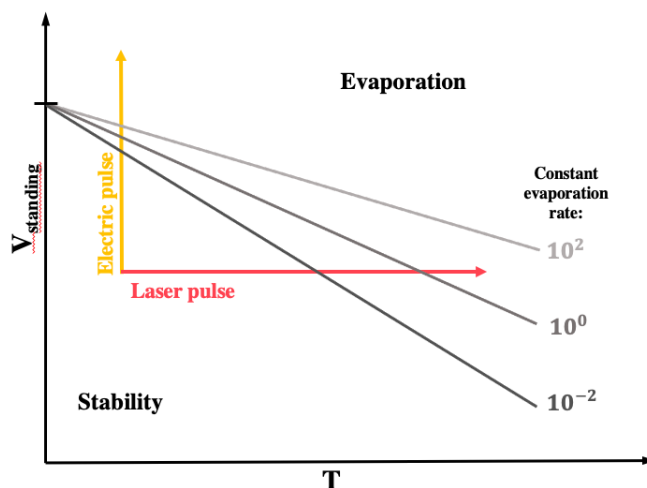


Figure 10: Schematic dependence of constant evaporation rate on $V_{standing}$ and temperature (cf. [46]). Voltage pulsing increases the voltage at the specimen tip, while laser pulsing increases the temperature. Both may lead to field evaporation.

$V_{standing}$ is chosen in a way that no evaporation occurs between the pulses. When a short-duration voltage pulse is applied in the voltage mode, the total voltage is temporarily raised to the operating voltage $V_{operating}$ ($= V_{standing} + V_{pulse}$). This temporarily elevates the field to an operating level with a good probability for ion emission from the specimen surface and the pulse fraction is defined as $PF = \frac{V_{pulse}}{V_{standing}}$ [43]. The voltage mode requires the specimen material to be electrically conductive. For poorly conductive materials, the laser mode is used, where ions are evaporated from the specimen tip during ultrafast laser pulses. The thermal energy from the laser pulse, in addition to the standing voltage, also leads to surface evaporation of atoms [43], as is shown in figure 10. It is particularly important that no field evaporation occurs at the standing field and temperature. In alloys, there should be no preferential evaporation of one species relative to the other at the operating voltage and temperature. Standing and operating fields and temperatures must therefore be carefully chosen in order to avoid artefacts in the collected data. In general, a lower standing voltage and lower temperature helps to ensure that no field evaporation occurs between the pulses. However, if the standing voltage is too low, contaminations can be adsorbed on the specimen surface, which can lead to field corrosion. In the voltage mode, a higher pulse fraction, shorter pulse length and higher pulse repetition frequencies may help to minimise preferential evaporation effects. However, these conditions put larger stresses on the specimen tip and increase the risk of fracture [45]. For the laser assisted field evaporation, the cooling time of the tip apex must be minimised in order to provide an adequate mass resolution. A larger shank angle (i.e. larger cone angle, see section 2.4.3) provides a larger heat sink and therefore better heat conductivity. The result are less pronounced thermal tails in the mass spectrum. An increase of the cone angle from 2° to 15° can reportedly improve the signal-to-noise ratio by almost two orders of magnitude [43].

2 Theoretical background

APT measurements are carried out in an ultra-high vacuum chamber at low temperatures (20 – 80 K [43]), so the interaction of ions from the specimen tip with surrounding gaseous atoms or molecules is kept at a minimum during their flight through the electric field. A position-sensitive detector intercepts the ions in their flight path. It enables the visualisation of a 3D atom probe, revealing the shape, distribution and morphology of nanoscale features. In the history of APT, it was discovered early on that different phases have different evaporation fields, which results in a phase contrast. Consequently, it is possible to image nanoparticles and characterize microstructures [43].

The chemical nature of the evaporated surface atoms is identified by time-of-flight (TOF) mass spectroscopy. TOF is the time an ion needs to fly from the sample surface to the detector. It can only be measured if the evaporation is triggered by a voltage or laser pulse. As the surface atoms are evaporated by electric or thermal pulses, the signal from these pulses yield the origin of time, from which the TOF to the detector can be calculated. Light species have higher velocity than heavier ones and therefore have a shorter TOF. Accordingly, the TOF measurement yields the mass-to-charge ratio (m/n) of evaporated ions. The principle of conservation of energy states, that the initial potential energy of the ion in the electric field ($E_{pot} = neV$) must be equal to its final kinetic energy ($E_{kin} = \frac{1}{2}mv^2$) at the detector. With the ions velocity $v = \frac{L}{t}$, this yields the following for the mass-to-charge ratio [43]:

$$\frac{m}{n} = \frac{2eVt^2}{L^2}, \text{ with} \tag{2}$$

m	mass of the ion,
n	charge state of the ion,
e	elemental charge,
V	$V_{operating}$,
t	TOF,
L	real flight length.

Equation 2 assumes that the ions have no initial velocity and a constant velocity during the flight (i.e. that the acceleration path can be neglected compared to the flight length). This is, however, a simplification, as will be shown in section 2.4.7 [43].

With the mass-to-charge information, a mass spectrum can be built and the allocation of various peaks allows the identification of chemical species. The quality of the mass spectrum depends on not only the physics of field evaporation but also the flight length (APT design), the hardware devices used to reduce energy deficits (i.e. reflectrons, see section 2.4.7) and the analysis conditions (voltage, detection rate, specimen temperature, pulse fraction or laser energy). A higher mass resolution reduces overlap of the peaks and therefore permits a more reliable identification of the peak spectrum. For a high mass resolution, ultra short pulses (1 ns [43]) are required, as well as a time acquisition accuracy better than 1 ns. Modern APT detectors rely on time-resolved position-sensitivity. Their functioning principle is further described in section 2.4.1 and

2 Theoretical background

depicted in figure 11. These detectors simultaneously provide the TOF of ions and the lateral position of their impact. The position-sensitivity of the detector allows the deduction of the real flight length L in equation 2 by combining the physical distance of the specimen from the detector and the relative XY -position of the ion (see section 2.4.7) [43].

In order to solve the initial problem of weak intensities of APT images, charge amplifiers are implemented in the imaging system. These charge amplifiers are realised as microchannel plates. A microchannel plate is an active electron conversion system that transforms any particle impact at the input into a secondary electron cascade at the output. It consists of a thin disk with high electrical resistivity, which contains a regular array of tiny tubes (microchannels) with diameters close to $10\ \mu\text{m}$. These microchannels are densely distributed over the whole surface. They are placed parallelly to each other with spacings of $\sim 15\ \mu\text{m}$. A set of two microchannel plates is placed in chevron with a spacer of $100\ \mu\text{m}$ between them. The number of created electrons is independent of the chemical nature of the detected species but can be controlled by the polarization between the input face of the first plate and the output face of the second one. If an ion enters a channel on the input face of the first plate, it creates a number of secondary electrons. The same number of electrons is created each time one of these electrons touches the border of the channel. The input face of the second microchannel plate collects the electron cloud from the output face of the first plate and the phenomenon repeats. At the end of the detection process, a cascade of electrons is available at the output of the second microchannel plate. In short, the microchannel plates amplify a particle into an electron cloud, which is used to define the impact position. Additionally, temporal information can be extracted from the analogue signal for the TOF mass spectroscopy. The TOF is calculated as the time difference of the analogue signal from the evaporation pulse (start time) and from the microchannel plate (stop time) [43].

Behind the output face of the second microchannel plate, two delay line detectors with a disorientation of 90° (X, Y) are situated. The first part of the electron cloud output from the microchannel plates is collected by the first delay line X , where it generates two analogue signals. The signals travel in opposing directions in the X line, until they reach its respective end. The rest of the electron cloud is collected by the second delay line Y . Using the combined temporal information at the four ends of the delay lines, the lateral (X - Y) position of the hit is determined. It is calculated from the time difference it takes for the electric signal to reach the opposite ends of the respective channel. The size, time width and amplitude of the signal depends on the quantity of collected electrons. Hence, both mass and spatial resolution depend on the precision of the extracted temporal information from analogue signals [43].

As the evaporation of multiple ions during one pulse is unavoidable, the detector is also required to process multi-hit events with a time separation of a few nanoseconds. Simultaneous multiplicities are defined as atoms detected in the same pulse with the same mass-to-charge ratio. Serial multiplicities are ions from the same pulse with different mass-to-charge ratios. The terms “same” and “different” depend on the mass resolution (i.e. the broadness of mass peaks, see section 2.4.7) of the instrument. The mass resolution is defined as the ability of the detection system to identify ions with very narrow ranges of mass-to-charge ratios (i.e. mass

resolving power). The mass resolving power is in turn dependent on the time resolution power of the instrument, which is the ability of the detection system to discriminate two analogue signals with a short time difference (dead time). This link between mass and time resolution is caused by the structure of the detection system. In summary, there is a conversion from position (impact on the microchannel plate) to time (temporal information extracted from the analogue signal on the delay line detector) and back to position (calculation from the timing information at the four ends of the delay line detector) [43].

2.4.2 Local electrode atom probe

Figure 11 shows the principal components of a local electrode atom probe (LEAP), including the detection system described in section 2.4.1. The main improvements to the atom probe design compared to previous models include the introduction of a local electrode, the application of laser-pulse-induced evaporation, the use of crossed delay line detectors and high-frequency pulse generators. The latter can provide pulse frequencies up to 200 kHz for voltage pulsing and 1 MHz for laser pulsing [45].

The specimen is cryogenically cooled and mounted on a nano-positioning stage. It is held to a high positive standing voltage $V_{standing}$ and the ions are evaporated during a negative voltage pulse with an amplitude V_{pulse} or a laser pulse. The local electrode is a close-proximity counter electrode with a central circular aperture (see section 2.4.7) and the impact position X - Y on the detector is determined by a crossed delay line detector (see section 2.4.1) [45].

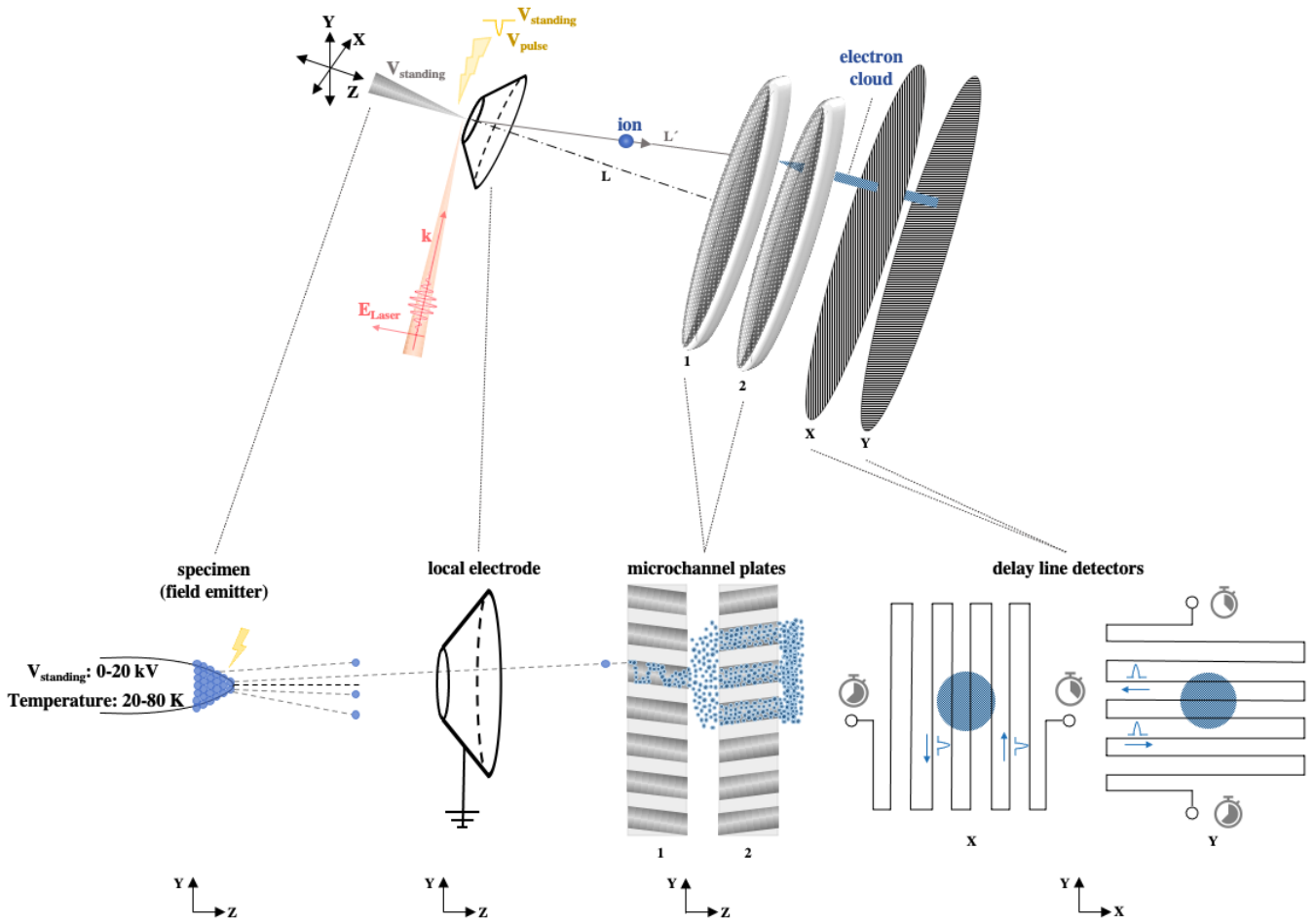


Figure 11: Principal components of a LEAP with detailed depictions of the specimen tip, local electrode, microchannel plates and delay line detectors (cf. [43, 45]).

2.4.3 Specimen geometry

The trajectories of ions are almost exclusively determined by the tip shape, the crystallographic orientation of the investigated phases and their local chemical composition [43]. As the tip geometry plays such an important role in the results of APT measurements, it is dealt with in detail in this section.

Specimens for APT are prepared as sharply pointed needles with an end apex that has an almost half-spherical shape (see figure 12). The tip radius R should be in the range of 10-200 nm. The length of the needle is more than several microns in order to enhance the local field at the tip apex sufficiently [43].

2 Theoretical background

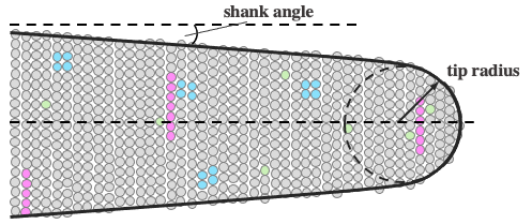


Figure 12: Specimen geometry: shank angle and tip radius (cf. [43]).

The field F on the tip axis and at the tip surface (i.e. in a distance R from the focal point of the tip) is given by

$$F = \frac{V}{k_f R}, \quad (3)$$

with the so-called field-factor k_f [43, 45]

$$k_f = \frac{1}{2} \ln \left(\frac{2L}{R} \right). \quad (4)$$

k_f is a semi-constant that takes into account the tip shape, which changes over the measurement (hence *semi*-constant) and its electrostatic environment. For a sphere, $k_f = 1$. For real emitter shapes $k_f > 1$, which is primarily due to the emitter shank, see figure 12. A large shank angle considerably reduces the enhancement of the field at an angular position. For the relation in equation 4, the tip geometry was approximated with a paraboloidal geometry. The values for k_f are in the range of 2 – 10 [43, 45]. Due to the shank angle, the tip radius increases after the evaporation of just a few atomic layers. Therefore, the standing voltage is increased continuously during the measurement in order to keep a constant electric field and consequently an almost constant evaporation rate. Hence, the tip geometry changes continuously during the measurement and the applied voltage follows. The standing voltage-curve during the measurement can therefore be used to estimate F and subsequently the tip shape for the 3D reconstruction. The evolution of the tip radius leads to a constant change in magnification that cannot be controlled directly. With the tip blunting during the APT measurement, k_f also increases slightly [43]. In order to take into account the real tip shape (tip radius and shank angle) as well as the AP chamber geometries, Gipson [47] found that the surface field follows the following expression:

$$k_f = k_{1(R/L)} \left(1 + \sin^2 \frac{\theta}{4} \right)^{\frac{1}{2}} \cdot e^{k_{2(R/L)}}. \quad (5)$$

The values of k_1 and k_2 are dependent on the relation (R/L) of the tip radius to the flight distance. Additionally, the expression found a variation of the field with the angular position θ [43, 47].

2.4.4 Physical conditions at the specimen tip

The work needed to remove an atom as a neutral from the emitter surface, is its bonding energy. If no field is applied, the bonding energy of solid chemical elements Λ^0 is equal to the tabulated sublimation enthalpy ΔH^{sub} . In presence of an external electric field F , the bonding energy Λ^F can be written as

$$\Lambda^F = \Lambda^0 + \frac{1}{2}\Omega\varepsilon_0F^2, \quad (6)$$

where Ω is the atomic volume and ε_0 the dielectric constant. Equation 6 describes the change in capacitance of the emitter if the atom is removed [45]. In order to understand the effects of such a strong electric field as it is applied to the specimen tip in APT, a sphere shall be viewed as simplification of the tip (i.e. the shank is neglected). At the surface of a sphere with radius R , the strength of an electric field is given by $F = \frac{V}{R}$, where V is the applied voltage. If a voltage of 1 kV is applied to a sphere with a radius of 100 nm, the generated field reaches 10^{10} V/m, which is necessary for field evaporation. The presence of such a high field can strongly affect the surface material of the specimen and surface stresses are induced by the charge layer. The so-called Maxwell stress tends to pull on the surface, regardless of the sign of the charge layer. The resulting force per surface unit is given by

$$f_s = \frac{1}{2}\varepsilon_0F^2. \quad (7)$$

For the examined sphere, the result is a tensile stress of ~ 500 MPa ($\approx \frac{1}{2} \cdot \varepsilon_0 \cdot 10^{20}$). In the surroundings of the sphere, the field is located near the surface and the strength of the field decreases exponentially with the distance from the sphere. A sufficiently strong field triggers the ionisation of particles, a mechanism referred to by Haydock and Kingham as post-ionisation. Regarding post-ionisation, Haydock and Kingham developed a theory, which states that atoms first evaporate as single-charged ions. An electron tunnels through a barrier and leaves the atom, resulting in an ion with one elementary positive charge more than before. During the early stages of its travel near the specimen tip, the ion may lose additional electrons depending on the electric field. The higher the field, the higher the eventual charge state of the ion [43, 45, 48].

In reality, the presence of the specimen shaft decreases the magnitude of the generated field. Nevertheless, the field can be amplified by the implementation of the local electrode, as is described in section 2.4.7. The negative field from that counter electrode tries to move the surface atom electrons towards the positive specimen shaft, but this is resisted by exchange-type repulsive forces, caused by quantum mechanical effects. The electric field pulls the nuclei away from the surface and displaces them from the electrical center of the surrounding electrons, which exposes them to electrical restraining forces. The outcome is a polarized surface layer with electrostatic potential differences across the layer, with the higher potential on the vacuum side.

2 Theoretical background

As the field rapidly drops along the specimen shaft in an exponential manner, the evaporation field is naturally confined to the tip apex [43, 45].

For electrons near a metal surface in vacuum, there are two competing tendencies. One effect is purely chemical, the other one is an electric dipole effect, which depends on the chemical nature and the arrangement of surface atoms in the crystallographic plane of interest. At the metal surface, electrons are spread into the vacuum, creating an electric dipole with its negative end pointing towards the vacuum. Simultaneously, the electrons are pulled into the gaps between atoms. For a given element, the effect of the pull is dependent on the crystallography. Thus, there are differences in the electric dipole moment at the metal surface and consequently the local evaporation fields vary for different crystallographic planes and different chemical elements [45]. With the laser assisted field evaporation, the risk of specimen rupture is reduced, especially for the investigation of fragile materials. The laser pulses are directly focalised on the apex of the specimen, keeping the mechanical stress from the electric field almost constant. Unlike investigations in the voltage mode, the laser mode does not expose the specimens to the cyclic mechanic loading and unloading due to oscillations of the Maxwell-stress. Laser assisted field evaporation also opens the application of APT for non-metallic materials, for which the voltage mode is not suitable due to their high electric resistivity. But also for some metallic samples, the laser mode can provide improvements regarding mass resolution and sensitivity (i.e. signal-to-noise ratio). If the illumination conditions are chosen accordingly, the mass resolution improves due to a decreased evaporation time and reduced energy spread of the evaporated ions. Additionally, the laser mode allows an increased ion collection angle. Hence, larger sample volumes can be investigated by reducing the distance between specimen tip and detector [43].

When the laser interacts with the specimen, the optical properties of the material (i.e. its complex refractive index) play an important role. When the refractive index of the material is known, the reflected, transmitted and absorbed energy can be calculated for the respective wavelength of the laser. However, due to the nanometric dimensions of the specimen tip, its shape can strongly influence the laser-specimen interaction. Because the material investigated in this thesis is metallic, only the properties of laser-metal interaction will be presented in the following. In metals, the laser photons interact with the electrons in the partially filled conduction band. The electrons are excited to higher energy levels and then relax through electron-electron collisions and electron-phonon collisions. As a result, the lattice temperature increases. The tip shape can influence the distribution of laser photons on the surface. Several physical effects have an influence on the laser-sample interaction. Firstly, diffraction of the incident laser beam occurs at the interface between the metallic tip and the vacuum. The tip apex is a diffraction source that emits in all directions. This diffraction source interacts with the incident and reflected beams and creates oscillating surface currents on the shank surface. Because the absorption properties are linked to the surface current density of the material, absorption maxima are observed on the shank surface. Secondly, collective excitation of surface electrons leads to an increase of absorption efficiency. The latter shows a maximum at the resonant excitation wavelength, depending on the tip radius. Accordingly, the absorption efficiency at the tip apex is much higher than

2 Theoretical background

for bulk material (i.e. the specimen shaft). Lastly, the cone shape of the specimen leads to a decreasing absorption along the axis, as the radius increases [43].

If a laser pulse is used to trigger the evaporation, the evaporation mechanism can be photo-ionisation (resonant ionisation of surface atoms), absorption (thermal assisted evaporation) or an increase of the surface field (evaporation by energy barrier reduction). The latter is negligible for metallic specimens. Photo-ionisation only occurs at low laser energies, where thermal energies are drastically reduced. The interaction of a photon with an electron of a surface atom leads to the transition of the electron to a vacant energy state and consequently to the ionisation of the surface atom. The atoms are first ionised to the $1+$ state and then post-ionised near the tip surface, according to the Kingham theory [48]. In contrast to photo-ionisation, absorption of the laser energy leads to heating of the sample. The rise in temperature (thermal pulse) triggers the evaporation process (see figure 10) and the evaporation rate follows the temperature dynamics of the tip apex. As the heating process can be very fast (a few picoseconds [43]), the dynamics of the evaporation rate depend only on the cooling conditions of the specimen. The temperature profile along the specimen axis depends on the base temperature of the specimen, its thermal properties and the illumination conditions of the tip. Therefore, the same illumination condition can trigger different thermal pulses for different specimen geometries [43]. In order to obtain good mass resolution, the thermal pulse should be as short as possible. Hence, the heating time of the tip apex should be minimised, so the laser energy is directly absorbed. This can be achieved by trying different tip geometries and laser wavelengths. Additionally, the cooling time should be minimised by reducing the heated area or by larger shank angles (see section 2.4.3) in order to avoid thermally induced migration of surface atoms [43, 45].

The mass resolution strongly depends on the illumination conditions. Larger wavelengths lead to a larger heated area (larger absorption region) and consequently to a bad mass resolution. Moreover, larger wavelengths move the first absorption maximum further away from the tip apex, resulting in an increase of the heating time and an increase of the width of the peaks in the mass spectrum. If the tip radius is far from the resonance value, the absorption is not well confined at the apex, increasing the heated area and decreasing the mass resolution. For materials with poor thermal conductivity, the pulse rate of the laser plays an important role for the signal-to-noise ratio. If the time between two pulses falls below a critical threshold, the sample never has the chance to cool down to the base temperature, which has a negative effect on the signal-to-noise ratio [43].

2.4.5 Specimen preparation

The APT specimen preparation consists of selecting a nanometre-small volume of material and giving it a shape that enables field evaporation. Hence, the specimen must be a needle with a shank angle typically less than 20° and a tip radius of 20 – 100 nm at its apex [43].

Specimen preparation by electropolishing is the standard technique for metals. Electropolishing

2 Theoretical background

is an ablative process, during which the charge exchange between a metallic part (anode) and a cathode in an electrolyte leads to an electrochemical removal of surface material. Material removal occurs with current densities in the transpassive range of the current density-voltage curve [49, 50]. The principle of the electropolishing procedure for APT is shown in figure 13.

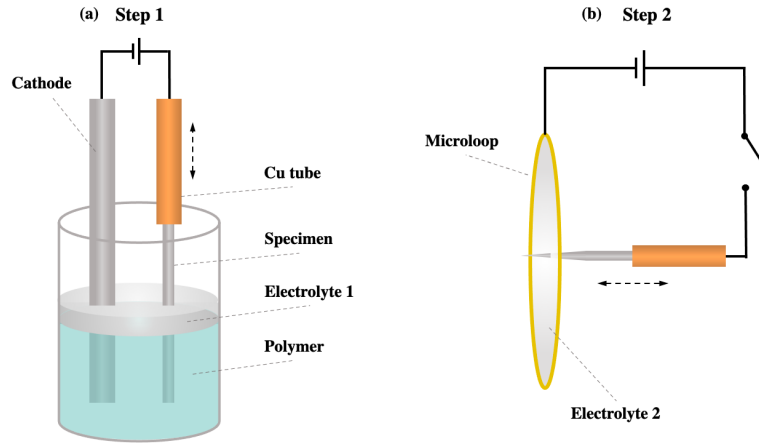


Figure 13: Schematic electropolishing procedure of specimen tips for APT: (a) standard electropolishing technique and (b) microloop method (cf. [51]).

The initial dimension of the specimen blank is approximately $0.3 \times 0.3 \times 20 \text{ mm}^3$. The principle idea is to form a neck in the specimen blank and initiate a controlled break at the neck in a final step by applying a low voltage (resulting in a low current). Thus, two specimen tips can be generated by the first preparation step from only one blank by retrieving the specimen that falls into the beaker (see figure 13 a). If the first electropolishing step does not yield a sharp and clean needle, micropolishing is applied with the so-called microloop method (figure 13 b). The name stems from the fact that the cathode consists of a small loop made from a noble metal (usually gold). The microloop is responsible for holding a small droplet of electrolyte through which the specimen is moved horizontally. Similarly to standard electropolishing, micropolishing forms a neck before breaking it to obtain a sharp needle. Once the neck breaks, the specimen must be quickly withdrawn from the droplet and rinsed with alcohol to attain a sharp tip. The specimen preparation process is monitored with a light optical microscope (LOM). As the optical microscope does not provide sufficient magnifications, the apex of an APT needle can be inspected with TEM or SEM prior to insertion into the LEAP. While electropolishing is a method that is easy to apply, the presence of microscopic features (e.g. grain boundaries or precipitates) in the tip volume is random and not reproducible, since they are invisible during preparation. Moreover, if various polishing rates occur in different phases of an alloy, electropolishing should be avoided [43].

For site-specific preparation and selection of features of interest, techniques combining SEM imaging and focused ion beam (FIB) milling are applied. SEM can visualise nm-sized features

2 Theoretical background

and the interaction of the electron beam with the material can provide additional information. For example, electron back scattered diffraction (EBSD) may be used to determine the crystallographic orientation of the grains in the specimen or to select specific grain boundaries for the APT analysis. Unlike electropolishing, FIB can also be used to prepare samples from almost any material, including semiconductors and insulators [43].

Positively charged *Ga* ions are used as primary ion source in FIB systems, because *Ga* has a low melting temperature ($\sim 30^\circ\text{C}$ [43]) and a low steam pressure. It ionises mostly as Ga^+ , which allows a very narrow energy distribution of the ion beam. *Ga* ions are typically accelerated at 30 kV. This accelerating voltage is in the same order of magnitude as that of electrons in an electron beam. However, *Ga* ions have a larger mass than electrons and therefore carry a larger momentum. Thus, they can affect the structure of the material they interact with. During low-energy FIB milling (e.g. during the final stages of the preparation), secondary electrons can be emitted from the material, which provide additional imaging capabilities. A fraction of *Ga* ions that hits the specimen surface, interacts with the material by generating sputtered atoms and ions, implanting themselves into the material or causing other point defects. The collisions of ions with the material can also cause recrystallisation or even amorphisation. The sputtering outcome depends on the incident angle of the ion beam, the atomic number of the bulk material and the crystallographic orientation. The depth of the *Ga* implantation depends on both the material and the energy of the incident ion. If the region of interest (ROI) is located at the surface of the specimen, a *Pt* capping layer can be deposited on the specimen surface. It serves the purpose of protecting the ROI and limiting the *Ga*-implantation to the capping layer. Because of the high evaporation field of *Pt*, the capping layer has to be completely removed previous to APT analysis during low-energy cleaning [43].

Because only small pieces of material can be handled with the FIB, samples are usually prepared with the lift-out method. Thereby, a piece of material is extracted from a substrate and subsequently mounted onto the end of a macroscopic tip. In the first step of the FIB preparation, trenches are cut on each side of the capping layer, so that the ROI forms a wall that is attached to the bulk material on one side. The ion beam is then used to cut a horizontal trench through the base of the wall, forming a cantilever. Simultaneous imaging via SEM during milling allows the observation of the moment when the wall is cut through. A micromanipulator is then inserted and welded upon the end of the cantilever with *Pt*. Finally, the wall is cut free and extracted and its free end is welded onto a support tip. The wall is cut into multiple pieces that are subsequently welded onto different mounts [43]. The next step in the FIB sample preparation consists of milling the mount and giving it a tip shape with the required geometry, using a high-energy Ga^+ ion beam ($\sim 30\text{ kV}$ [43]). This is done with an annular milling pattern that mills the mounted sample into a cylindrical shape that is $1 - 2\ \mu\text{m}$ in diameter. The inner diameter of the annular milling pattern is then reduced step by step to produce a conical shape with a radius of $\sim 50\text{ nm}$ at the apex. As the annular milling radius is reduced, so is the beam current in order not to damage the ROI. The annular milling parameters can be adjusted to control the tip morphology, e.g. to produce a larger shank angle for laser-assisted APT [43].

2 Theoretical background

During high-energy milling, ions are implanted into the material. These implantations can severely damage the surface of the sample. The ion collisions can amorphise the material over a certain area, dissolve precipitates, induce grain growth or form *Ga*-rich phases. Thus, it is important not to include this part of the sample in the analysis and to remove it by milling the tip with a low-energy *Ga* beam (2 – 5 kV [43]). This low-energy cleaning also leaves damages in the material but at much more shallow depths. [43]

For specimens with rough surfaces, field evaporation occurs selectively at the sharpest areas, where the electric field is especially high according to equation 3. Hence, field evaporation provides surface cleaning by smoothing away surface irregularities and residual surface films. As field evaporation creates an atomically clean surface, it can be seen as final step of the specimen preparation. After sufficient field evaporation, the specimen tip develops a material-specific dynamic field evaporation endform. This shape yields an almost constant evaporation rate, which translates into a steady increase of the standing voltage in the measurement. The details of the dynamic field evaporation endform depend on the material and the field evaporation conditions, especially the emitter temperature [45].

2.4.6 Data processing and 3D reconstruction

Technically, APT is a projection microscopy technique with a projection law and a magnification that depends on the flight length. The magnification M is given by $M = \frac{L}{\alpha R}$, where α is the image compression factor (the value of α is between 1 and 2) and R is the specimen tip radius [43]. The lateral positions of atoms at the tip surface (x, y) are simply derived from the position of the ion impacts on the detector (X, Y) with the relations

$$x = \frac{X}{M} \quad (8) \quad \text{and} \quad y = \frac{Y}{M}. \quad (9)$$

The z coordinate can be derived from the cumulative number of detected ions, which is proportional to the evaporated layers. Consequently, the depth can be analysed [43].

The 3D reconstruction of the specimen begins with the TOF mass spectrum. A mass spectrum is a histogram that depicts the distribution of the mass-to-charge ratio of collected ions. Typically, there are peaks that correspond to specific ions. Perfect mass resolution would result in mass peaks with a Dirac distribution. However, the accumulation of the errors described in the following section 2.4.7, regarding voltage, energy, timing and space inaccuracy, shapes the mass peaks to a Gaussian form with a standard deviation according to the accumulated errors. The resolution of a mass spectrum is defined as the range of each class in the mass spectrum. Increasing ranges (i.e. rough resolution) of multiple classes lead to artificial peak broadening and peak overlapping. The mass resolution is used to assess the quality of the mass spectrum. It is given as $M/\Delta Mx\%$ where $\Delta Mx\%$ is the width of the mass peak at $x\%$ of the maximum peak height (usually at 50%, 10% and 1% of the maximum of the peak). The mass resolution is

2 Theoretical background

dependent on the accuracy of measurements (TOF and voltage), geometrical (flight length) and physical factors (sample temperature). Optimising measures can be taken by either hardware (e.g. reflectrons) or post-analysis software treatment (see section 2.4.7) [43].

The identification of peaks requires preceding knowledge about the investigated material and the natural abundance of isotopes. Peak identification is necessary because it allows the precise calibration of the mass spectrum previous to the reconstruction. Typically, the calibration is done for each measurement separately, because small, unavoidable variations in the flight length from one analysis to another shift the spectrum and the magnification depends directly on the flight length [43].

The definition of mass ranges is a user-defined parameter and has non-negligible influence on the measured concentration. Hence, well-defined methodologies need to be implemented for the definition of the mass range to minimise user-based errors. On average, the precision of the user-measured concentration decreases as the absolute level of the element decreases [43]. This effect must be taken into account when assessing the final uncertainty of the measured composition. Automated methods could largely reduce the deviation of measured and actual concentration, but these methods are not widespread in the APT community. Manual peak identification is often preferred because of the possible ambiguity of peaks and the necessity of previous knowledge about the investigated material [43].

The charge of the detected ions depends on the occurrence of post-ionisation, which was presented in further detail in section 2.4.4. A given species could then be detected as ions with different charges or in some cases as molecular ions. The latter may be the result of chemical reactions under the high electrical field on the specimen surface with residual molecules from the vacuum chamber (e.g. hydrogen). Their original molecular bond may also be too strong to be broken under the electric field. In order to determine the chemical composition of the sample, each peak should be identified and the mass ranges defined accordingly. In case of peak overlaps, peak deconvolution should be performed, based on the natural abundance of isotopes. For this correction, the expected amount of isotopes can be calculated from its natural abundance. The remainder of ions at the overlap position is attributed to the other species and simply calculated by subtracting the amount of the first one [43].

Background noise and mass resolution also have an influence on the accuracy of the analysis. The former stems from the random detection of ionised gaseous atoms or molecules from the inside of the analysis chamber or from atoms or molecules that are adsorbed at the specimen surface. The detection of such species leads to a random, time dependent contribution to the mass spectrum. Therefore, analysis conditions have an influence on the quality of the outcome. A higher detection rate will always reduce the mean level of background noise. Although the contribution of the background to the peak of a major element is weak, this is not the case for minor elements (e.g. trace elements). For the accurate measurement of these elements, the contribution of the noise can be taken into account by applying automated background subtraction. Procedures for background subtraction are available in commercial software. Some estimate the background based on a fit of a Poisson distribution, others are based on iterative procedures.

The different procedures of background subtraction may also contribute to the uncertainty of the measured composition. The detection limit of APT is defined as the lowest concentration that can be measured experimentally. It is closely related to the mass resolution, the background level of the mass spectrum and the total ion count in the analysis. A critical factor for the detectability is the signal-to-noise ratio. It assumes that the peak is inherently different from the noise, which makes the peak distinguishable from the background level [43].

2.4.7 Potential measurement errors and corrective measures

The degradation of mass resolution is dependent on many factors, including the shank angle (see section 2.4.3) and thermal conductivity of the specimen, the wavelength of the laser, its beam intensity and focalisation. The origins of the mass spectrum degradation are linked to measurement performance errors or intrinsic physical limitations. These sources of errors are in turn divided into TOF errors, energy or voltage errors and flight length errors. TOF errors are rooted in the time that elapses between the voltage or laser pulse and the emission of ions from the tip and the precision of the electronic system. At each generated pulse, a detection window is opened, which is the duration for the detection of ions. If an ion arrives at the detector during this detection window, its TOF can be calculated. It corresponds to the time between the opening of the detection window and the moment the signal is detected. However, a time offset between the opening of the detection window and the actual application of the pulse to the specimen exists. The actual TOF is obtained by correction of the measured TOF t_m by the time offset t_0 . The determination of the time offset plays a crucial role in estimating the accurate flight length, which has a direct influence on the position of the mass peaks. According to equation 2, the proper flight length can only be determined if the time offset is known:

$$\frac{m}{n} = 2eV \left(\frac{t_m - t_0}{L} \right)^2. \quad (10)$$

With knowledge about the flight length, the mass spectrum can be fitted so that the mass peaks are located at their expected position. In practice, at least two mass peaks are selected for the calibration of t_0 and L [43].

The electric or thermal pulses that are superimposed to the standing electric field V_0 lead to the evaporation of ions. However, these pulses may generate energy deficits. Atoms may evaporate on the falling edge of pulses, i.e. at a smaller potential energy, which contributes to the degradation of mass resolution [43]. This is common for measurements in laser mode, where the thermal conductivity of the specimen is rather low due to its limited cross-section. While the laser pulse induces a sharp temperature increase, the decrease in sample temperature is gradual (see section 2.4.4). As a result, the evaporation of surface atoms continues well after the laser pulse. This phenomenon is mirrored in the mass spectrum of laser mode measurements. The mass peaks are enlarged by the succession of so-called thermal tails [43]. A comparison of a

2 Theoretical background

voltage spectrum to a laser spectrum of the investigated alloy is shown in figure 14. The thermal tails in the laser spectrum are visible in figure 14 b.

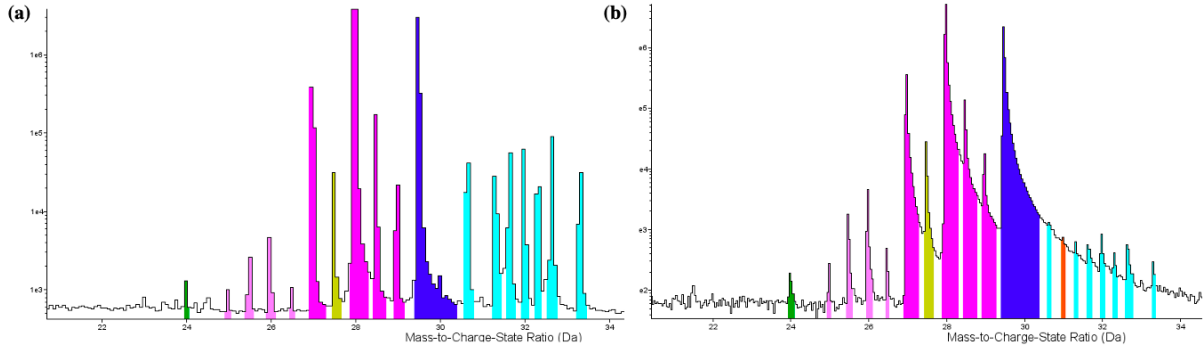


Figure 14: (a) Part of a mass spectrum from a voltage-mode measurement.
(b) Same part of a mass spectrum from a laser-mode measurement.

Equation 2 neglects acceleration effects that occur close to the specimen tip. In reality, the ions are accelerated through a time-varying field, which can result in uncertainty about their kinetic energy as well as their timing. When an ion leaves the sample surface, it is accelerated towards the detector. However, this acceleration is not instantaneous. The voltage of the tip changes slightly during acceleration, so the ion does not acquire the full expected energy. Accordingly, the ions with the maximum kinetic energy are not the ones that evaporated at the maximum of the pulse but an instant before the maximum. As a result, the energy deficit distribution is distorted [43].

Due to the flatness of the detector, the flight length is not constant over the detector surface. For a perfectly planar detector that is situated at the distance L_0 from the specimen tip, the actual distance can be calculated with the Pythagora correction $L^2 = X^2 + Y^2$. This correction is not only necessary to determine the real flight length of the ion (i.e. mass spectrometry) but also to calculate its original position in the specimen. In reality, this correction is insufficient to achieve an optimal correction. A minor misalignment of the tip, a small tilt of the detector or the use of electrostatic devices to enlarge the field of view causes a serious distortion of the Pythagora correction. In practice, the detector is divided into a grid, in order to correct flight length variations. The mass spectrum is calculated for each cell, in which the variation of flight length is small. In order to adjust the mass peaks at their correct positions, a mass window is selected on a defined peak with the average value for the mass. From the average mass value, a correction factor is derived to restore the peak at its correct position. The entirety of atoms is then recalibrated with this correction map [43].

The use of a local electrode in modern LEAP systems is a major improvement. The local electrode is a grounded counter electrode, in front of which the specimen is placed. Ions pass through a hole in this local electrode and fly to the ion detector that is located a few centimetres away.

2 Theoretical background

This results in an amplification of the electric field generated at the specimen tip. Commercial LEAP instruments use a standard local electrode with a $40\ \mu\text{m}$ diameter aperture. The distance of the tip to the local electrode is in the same order. Using a local electrode also minimizes the impact of dynamic effects. Both the acceleration distance and the acceleration duration can be reduced by one order of magnitude and as a result, the maximum kinetic energy coincides with the maximum of the voltage pulse [43].

In order to minimise mass spectrum degradation, an energy deficit compensation system, called reflectron (see figure 15), is implemented into the instrument. This compensation system improves mass resolution by elongating the flight paths and simultaneously reduces background noise in mass spectra, which results in an increase in the sensitivity threshold. The reflectron creates a static electric field in a defined region of the ion flight path to reverse the travelling direction of the ion. In its simplest design, a reflectron consists of two electrodes with a homogeneous electric field between them. Within the homogeneous electric field, the ion trajectory is a parabola. However, planar reflectrons have limited collection angles and suffer from severe chromatic aberration effects. The solution to these shortcomings was introduced with the invention of the curved reflectron, which acts as a spherical mirror for ions entering the device. It produces a compression of ion trajectories on the detector by producing a spherical potential distribution between two concentric spherical electrodes, one of which is grounded. Ions with the same entrance angle but slight differences in kinetic energy are spatially focused onto the detector [43, 45]. However, the detection efficiency of a LEAP incorporating a curved reflectron is $\sim 30\%$ lower than that of a LEAP without such a reflectron [52].

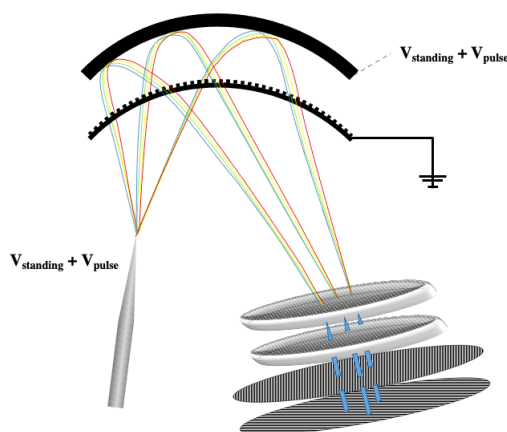


Figure 15: A curved reflectron improves the mass resolution by elongating the flight path and corrects chromatic aberrations in new LEAP generations (cf. [43]).

The spatial resolution of atoms evaporated in a regular manner is some tenths of nanometres along both the analysis and lateral directions, whereby the resolution along the direction of analysis is better than in the perpendicular directions. Therefore, the concentration profile of a heterogeneous interface is most accurate when the interface is oriented perpendicularly to

2 *Theoretical background*

the direction of analysis. However, the resolution is considerably worse close to interfaces that separate regions with different evaporation fields. The degradation occurs because of local magnification effects and trajectory aberrations. Local magnification effects are the result of local variations of the evaporation field. These variations are characteristic for areas with sharp chemical gradients (segregations) or interfaces between different phases. As a consequence, the local composition of nanoparticles may be biased by the surrounding matrix, which can lead to severe image distortion of the particle shape. Simulations of ion trajectories can help to correct these aberrations and image distortions [43].

Furthermore, a compromise between mass resolution and field of view must be made. On one hand, a longer flight length produces a higher mass resolution due to a greater difference in TOF. On the other hand, a long flight length decreases the field of view for techniques relying on projection on the detector. The implementation of reflectrons and local electrodes also helps to remedy this compromise.

3 Experimental

3.1 Investigated material

The investigated material is a FeCoMo alloy with the following nominal composition:

Table 1: Nominal chemical composition of the investigated alloy.

	<i>Fe</i>	<i>Co</i>	<i>Mo</i>	<i>Si</i>	<i>C</i>
wt.%	Bal.	25.3	15.2	0.2	0.02
at.%	Bal.	25.1	9.3	0.4	0.1

The powder particles used for LPBF of the investigated specimens were gas atomised with N_2 , which resulted in a spherical particle shape. The powder was sieved to a particle diameter range of 15 – 45 μm . Powder atomisation and sieving were carried out at voestalpine Böhler Edelstahl GmbH & Co KG, Kapfenberg, Austria.

The process parameters for the LPBF process are given in table 2, where P_L is the laser power, h the hatch distance, v the scanning speed and D the powder layer thickness. The VED was calculated from these parameters according to equation 1. Ar with an O -content of $< 0.1\%$ was used as inert gas in the LPBF-process as well. Specimen cuboids of different heights (step-specimens: $T_{Pnone300}$, $T_{Pnone400}$ and $T_{Pnone500}$) were produced at Politecnico di Milano, Milan, Italy with a Renishaw AM250 machine. The specimen height is given by the number of fused powder layers (300, 400 and 500 layers, respectively). Additionally, two specimens from one build job (T_{P50002} and T_{P50003}) with platform preheating temperature $T_P = 500^\circ\text{C}$ were produced at voestalpine Additive Manufacturing Center GmbH, Düsseldorf, Germany with a SLM 280HL machine, see table 2. These specimens had a built height of ~ 15 mm.

Table 2: Process parameters of the LPBF-specimens.

	P_L [W]	h [μm]	v [mm/s]	D [μm]	VED [J/mm ³]	T_P [$^\circ\text{C}$]	machine
step-spec.	200	90	800	40	69.4	none	Renishaw AM250
T_{P50002}	135	80	500	30	112.5	500	SLM 280HL
T_{P50003}	135	140	500	30	64.3	500	SLM 280HL

3.2 Heat treatment variations and hardness measurement

Table 3 lists the conducted heat treatment variations of conventionally manufactured (HIP) rod-material and the LPBF specimens $T_{Pnone300}$ and T_{P50003} . These were carried out in order

3 Experimental

to study the hardening-potential of as-built specimens. The solution annealing treatment was done at 1180 °C and held for 10 minutes. Subsequently, the specimens were water-quenched. The ageing treatment was carried out at 560 °C for 3 h with subsequent air-cooling.

Table 3: Heat treatment variations of conventional material (HIP), $T_{Pnone300}$ and T_{P50003} specimens.

	Solution annealing (SA) 1180 °C/10 min/ H_2O	Ageing 560 °C/3 h/air	Final condition
HIP	no	no	soft annealed
HIP	yes	no	SA
HIP	yes	yes	SA and aged
$T_{Pnone300}$	no	no	as-built
$T_{Pnone300}$	yes	no	SA
$T_{Pnone300}$	no	yes	aged
$T_{Pnone300}$	yes	yes	SA and aged
T_{P50003}	no	no	$T_P = 500^\circ\text{C}$ as-built
T_{P50003}	yes	no	$T_P = 500^\circ\text{C}$ SA
T_{P50003}	no	yes	$T_P = 500^\circ\text{C}$ aged
T_{P50003}	yes	yes	$T_P = 500^\circ\text{C}$ SA and aged

The HRC150 hardness was measured with a EMCO-Test N3A 15 machine from Prüfmaschinen GmbH, Kuchl, Austria. On each specimen, five indents were made, of which the highest and lowest values were dismissed in order to minimise the potential error caused by the defects inherent to LPBF, i.e. cracks and pores.

The heat treated specimens were ground and subsequently polished to 1 μm with a Struers Tegramin. Afterwards, they were prepared with Struers OPS-Nondry for 2 minutes with 20 N on a Struers Tegramin to enhance the contrast for the SEM BSE-mode. The microstructural analysis was conducted with a Tescan Clara SEM.

3.3 Microstructure and hardness of as-built specimens

In order to investigate potential microstructural differences in dependence of the specimen height caused by the nature of the LPBF process (e.g. in-situ ageing, remelting, etc.), SEM micrographs were taken from the last layer and the middle position of the as-built specimens with a Tescan Clara SEM. The preparation of the as-built specimens for high magnifications in SEM turned out to be quite challenging. In trying to visualise the solidification structure from LPBF, multiple preparation techniques were applied, see table 4. All techniques were conducted at room temperature (RT).

3 Experimental

Table 4: Preparation techniques for SEM.

Technique	Time [s]	Temperature [°C]	Machine	Additional information
Polishing	180	RT	Struers Tegramin	1 μm /Struers Nap
OPS-polishing	30	RT	Struers Tegramin	OPS Struers-Nondry
WII-etching	1	RT	-	20% WII etchant
Electropolishing	40	24	Struers Lectropol	Struers A3/0.5 cm ² /16 V/flow rate 11

Electropolishing proved to be the most suitable technique to visualise the solidification structure. However, the outcome was still not ideal, as the etching attack on the $TP500_{02}$ specimen was insufficient under the mask and the SEM micrograph had to be taken from the over-etched area in the top layer. For the middle section of the $TP500_{02}$ specimen, the diluted W2 etch was most suitable, however surface deformation was difficult to remove.

The μ -phase, which precipitates in the investigated FeCoMo alloy during ageing, causes a significant increase in hardness. Hence, the IHT effects during LPBF were investigated with hardness measurements over the specimen height. Due to the high density of cracks and pores in the $TPnone_{500}$ and $TP500_{02}$ specimens, their HV1 hardness at various distances from the top layer was measured with a QNess Q60A+ hardness tester. Figures 16 a and b show LOM micrographs (M=12.5) of the HV1 indents. These bright field micrographs were obtained with a Zeiss Axio Imager 2.

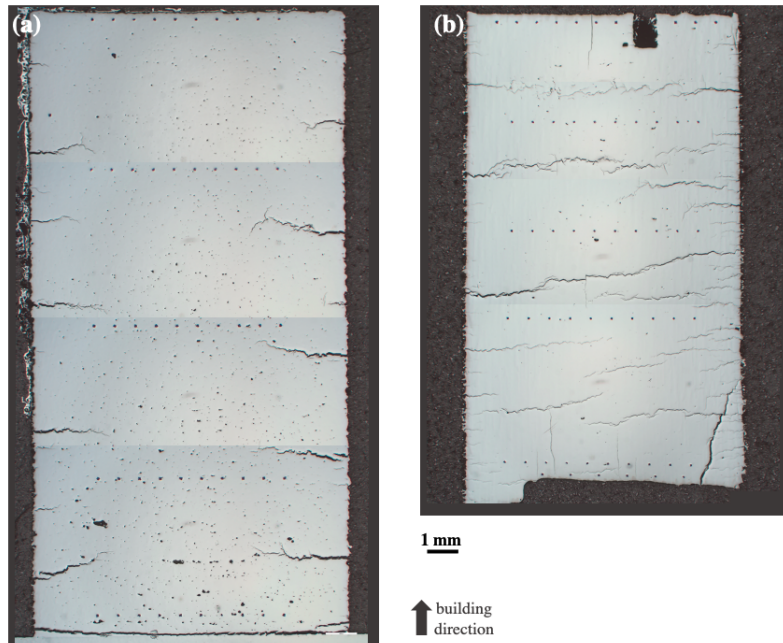


Figure 16: LOM micrographs (M=12.5) of the HV1 indents in the (a) $TPnone_{500}$ and (b) $TP500_{02}$ specimens.

3.4 Preparation of as-built specimens for APT

The specimens for APT were prepared using the electrolytic method, except for the top layer. In order to guarantee the analysis of only the top layer, i.e. an area that has not experienced IHT, the specimen tips from that position were prepared using FIB technology.

3.4.1 Electrolytic preparation

Figure 17 a shows the positions in the specimens $T_{Pnone400}$, $T_{Pnone500}$ and T_{P50002} , from which APT tips were prepared. The distance of a tip from the top layer is given by x . From the investigated positions with $x \neq 0$, specimen blanks with $\sim 0.4 \times 0.4 \times 10 \text{ mm}^3$ were cut according to figure 17 b and c. A Struers Accutom-5 machine and a cubic boron-nitride (CBN) BOC13 cut-off wheel were used for cutting. The cutting speed was set to 0.010 mm/s.

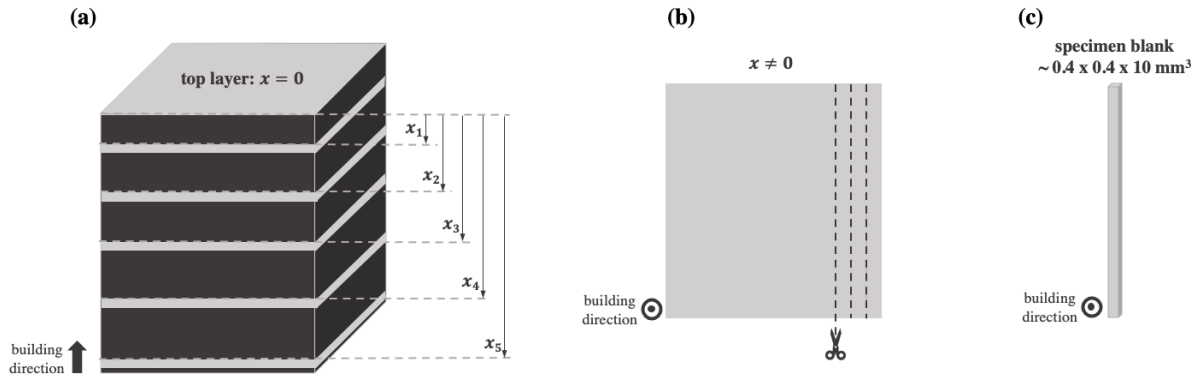


Figure 17: (a) Selection of the positions of APT-specimens in the cuboid.
 (b) Cutting of specimen blanks.
 (c) Specimen blank ready for electrolytic preparation for APT.

The tips were electrolytically prepared at RT in a mixture of 25% perchloric acid in acetic acid (electrolyte 1) for the first step and 98% 2-butoxyethanol–2% perchloric acid (electrolyte 2) for the second step. Both steps were performed with the microloop method and the specimen was rinsed with 2-propanol between the polishing steps. For neck-formation (step 1, see figure 18 a, b), voltages in the range of 11 – 12 V were applied, which were reduced to 6 – 7 V to break the neck (step 2, see figure 18 c, d).

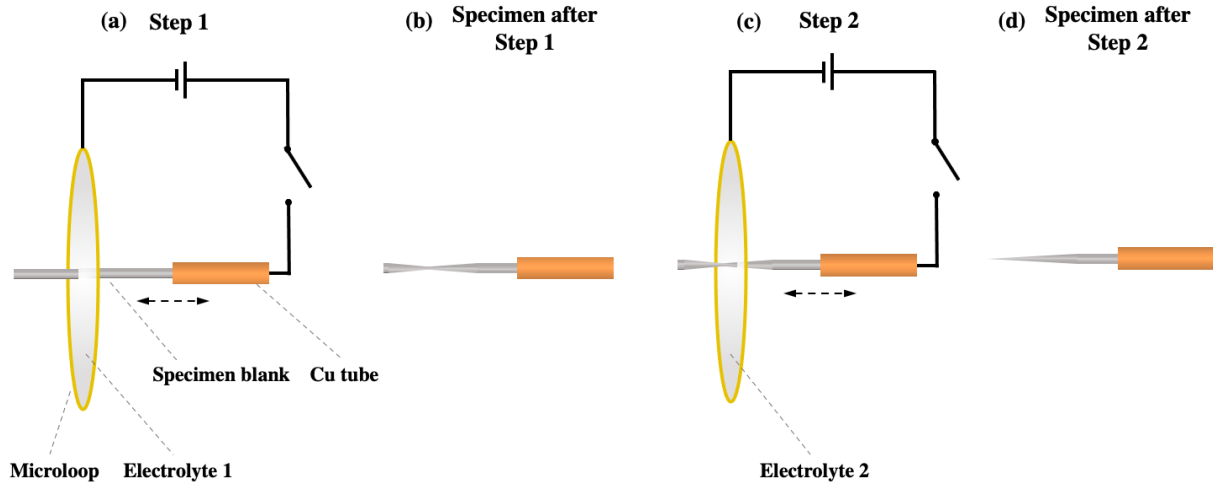


Figure 18: Schematic sequence of the electrolytic preparation using the microloop method for both polishing steps:

- (a) Neck-formation in the specimen blank.
- (b) Specimen blank with neck.
- (c) Controlled breaking of the specimen neck.
- (d) Specimen ready for insertion into the LEAP.

3.4.2 FIB preparation

The targeted preparation of the top layer ($x = 0$) was done with a FIB Versa 3D from Thermo Fisher Scientific. Figures 19 a–d show SEM images of the FIB lift-out preparation sequence. For this purpose, the top parts from the $Tpnone400$ and the $Tp500_{02}$ specimens were embedded in Struers Polyfast, ground and polished to $1\ \mu\text{m}$ and OPS-polished for 30 s with Struers OPS Nondry. After the location of the last layer was determined with SEM SE-contrast, a Pt capping layer was deposited to protect the ROI, see figure 19 a. Trenches were cut around the ROI to form a lever, see figure 19 b. Then, the omniprobe was inserted into the chamber and welded onto the lever with Pt . The last wall was cut free and the lever was split up into three tips, which were welded onto a needle pad. Subsequently, the tips were coarse milled, see figure 19 c. During cleaning (i.e. milling with lower energy to avoid Ga implantation), the Pt capping layer was removed, as shown in figure 19 d.

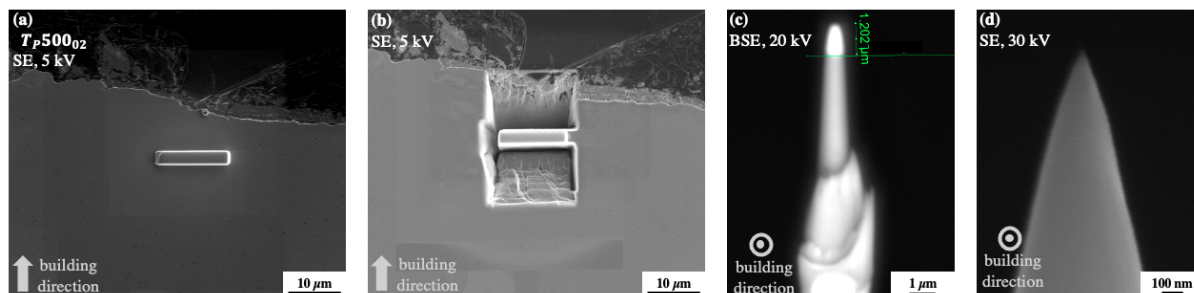


Figure 19: FIB preparation sequence:

- (a) Selection of ROI, after *Pt* capping layer deposition (SE).
- (b) ROI lever with trenches before lift-out (SE).
- (c) Coarse-milled tip mounted on a needle pad with *Pt* capping layer (BSE).
- (d) Final tip after cleaning (SE).

3.5 APT measurement of as-built specimens

APT measurements were carried out with a Cameca LEAP 3000X HR system. In order to access a large volume of material and to reduce the risk of specimen-fracture compared to voltage mode APT measurements, the laser mode was used. The analysis temperature was set to 40 K and the residual gas pressure in the chamber was $\sim 3 \cdot 10^{-11}$ torr ($\sim 4 \cdot 10^{-9}$ Pa). A laser power of 0.6 nJ and an evaporation rate of 1% were chosen for all measurements.

For comparison, one measurement was carried out in the voltage mode ($T_{Pnone500}$, $x = 3$ mm). The analysis temperature was set to 60 K and the residual gas pressure was $\sim 4 \cdot 10^{-11}$ torr ($\sim 5 \cdot 10^{-9}$ Pa). A target pulse fraction of 20%, an evaporation rate of 0.5% and a pulse frequency of 200 kHz were chosen.

3.6 APT reconstruction and analysis

The reconstruction of the specimen tip-geometry and the analysis of APT measurements was done with the “Integrated Visualisation and Analysis Software” (Imago IVAS 3.6.14). Figure 40 in the appendix shows the reconstruction sequence in IVAS. The standing voltage-curve during the measurement was used for the reconstruction of the tip geometry (cf. section 2.4.3). Discontinuities at the beginning of the measurements due to roughness-peaks being smoothed away were cropped out of the voltage curves, see figure 40 a. The selection of the part of the measurement used for the analysis was chosen in a way that the background history did not exceed 100 at any time, see figure 40 b. Next, the detector ROI was aligned based on the detector event history, see figure 40 c. TOF correction was performed to sharpen the mass peaks by iteratively running the voltage-correction (non-linear effects) and the bowl-correction (flight-path), see figure 40 d. The next step in the reconstruction concerned the fitting of the mass spectrum. For

3 Experimental

this purpose, three distinct peaks (Fe^{2+} , Si^{2+} and Mo^{2+}) were identified in the mass spectrum, see figure 40 e–g. The whole spectrum was then fitted, taking into account the positions of these selected peaks, see figure 40 h. In the final step of the reconstruction, ionic species were allocated to their characteristic peaks, see figure 20.

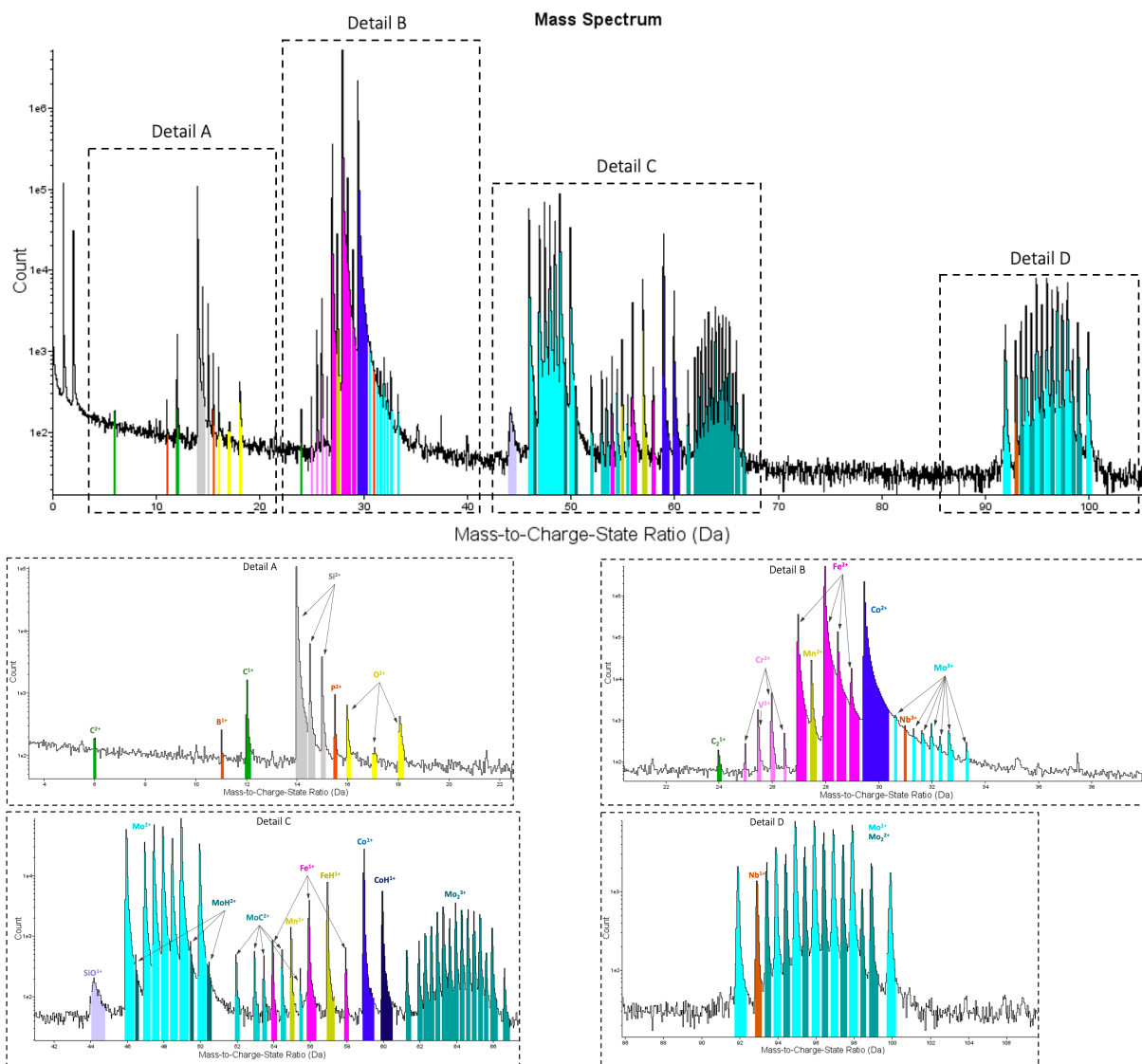


Figure 20: Ion species allocated to their corresponding peaks in the mass spectrum (laser mode). Mass spectrum overview and details A–D from the mass spectrum.

For comparison, the mass spectrum of the voltage mode measurement is shown in figure 41 in the appendix. Note that the thermal tails are much less pronounced and hardly any molecular ions were detected in the voltage measurement compared to the laser measurement.

For the analysis of reconstructed specimens, various functions included in IVAS were applied. In order to visualise precipitates or clusters, isoconcentration-surfaces (isosurfaces) were used. To assess the elemental composition of precipitates, the “atomic” and “decompose complex ions”

3 Experimental

boxes were checked. With this command, IVAS creates surfaces in those areas, where the concentration of the given element equals the given isoconcentration-value. The concentration of the element on either side of an isosurface is higher or lower than the isovalue, which is useful for the quick assessment of enriched or depleted areas. For a closer chemical analysis of precipitates, proximity histograms (proxigrams) are a suitable analysis tool. In a first step, element-interfaces are created from the isosurfaces. A proxigram can be then created with the location of the interface at the origin. The concentration of each species is calculated perpendicularly to the interface in both directions. The mean concentration values and standard deviations over the distance from the interface are then plotted in the proxigram. Hence, a concentration profile for each elemental species is created from an element-interface. Proxigrams can provide insight into the composition of precipitates and their surrounding matrix. In order to determine the width or diameter of a precipitate, cylindrical ROIs can be of use. The ROI should be placed in a way that the cylinder top is roughly perpendicular to the isosurface. A 1D concentration profile can then be calculated along the z -axis of the cylinder and the precipitates width can be estimated. The precipitate size distributions (PSDs) at different x in the $TP500_{O_2}$ specimen were visualised by exporting the interface values of 20 at.% Mo interfaces in a $60 \times 60 \times 150 \text{ nm}^3$ volume from the APT reconstruction. Unbound interface volumes were filtered for this purpose. From the surface area A and the volume V of a precipitate, two radii were calculated under the assumption of spherical precipitates: $R_{surface} = \sqrt{\frac{A}{4\pi}}$ and $R_{volume} = \sqrt[3]{\frac{3V}{4\pi}}$. An equivalent radius R was calculated as the mean value of $R_{surface}$ and R_{volume} . The precipitates were then categorised into intervals of $\Delta R = 0.2 \text{ nm}$. The number of precipitates of each interval was plotted as a histogram over their size.

The volume renderer in the right click menu of an elemental isosurface has proven useful for visual comparison of precipitation stages at various x . By linking the concentration of an element in a voxel to that voxels RGB-value and opacity, elemental clustering and precipitation can be visualised. Mo -volume rendering was applied to detect spinodal decomposition and μ -phase precipitation.

3.6.1 Spatial distribution mapping

Spatial distribution maps (SDMs) make use of the interatomic positions vectors in an APT dataset and exploring the vicinity of individual atoms. The offsets between reconstructed neighbouring atoms are recorded from zero to a defined maximum distance. In order to detect clustering, SDMs including only the vectors of specific species can be created [53]. For the investigation of μ -phase precipitation during LPBF, SDMs containing the vectors of Mo , Mo_2 and MoC were created. MoH peaks were also taken into account, but H was removed before further analysis. The Mo -ions were selected and the maximum distance was set to 5 nm. 1D and 2D SDMs were rendered, which represent histograms of the relative positions between atoms. In the case of 2D SDMs, the ion count is represented by RGB-values.

3.6.2 Cluster search

As fine-scaled μ -phase precipitates and early-stage solute clustering is expected to occur in the investigated material, the maximum separation algorithm was applied in IVAS. This algorithm comprises of three data-mining steps. First, a clustering algorithm identifies solute clusters of selected species in the data, see figure 21 a. Then, an enveloping algorithm identifies atoms of other elements that are part of the solute cluster, see figure 21 b. Finally, an erosion algorithm erodes the particle-matrix interface, which was formed by the enveloping algorithm, see figure 21 c. Statistical methods can then be applied to investigate the cluster properties, e.g. size, distribution and chemical composition [54, 55]. Besides the enveloping distance and the erosion distance, the algorithm requires input parameters regarding the maximum separation distance between clustered atoms d_{max} and a minimum number of clustered atoms to be considered as a cluster N_{min} , i.e. a minimum cluster size.

The maximum separation algorithm was applied to Mo and its molecular ions (Mo_2 and MoC), Si and C , respectively. Si - and C -clustering was investigated because the Mo -cluster search was inconclusive and Si and C are known to accumulate in μ -phase precipitates [56]. In order to find a suitable d_{max} , a nearest neighbour (NN) search was applied (see figure 21 d). For the Mo -NN search, the order was set to 10 (10NN), i.e. the distance to the 10th nearest neighbour was calculated. The 10NN search was also done for Si and a 3NN search was done for C . The sample width for the Mo and Si 10NN search was set to 0.01 nm and 0.06 nm for the C 3NN search. The resulting NN distribution consists of two graphs, one for the dataset (black) and one for a randomised distribution (red), see figure 22 a. The intersection of these two graphs yields d_{max} for the maximum separation algorithm. With this d_{max} , a cluster size distribution was created and N_{min} was established. Figure 22 b depicts that clusters larger than N_{min} are no longer expected in a random distribution. With these input parameters, a cluster size analysis was then launched.

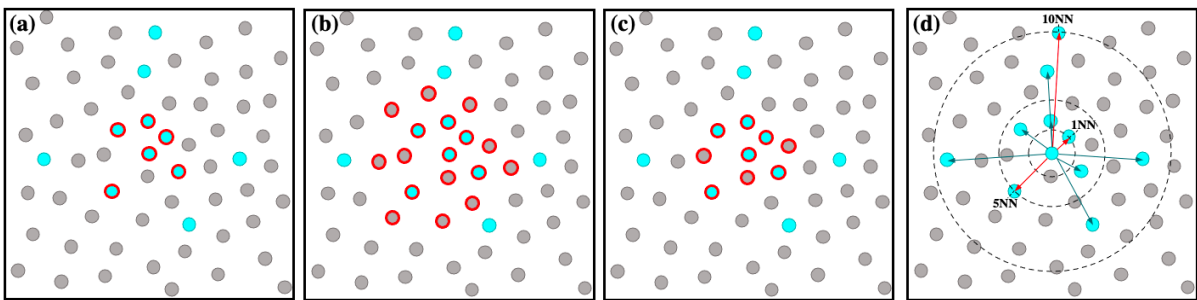


Figure 21: (a–c) Schematic sequence of the maximum separation algorithm (cf. [53]):

- (a) Solute atom selection with the clustering algorithm.
- (b) Selection of other atoms with the enveloping algorithm.
- (c) Erosion algorithm.
- (d) 1NN, 5NN and 10NN distances in an APT dataset (cf. [54]). The respective d_{max} are presented with red arrows.

3 Experimental

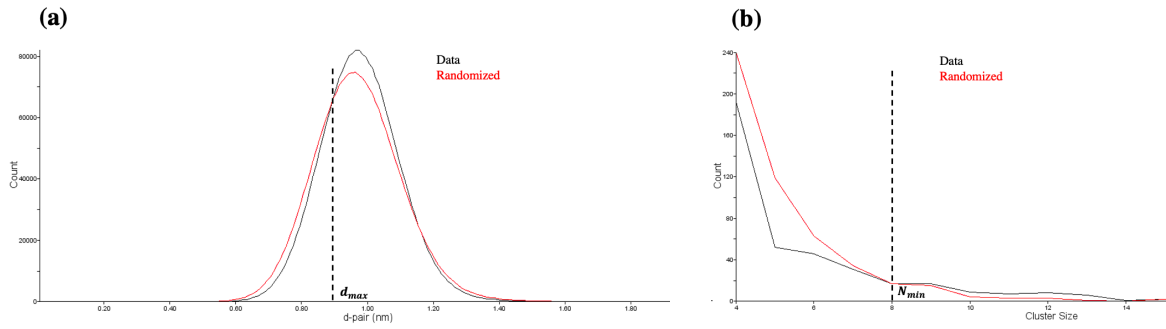


Figure 22: (a) NN distribution and deduced d_{max} .
 (b) Cluster size distribution and deduced N_{min} .

3.6.3 Tip profile-based reconstruction from SEM image

A tip profile-based reconstruction from a SEM image was done for one FIB-prepared specimen in order to examine the differences in tip geometry compared to the conventional voltage-based reconstruction. Figure 23 shows the reconstruction window in IVAS, where the “Tip Profile” tab has been selected. The SEM image of a FIB-prepared tip profile has been uploaded to the program. Initially, the diagram on the right is blank. First, the scale factor was calibrated by tracing the scale on the image and entering the length of the scale. Then, the cone diameter of the tip profile is traced at increasing distances from the tip apex to establish the evolution of the tip profile. Consequently, the graph on the right describes the cone radius. Its evolution is rendered automatically.

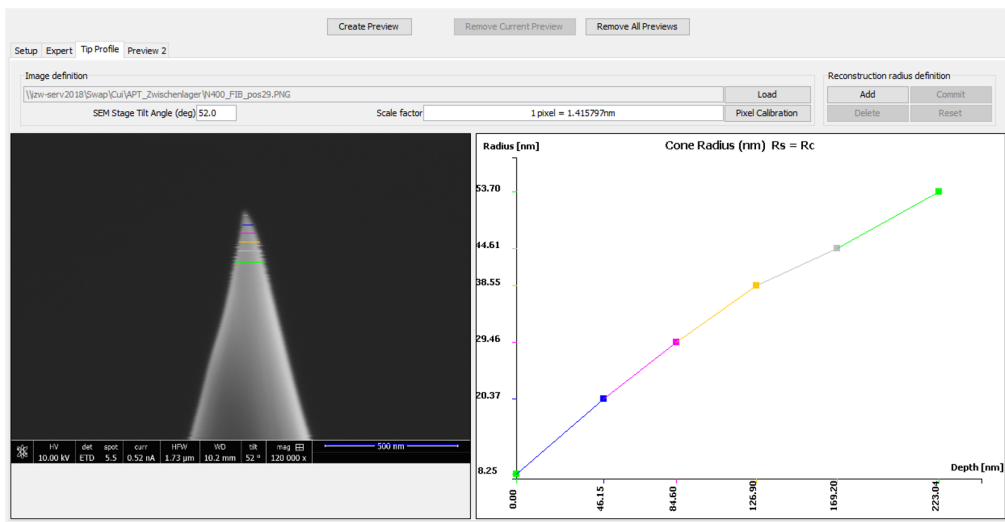


Figure 23: APT reconstruction based on a SEM image of the tip profile in IVAS.

3 Experimental

The tip profile-based reconstruction was done for the FIB-prepared $T_{Pnone400}$ specimen at $x = 0$ mm and compared to the voltage-based reconstruction. Afterwards, it was attempted to adjust k_f in the voltage-based reconstruction in a way that the result resembles the tip profile-based reconstruction. The most promising value for the FIB prepared specimens was $k_f = 4$. The k_f for some other measurements of interest was adapted to $k_f = 4$.

3.7 Dilatometer measurements

A nominal preheating temperature of 500 °C was applied during one of the investigated LPBF processes. However, the martensite start temperature M_s of the conventionally manufactured material is lower than that (~ 380 °C). During LPBF with nominal $T_P = 500$ °C, the material rapidly solidifies and is ideally quenched to 500 °C. It is then held at that temperature until the LPBF process is finished. Hence, it was of interest whether precipitation could have occurred during such a LPBF with $T_P = 500$ °C. For that reason, dilatometer measurements were carried out at voestalpine Böhler Edelstahl GmbH & Co KG, Kapfenberg, Austria. Four heat treatment variations were performed with soft annealed HIP material. The temperature profiles of the heat treatments are shown in figure 24 a. After solution annealing at 1180 °C for 10 min under vacuum, the specimens were quenched linearly to 500 °C with *Ar* gas. The dwell times at 500 °C were 1, 10, 30 and 60 min under vacuum. The specimen geometry is schematically depicted in figure 24 b. After the dilatometer measurements, the HV hardness was measured in order to determine whether precipitation occurred from the austenite phase during dwelling at 500 °C. The influence of the dwell time on M_s and martensite finish temperature M_f and the correlation to the precipitation behaviour were also of interest. It should be noted, however, that the LPBF process differs from the dilatometer measurements with conventionally produced rod material in three main ways. Firstly, the material solidifies from the melt during LPBF, which is not possible to imitate in the dilatometer. Secondly, the cooling rate during LPBF may be considerably faster (up to 10^7 K/s [31]) than quenching with *Ar* can provide and thirdly, the IHT during LPBF was not considered in the dilatometer measurements.

3 Experimental

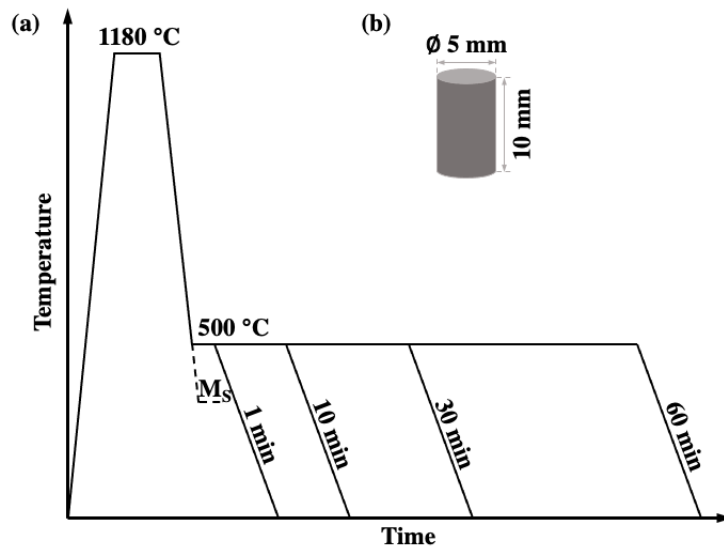


Figure 24: (a) Temperature profiles for the dilatometer measurements.
(b) Specimen geometry of dilatometer specimens.

4 Results

4.1 Microstructure and hardness

The mean hardness values (HRC) of the differently heat-treated samples are shown in figure 25, along with exemplary SEM-BSE micrographs of the microstructures. The individual hardness values and corresponding heat treatments are given in table 6 in the appendix. Figure 26 shows the SEM-BSE micrographs in higher magnification.

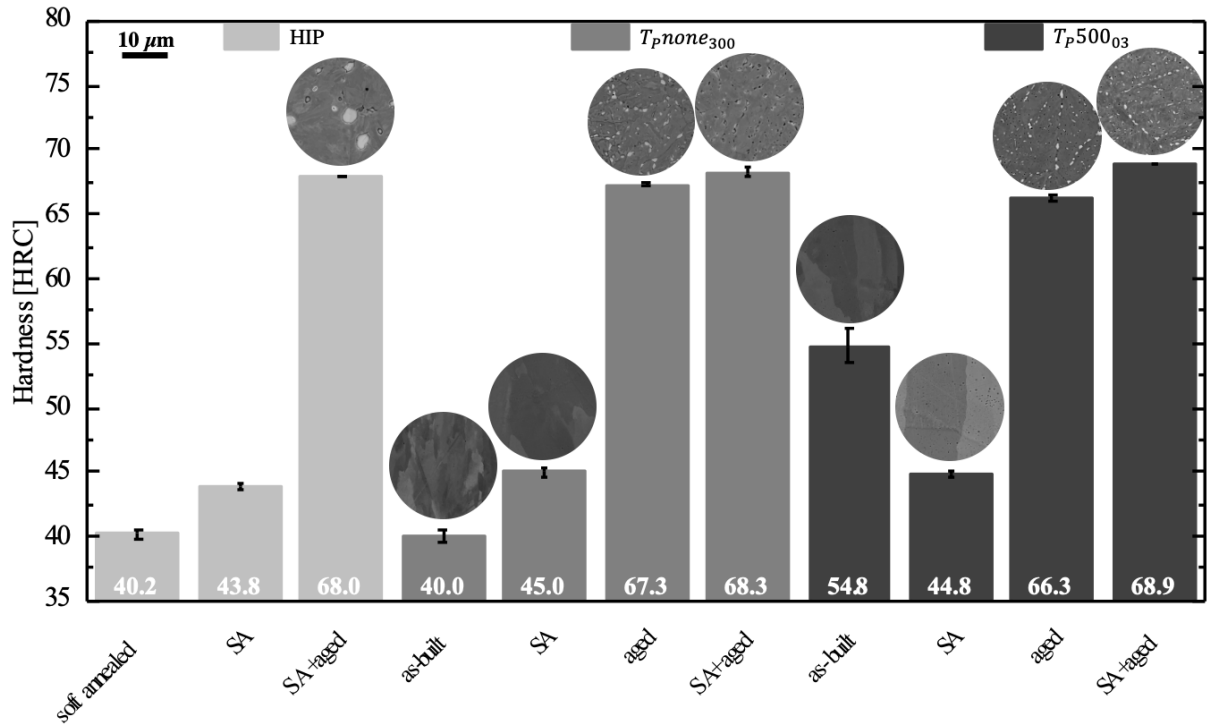


Figure 25: Heat treatments, resulting hardness and corresponding SEM-BSE micrographs (15 kV) of HIP material, $T_{Pnone300}$ and T_{P50003} .

The soft annealed (40.2 HRC) and SA (43.8 HRC) HIP material exhibit low hardness due to the lack of strengthening effect from the μ -phase. These two HIP conditions are not technically relevant and hence no SEM micrographs are depicted. The SA+aged HIP condition (i.e. fully heat treated condition) yields an unsurprisingly high hardness of 68.0 HRC. The SEM micrograph reveals a martensitic matrix with embedded μ phase precipitates. The μ m-sized bright areas are primary μ phase particles, which stem from solidification and attain a globular shape during HIP. The as-built $T_{Pnone300}$ specimens hardness (40.0 HRC) is similar to the soft annealed HIP specimen. The corresponding SEM-BSE micrograph shows the absence of primary μ -phase particles. Similarly, there is no trace of primary μ -phase precipitates in the SEM-BSE micrograph of the as-built T_{P50003} specimen. However, its hardness (54.8 HRC) is markedly

4 Results

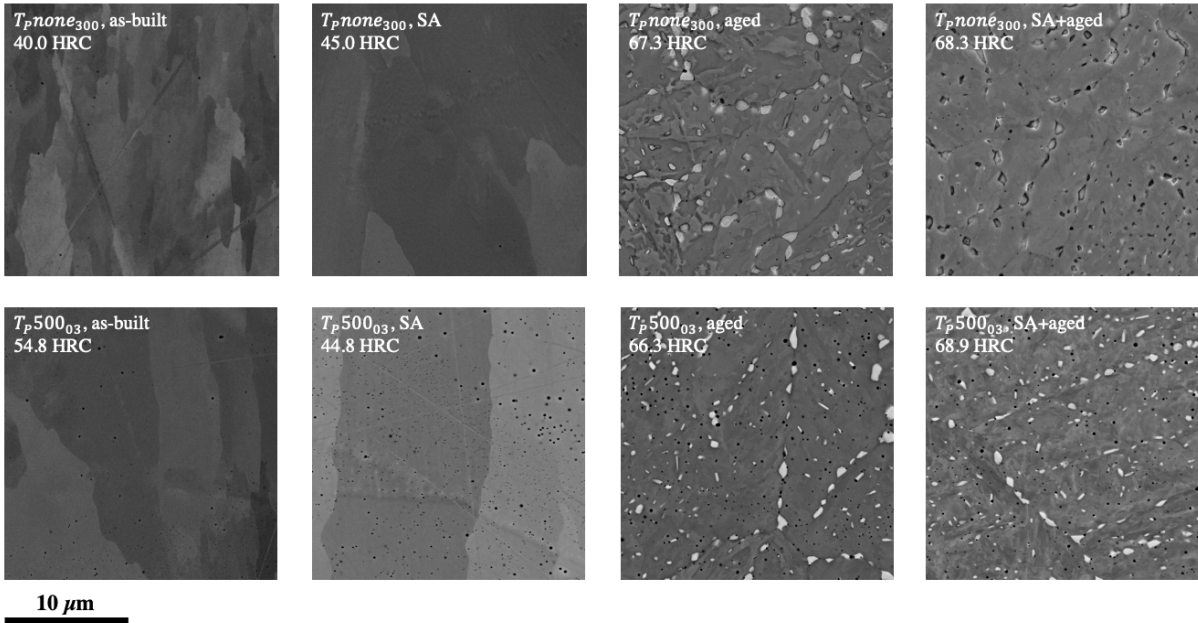


Figure 26: SEM-BSE micrographs of differently heat treated specimens (15 kV).

higher compared to the $T_{Pnone300}$ specimen. Notably, the standard deviation in hardness of the as-built specimen with $T_P = 500^\circ\text{C}$ (± 1.25 HRC) is larger than that of all other investigated specimens (≤ 0.56 HRC).

Aged LPBF specimens experience a significant hardness increase (67.3 HRC and 66.3 HRC, respectively), compared to their as-built counterparts. However, their hardness is lower than the fully heat treated HIP material. While the fully heat treated HIP material exhibits a hardness of 68.0 HRC, the aged $T_{Pnone300}$ specimen reaches 67.3 HRC and the aged T_{P50002} specimen only reaches 66.3 HRC.

LPBF specimens, which underwent both SA and ageing exhibit even higher hardness (68.3 and 68.9 HRC, respectively) than the fully heat treated HIP material (68.0 HRC). It should be noted that the hardness increase is very small, however the standard deviations of all measurements are also very narrow (0.05 HRC, 0.33 HRC and 0.08 HRC, respectively).

The microstructure and hardness of the two as-built specimens were examined in more detail along the building height. Figure 27 shows SEM micrographs of the electropolished $T_{Pnone500}$ specimen. Micrographs of other preparation methods are shown in figures 42 and 43 in the appendix. Figure 27 a and b are micrographs from the top layer, c and d from ~ 7 mm beneath it. In figure 27 a, the weld beads from LPBF are indicated with blue dashed lines. Grain boundaries propagate through the weld bead boundary and the grain continues in the next layer. The overview micrographs (figures 27 a and c) display a wide variation in grain size. Although the overall solidification direction can be made out, some grains solidify angled $\pm 45^\circ$ to the building direction (i.e. orthogonally to the weld bead surface). Others have a much smaller size, which can be seen in figure 27 d. In figures 27 b and d, higher magnifications reveal fine structures

4 Results

within the matrix. Note that these micrographs were taken with secondary electron (SE) contrast. The orientation of these structures is almost parallel within one grain and changes at the grain boundaries.

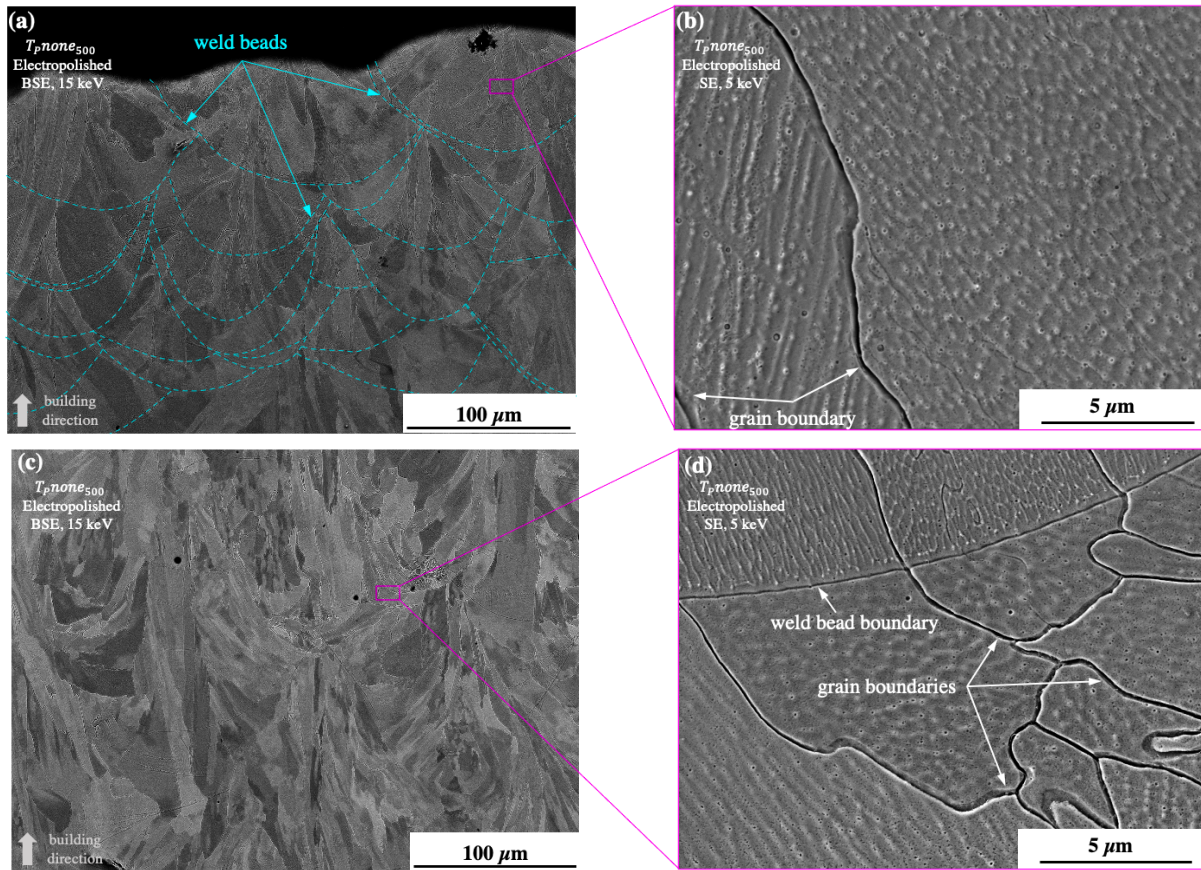


Figure 27: SEM micrographs of the $T_{pnone500}$ specimen after electropolishing:
(a) Top layers with dashed lines indicating the weld beads from LPBF (BSE-contrast).
(b) Top layer (SE-contrast).
(c) Middle section (BSE-contrast).
(d) Middle section with weld bead boundary and grain boundaries (SE-contrast).

The effect of directional solidification caused by partial remelting is even more pronounced in the T_{P50003} specimen, see figure 28. The attack by electropolishing was insufficient under the mask and no structures could be observed there. Hence, the SEM micrographs in figure 28 a and b were taken in the over-etched part of the specimen. The SEM micrographs of the middle section (~ 7 mm beneath the top layer) of this specimen, etched with 20% WII, are shown in figures 28 c and d. Note that the SEM micrograph in figure 28 d was taken with 10 kV, as opposed to the other micrographs with the same magnification, which were taken with 5 kV.

4 Results

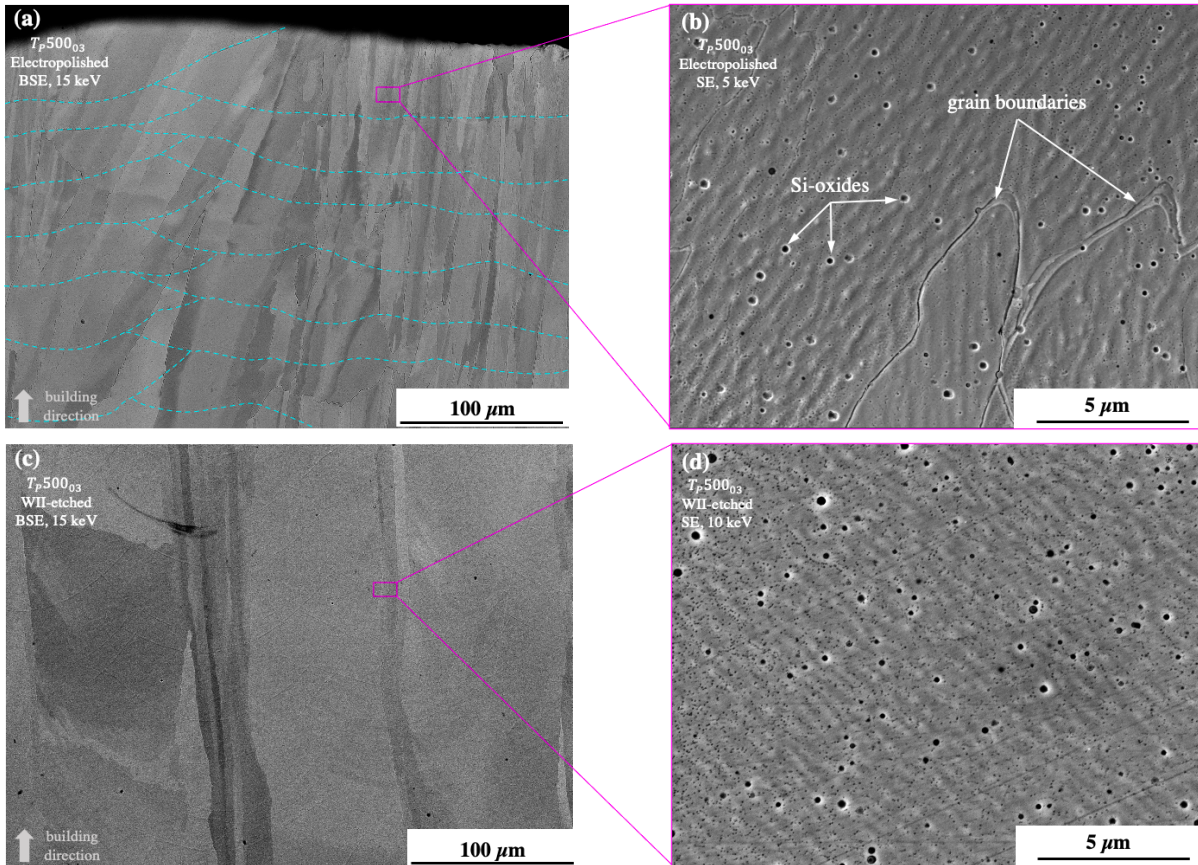


Figure 28: SEM micrographs of the $TP500_{03}$ specimen:

- (a) Top layers after electropolishing with dashed lines indicating the weld beads from LPBF (BSE-contrast).
- (b) Top layer after electropolishing (SE-contrast). The micrographs were taken in the over-etched area of the specimen due to insufficient etching attack in the masked area.
- (c) Middle section etched with 20% WII (BSE-contrast).
- (d) Middle section etched with 20% WII (SE-contrast).

Figure 29 shows the HV1 hardness of as built specimens in dependence of the distance from the top layer x of as-built specimens. The $TPnone_{500}$ specimen exhibits no significant change in hardness over the specimen height, although a slight hardness decrease can be observed with increasing x . In contrast, the $TP500_{02}$ specimen exhibits a significant hardness increase with increasing distance from the top layer.

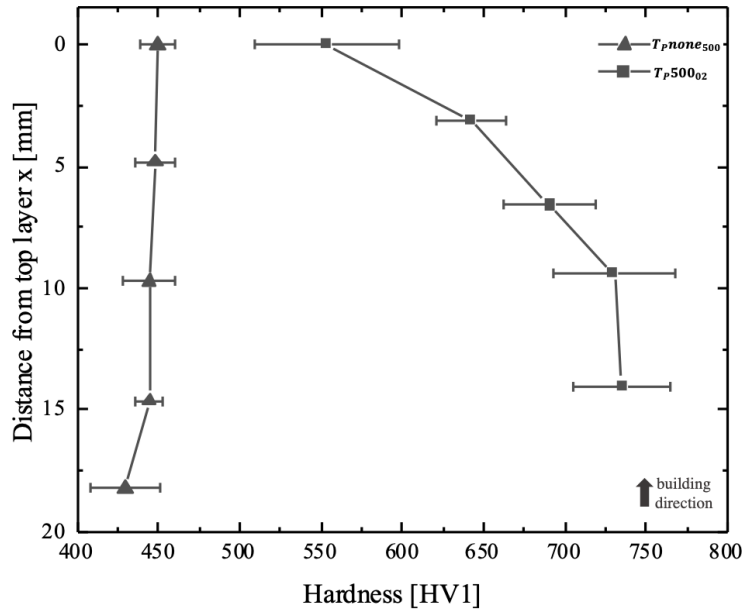


Figure 29: HV1 hardness at various distances from the top layer x of as-built specimens $TPnone_{500}$ and $TP500_{O_2}$.

4.2 APT analysis of as-built specimens

In the course of the APT measurements, Mo -rich chain-like structures were found in multiple specimens. These Mo -chains can be seen in figure 30, which shows Mo -isosurfaces in APT specimens with varying distances from the top layer, along with their respective proxigrams. Going forward, these Mo -chains will be distinguished from the parent material surrounding them. In the $TPnone_{500}$ specimen in figure 30 a, Mo -chains are present at $x = 0$ mm, $x = 2.5$ mm and $x = 5$ mm. Their Mo -content decreases with increasing x , from ~ 40 at.% at $x = 0$ mm to ~ 35 at.% at $x = 5$ mm. From $x = 2.5$ mm to $x = 9$ mm, the number and size of Mo -chains decreases. At $x = 9$ mm, no Mo -chains are visible and Mo isosurfaces with 15 at.% were chosen, because 20 at.% did not show a clear result. The Mo -content of these isosurfaces is ~ 30 at.% and varies widely. In the $TP500_{O_2}$ specimen in figure 30 b, the overall size of Mo -chains is larger than in figure 30 a. Their size and number decreases notably with increasing x . From $x = 5$ mm to $x = 8$ mm, their Mo -content decreases from ~ 45 at.% to ~ 40 at.%, but overall, there is no trend in Mo -content over x . At $x = 0$ mm, there is a Mo -rich network extending in the reconstruction. 30 at.% Mo isosurfaces were chosen to illustrate this network. The Mo -content within the isosurfaces increases to ~ 40 at.%. The Mo -rich network has a flattened shape. The compressed dimension is oriented orthogonally to the paper plane. Both Mo -chains at $x = 5$ mm also display a flattened geometry, but this does not hold true for the Mo -chain at $x = 8$ mm. At $x = 15$ mm, there are no Mo -chains present but small precipitates are visible in the parent material.

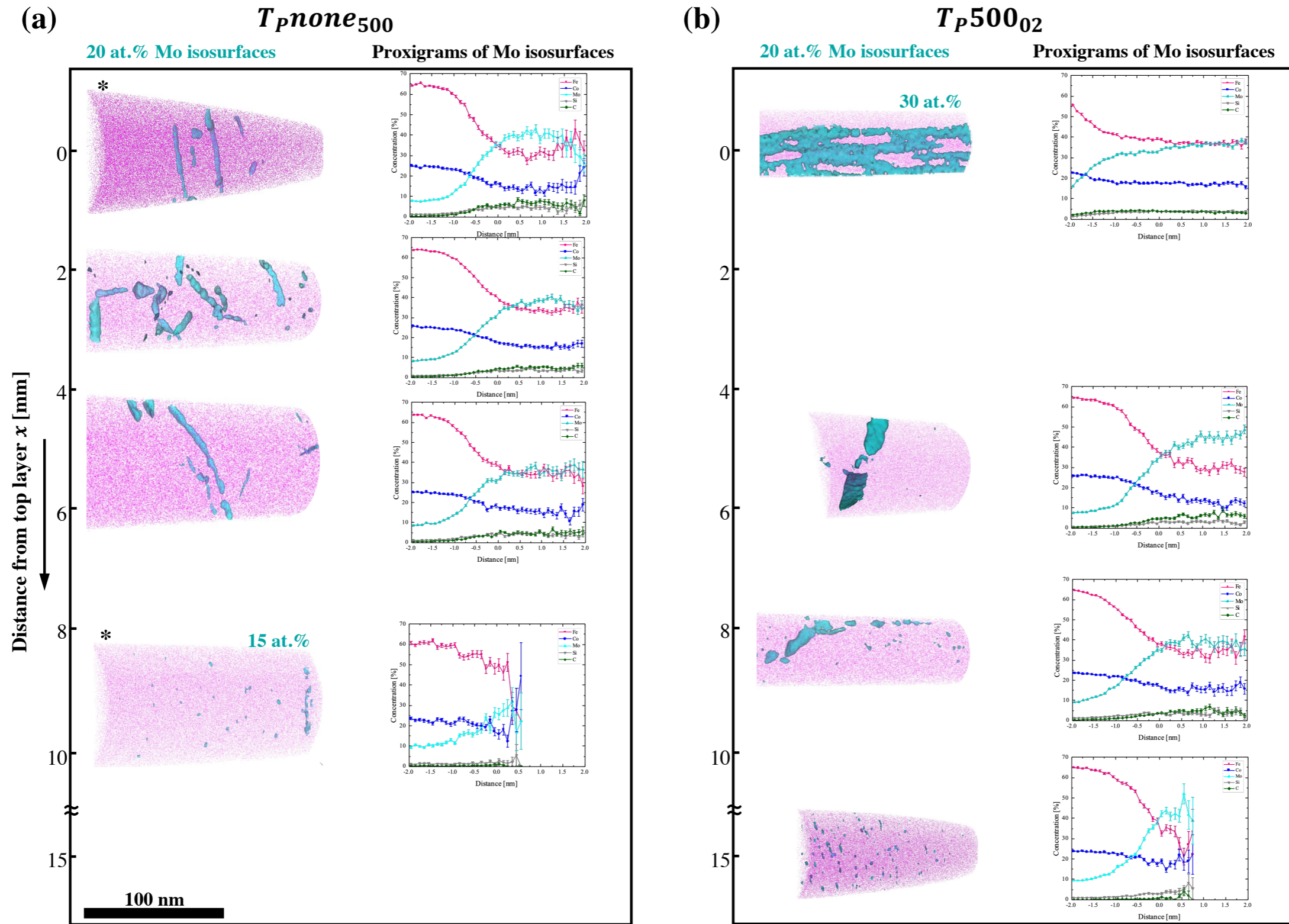


Figure 30: Evolution of solidification structure over x in the (a) $TP_{none500}$ specimen and (b) TP_{50002} specimen.

* This specimen was taken from the $TP_{none400}$ cuboid.

1st column: Mo isosurfaces.

2nd column: Proxigrams of Mo isosurfaces.

4 Results

The flattened appearance of *Mo*-chains in figures 30 a and b may not reflect reality as all of those reconstructions are voltage-based with $k_f = 3.3$. Figure 31 shows the voltage-based reconstruction with $k_f = 3.3$ (figure 31 a), the tip profile-based reconstruction (figure 31 b) and the voltage-based reconstruction with an adapted $k_f = 4.0$ (figure 31 c) of the FIB-prepared $T_{Pnone400}$ specimen at $x = 0$ mm. The tip profile-based reconstruction reveals an elongated geometry, compared to its voltage-based counterpart with $k_f = 3.3$. The initial tip radius in the tip profile-based reconstruction (8.25 nm) was only about a quarter of the initial tip radius in the voltage-based reconstruction (31.27 nm). The geometry of the *Mo*-chains in the voltage-based reconstruction was compressed by $\sim 33\%$ in longitudinal direction. Figure 31 c shows that an adjustment of $k_f = 4.0$ yielded a similar geometry of the *Mo*-chains, however the initial tip radius of 8.25 nm could not be imitated.

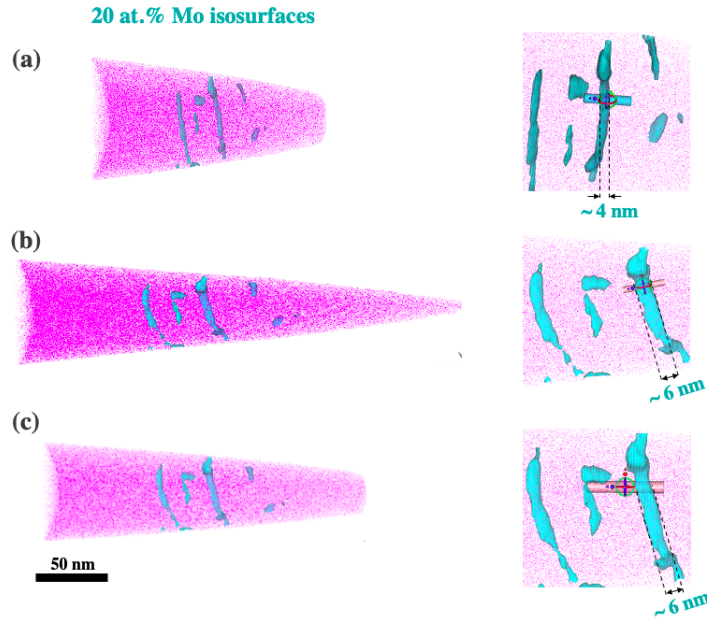


Figure 31: (a) Standard voltage-based reconstruction ($k_f = 3.3$), (b) tip profile based reconstruction and (c) voltage-based reconstruction ($k_f = 4.0$).

For the description of precipitation, matrix and precipitates will be distinguished within the parent material. The precipitation evolution in the parent material of the as-built $T_{Pnone500}$ and the as-built T_{P50002} specimen is shown in figures 32 and 33, respectively. In each of these two figures, the first column depicts the volume renderer of *Mo* isosurfaces. The second column shows the 20 at.% *Mo* isosurfaces in the specimen tips and the corresponding proxigrams are plotted in the third column. In the fourth column, the matrix composition of each tip is compared to the nominal chemical composition of the FeCoMo alloy (see table 1). Columns five and six depict the *Mo* SDMs in ZY and Z direction. In figure 33, there is an additional seventh column, in which the PSD is plotted. There is no PSD for $x = 0$ mm, as there were no precipitates in the matrix, according to the *Mo* volume renderer.

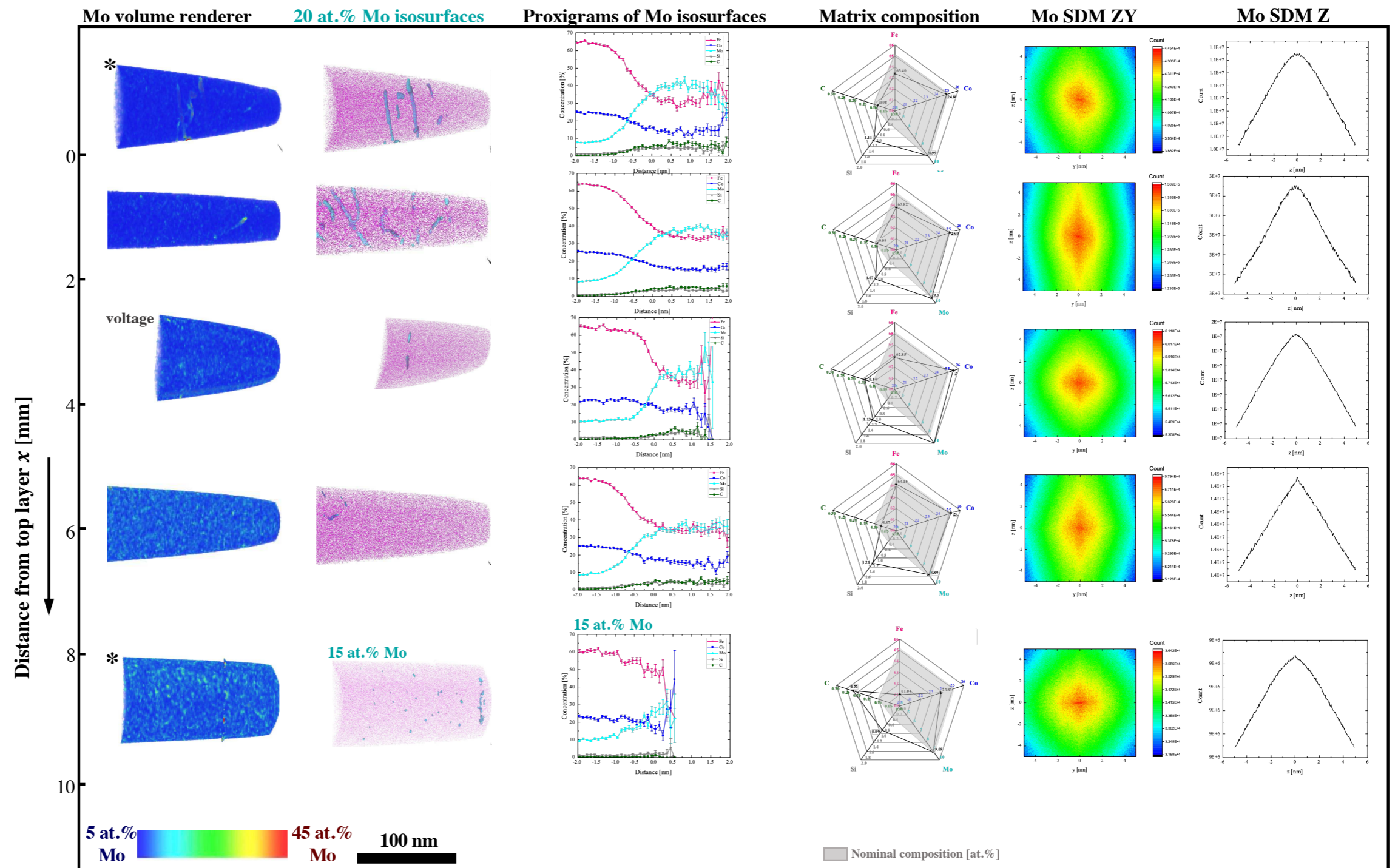


Figure 32: Evolution of precipitation over building height in the $Tpnone_{500}$ specimen.

* This specimen was taken from the $Tpnone_{400}$ cuboid.

1st column: Mo volume renderer.

2nd column: 20 at.% Mo isosurfaces.

3rd column: Proxigrams of Mo isosurfaces.

4th column: Matrix composition compared to nominal composition.

5th column: 2D Mo SDM viewed along the x -axis.

6th column: 1D Mo SDM in z -direction.

4 Results

In the $T_{Pnone500}$ specimen in figure 32, no precipitates were identified with the Mo -volume renderer. However, at $x = 1$ mm, periodic concentration fluctuations arise in the parent material and intensify with increasing x . Both amplitude and wavelength of the fluctuations increase with increasing x , whereas there were no fluctuations visible in the parent material at $x = 0$ mm. The 20 at.% Mo isosurfaces reveal Mo -chains at $x = 0$ mm, $x = 1$ mm and $x = 3$ mm. It should be mentioned at this point that the proxigrams in figure 32 are of these Mo -chains rather than precipitates. The Mo -content in the matrix at $x = 3$ mm (10.0 at.%) deviates from that of the other matrices (~ 9 at.%). Note that this was the result from the voltage measurement. In all specimens, the Si -content in the matrix is higher than the nominal 0.4 at.%. Similarly, the C -content appears to be elevated in all specimens, except $x = 6$ mm. However, the content of impurity elements may be overestimated, see section 2.4.6. All in all, no trend could be made out regarding the matrix composition depending on x . Likewise, the Mo SDMs exhibit no dependency on x .

In contrast, the appearances of the specimens from T_P500_{03} in figure 33 evolve in dependence of x . The Mo volume renderer already reveals periodic concentration fluctuations at $x = 2$ mm. Small precipitates, dispersed homogeneously in the matrix, can be seen with 20 at.% Mo isosurfaces. They comprise of ~ 40 at.% Mo , ~ 33 at.% Fe and ~ 18 at.% Co . Small amounts of Si and C also aggregate within them. The PSD reveals a peak number of 5 precipitates with $R = 1$ nm. PSDs show that the precipitates grow in number and size with increasing x . At $x = 4$ mm, there are 17 precipitates with $R = 1$ nm and at $x = 7.5$ mm, there are 35. The maximum R of the precipitates also increases from 1.5 nm at $x = 2$ mm to 5.5 nm at $x = 7.5$ mm. Moreover, the Mo -content of the precipitates increases to ~ 42 at.% Mo at $x = 4$ mm and ~ 46 at.% Mo at $x = 7.5$ mm. At $x = 7.5$ mm, the matrix is notably depleted of Mo (8.26 at.%) and Si (0.79 at.%) and enriched with Co (25.56 at.%), compared to $x < 7.5$ mm. The Mo SDMs from $x = 0$ mm to $x = 7.5$ mm show increased localisation of Mo and its molecular ions, i.e. an accumulation of Mo at smaller distances, as the interatomic positions vectors of Mo become smaller with increasing x , up to $x = 7.5$ mm. An exception from these trends is the specimen at $x = 15$ mm, i.e. in close proximity to the platform. It contains fewer and smaller precipitates. Their maximum size is $R = 2.0$ nm and their Mo -content ~ 44 at.%. The Mo -content in the matrix (8.48 at.%) is somewhat below the nominal composition and the Mo SDMs are less localised than at $x = 7.5$ mm and $x = 4$ mm.

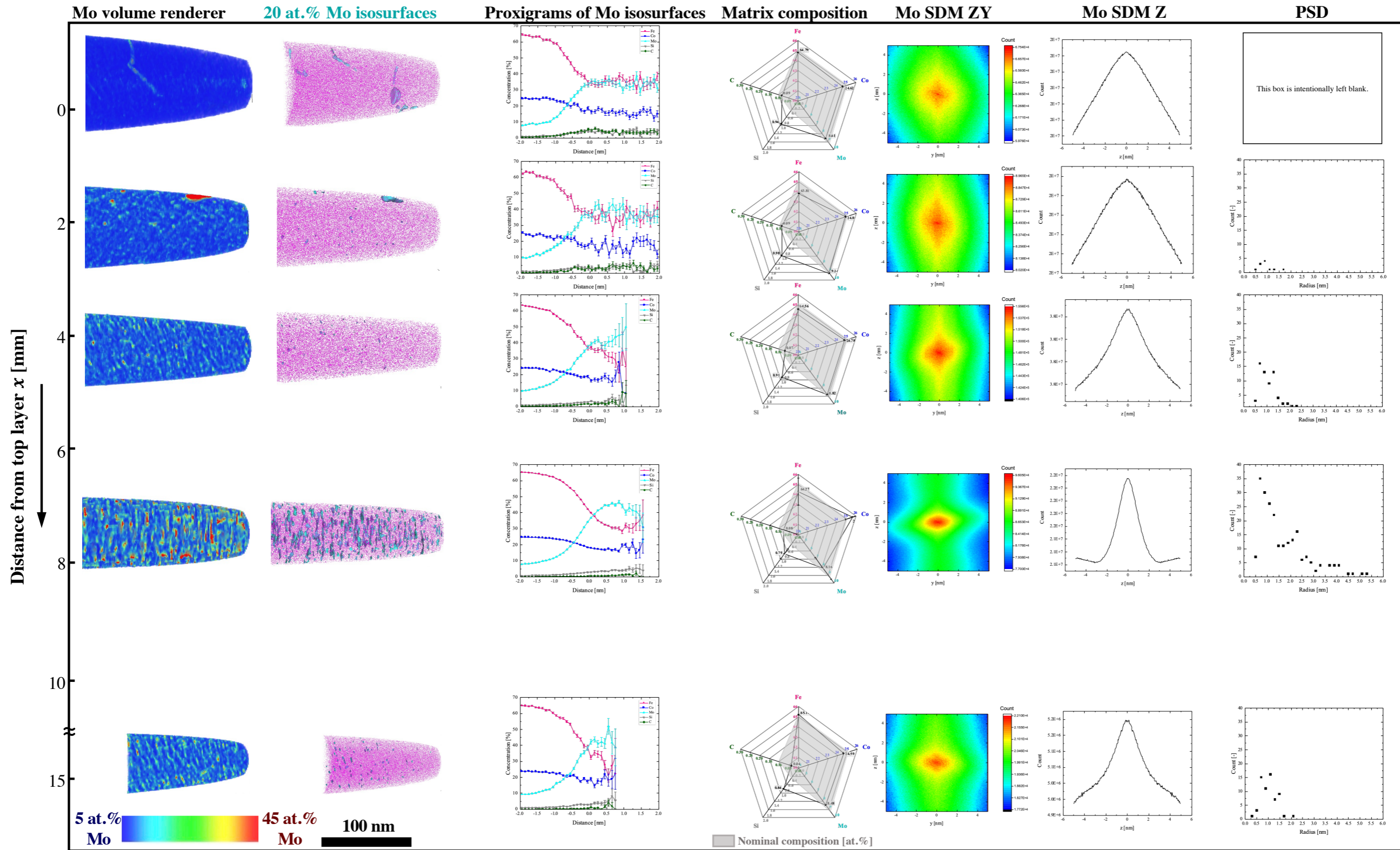


Figure 33: Evolution of precipitation over building height in the $Tp500_{O_2}$ specimen.
 1st column: Mo volume renderer.
 2nd column: 20 at.% Mo isosurfaces.
 3rd column: Proxigrams of Mo isosurfaces.
 4th column: Matrix composition compared to nominal composition.
 5th column: 2D Mo SDM viewed along the x -axis.
 6th column: 1D Mo SDM in z -direction.
 7th column: PSD of a $60 \times 60 \times 150 \text{ nm}^3$ volume in the APT reconstruction.

4 Results

After an adjustment of k_f in the voltage-based measurement to imitate the tip profile-based reconstruction and hence more closely relate to reality, most of the precipitates in the $TP500_{02}$ specimen at $x = 7.5$ mm retain their flattened, rod-shaped appearance, see figures 34 a and b. Some smaller precipitates attain a spherical shape.

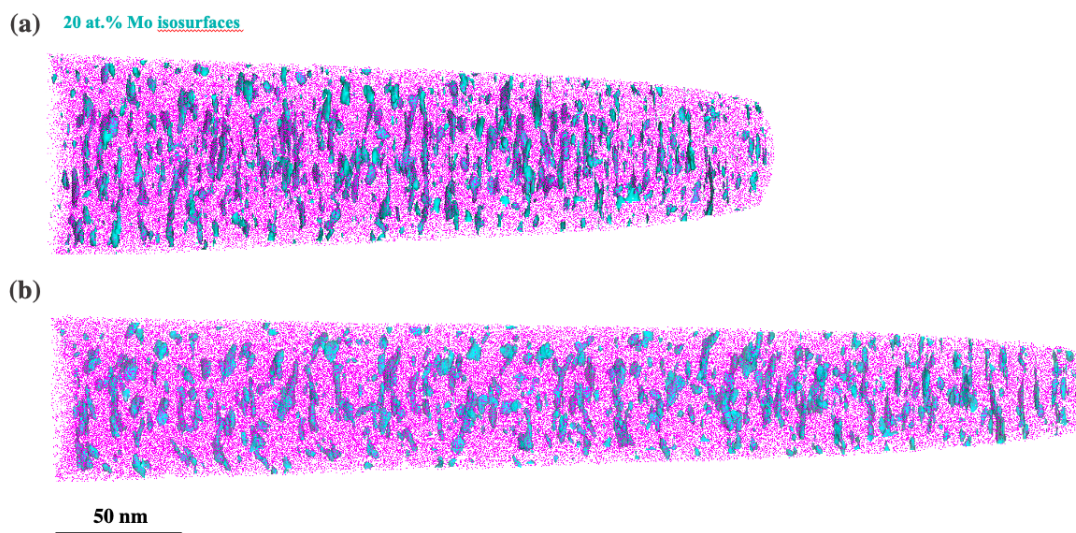


Figure 34: Precipitates in the $TP500_{02}$ specimen at $x = 7.5$ mm for (a) $k_f = 3.3$ and (b) $k_f = 4.0$.

Figure 44 in the appendix shows the results from the maximum separation algorithm for Mo , Si and C . Unfortunately, the algorithm did not yield a conclusive result. Regarding Mo -clusters, the algorithm only identified clusters near the tip apex, which disagrees with the Mo -isosurfaces. The algorithm did find Si and C clusters within the tip volume, however their size, shape and location was not in agreement with the respective isosurfaces.

During electrolytic preparation, it is impossible to know which microstructural features are present in the specimen tip. Due to the hierarchical and highly inhomogeneous micro- and nanostructure of LPBF material (weld beads, heat-affected zones, dendrites, segregations, etc.), the incidental measurement of contaminations is inevitable. In one specimen, sub-nm-sized Si -oxides were found. Figure 35 a shows those Si -oxides. The decomposed 7 at.% SiO isosurfaces in the $TPnone_{500}$ specimen at $x \approx 0.6$ mm are shown. In the voltage-based reconstruction with $k_f = 3.3$ in figure 35 a, there are smaller particles with diameters of ~ 0.03 nm and one bigger, flattened particle with a mean diameter of ~ 0.05 nm. Figure 35 b shows that after an adjustment of $k_f = 4$, the oxides attain a spherical shape. The proxigram belonging to the isosurfaces is depicted in figure 35 c. The specimen tip includes Si -oxides with 43 at.% Si and 40 at.% O .

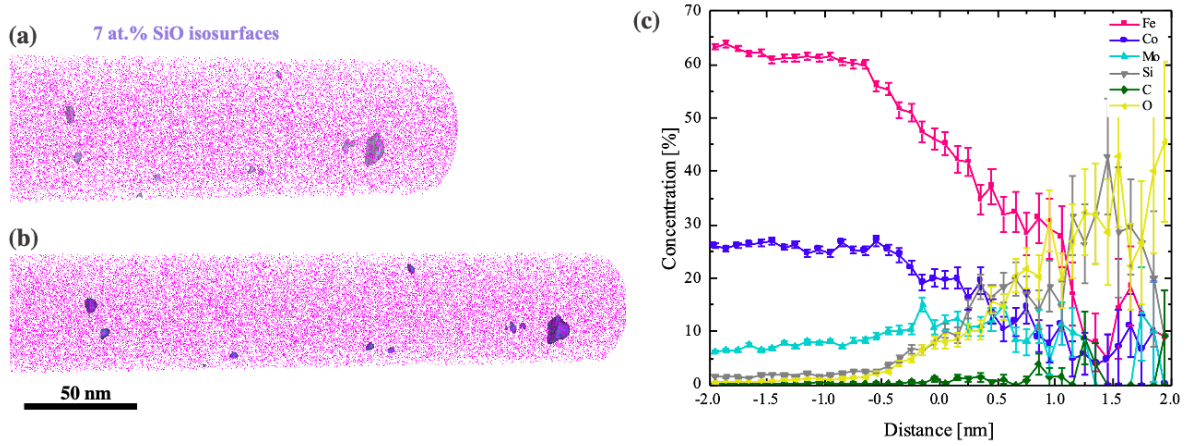


Figure 35: (a) Voltage-based reconstruction of the $T_{Pnone500}$ specimen at $x \approx 0.6$ mm with $k_f = 3.3$. Decomposed 7 at.% SiO isosurfaces are shown.
 (b) Voltage-based reconstruction with $k_f = 4.0$.
 (c) Proxigram over all 7 at.% SiO isosurfaces.

4.3 Comparison of precipitation behaviour using dilatometry

The resulting relative length change–temperature curves of the dilatometer measurements are shown in figure 36 a. During heating, the only phase transformation taking place is austenitisation. The high austenitisation temperature ($A_s \approx 930$ °C, $A_f \approx 960$ °C) is an indicator for the high thermal stability of the FeCoMo alloy (cf. section 2.2.2). The dashed blue circle in figure 36 marks a fluctuation in length attributed to turning off the Ar gas after rapidly quenching from 1180 °C to 500 °C. Because rapid quenching is required to imitate the cooling conditions during LPBF, Ar gas flows into the chamber with high flow rates. In order to prevent the sample from under-cooling, the high-frequency coil readjusts the temperature, according to the measured temperature from the thermocouple. When the cooling gas is turned off, the coil does not immediately react, but overheats before re-adjusting. The resulting fluctuation is negligible for the purpose of the measurement, because of the absence of phase transformations in its vicinity. Figure 36 b is a more detailed depiction of M_s .

4 Results

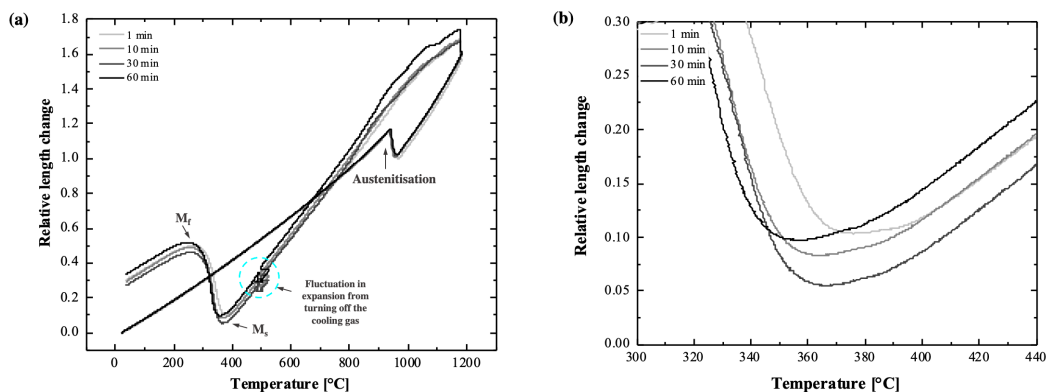


Figure 36: (a) Relative length change during the dilatometer measurements of varying dwell time at 500 °C.
 (b) Detail of M_s .

The variation in dwell time at 500 °C results in a slight change in M_s and M_f , see table 5. The hardness values resulting from the varying dwell times are also given in table 5. No significant change in hardness is observed for the varying dwell times.

Table 5: M_s and M_f for varying dwell times at 500 °C from dilatometer measurements and resulting hardness.

Dwell time at 500 °C [min]	M_s [°C]	M_f [°C]	Hardness [HV]	St. dev. [HV]
1	380	260	458	1.6
10	360	240	459	0.8
30	360	240	458	1.4
60	350	220	458	1.7

5 Discussion

In this section, the SEM micrographs of the LPBF-processed FeCoMo alloy will be discussed, the previously presented results from APT measurements will be interpreted and the nanostructural features of the FeCoMo alloy will be correlated to the results from the hardness measurements. On a microstructural scale, the SEM micrographs in figures 27 a, c and figures 28 a, c reveal elongated grains, which are oriented along the building direction. Moreover, the partial remelting during LPBF caused grains to expand over multiple layers. This epitaxial growth of existing grains into the subsequent layer is visible in figure 27 d. Directional solidification and pronounced epitaxial growth are the result of strong thermal gradients during LPBF (cf. section 2.3.2) and reportedly attributed to high laser powers [57].

The SEM-SE micrographs with higher magnification in figures 27 b, d and figures 28 b, d reveal fine structures within the grains. These structures appear slightly brighter than the matrix in the SEM-BSE micrographs in figures 42 b and 43 b, which indicates *Mo*-enrichment within the structures. The size of these structures should be viewed with caution, due to the limited spatial resolution in SEM. The volume of interaction of an electron beam with the material depends on its atomic number and the acceleration voltage of the electron beam. Accordingly, the interaction volume limits the spatial resolution in SEM [58]. As increasing voltage is necessary to excite heavier elements (e.g. *Mo*), the interaction volume also increases. Despite the limited spatial resolution of the fine structures in SEM, their separation distance is in the same order as between the *Mo*-rich chains in the APT analysis in figure 30. In literature, *Mo*-rich chains have been found in *Fe-Mo* alloys, as well as in the investigated FeCoMo alloy after ageing. In their investigation of an *Fe-20 Mo* (at.%) binary alloy after ageing for 20 h at 500 °C, Isheim *et al.* [59] found chain-like *Mo*-rich precipitates ($\varnothing \sim 5$ nm). These precipitates consisted of ~ 90 at.% *Mo*. After ageing for that long, the alloy is considered to be overaged, hence approaching its equilibrium state. The elongated shape of those precipitates was justified with the elastic anisotropy of *Fe*. *Mo* preferably precipitates along the $\langle 100 \rangle$ type directions of the *Fe*-rich bcc matrix, as those are the elastically softest directions and thereby the coherency strain energy caused by the pronounced difference of the atomic radii of *Fe* and *Mo* is minimised. Eidenberger *et al.* [60] studied the spinodal decomposition of a HIP *Fe-25 Co-9 Mo* (at.%) alloy during ageing after solution annealing. This was the same alloy as investigated in this thesis but processed through the conventional manufacturing route. They also found chain-like μ -phase precipitates (~ 42 at.% *Mo*) in later ageing stages (600 °C for 3000 s). However, they could not unambiguously determine whether the precipitate-shape was caused by spinodal decomposition or coherency strains.

As the T_{Pnone} specimen is not overaged but also exhibits chain-like *Mo*-rich domains, a different approach for the explanation of their origin is attempted. These *Mo*-chains did not exhibit a uniform chemical composition. Their decrease in *Mo*-content with increasing x in the $T_{Pnone500}$ specimen (see figure 30 a) could indicate their dissolution with an increasing number of IHT-cycles. Their decrease in number and size in the T_{P50002} specimen with x in figure 30 b

supports this theory. Hence, the observed *Mo*-chains in the APT reconstructions are considered to be interdendritic segregations of *Mo* and impurity elements (*Si* and *C*) from the melt. Hagh-dadi *et al.* [57] reported that AM solidification cells are subgrains with very similar orientation, outlined by segregations of alloying elements and dislocation accumulations at their boundaries. As previous investigations of LPBF *Ni*-maraging steels [33, 39–41] found dendritic solidification structures with *Ni*-segregations in interdendritic spaces, the structures depicted in figures 27 and 28 are most likely the result of segregation during dendritic solidification. As *Mo* is likely to segregate from the *Fe*-rich melt, *Mo*-agglomerations in interdendritic spaces are a valid point of discussion. The generally broader shape of the *Mo*-chains in the $TP500_{02}$ specimen could stem from the effect of platform preheating, resulting in a slower cooling rate and hence a more pronounced *Mo*-segregation.

As the top layer experiences no reheating, it reveals the solidification structure of the material. When lower layers experience IHT, *Mo*-segregations may be dissolved into the matrix. The dissolution of interdendritic segregations could be confirmed by the slight decrease in hardness with x in the $TPnone$ specimen, see figure 29. Bajaj *et al.* [61] argue that the hierarchical microstructure in AM material is one reason for its higher hardness compared to conventionally manufactured material, which is visible in figure 25. Dendrites and subgrains resist against sub-surface deformation by hindering dislocation movement [57].

During laser-mode APT, the tip apex may experience a significant increase in temperature, as figure 10 shows. In trying to adjust k_f to the real temperature during the measurement, $k_f = 4.0$ yielded a promising reconstruction, similar to the tip profile-based reconstruction in figure 31, regarding the geometry of the *Mo*-chains. The longitudinal compression in the voltage-based reconstruction with $k_f = 3.3$ was caused by the thermal evaporation of ions during laser-mode APT. The evaporation field values for ionic species in the IVAS database were default values for 33 K. The evaporation field of a species decreases with increasing temperature. Accordingly, its evaporation field could actually be significantly lower during laser pulsing than the database suggests. As a result, $k_f = 3.3$ may not be accurate for these measurements (cf. equation 3). One might argue that the tip profile-based reconstruction is the most accurate way to visualise the real shape of nanostructural features within the APT tip, however, the danger of this method is that the SEM image only depicts a 2D projection of the tip. If the tip is not rotationally symmetric, the reconstruction yields an incorrect geometry, as there is no underlying physical quantity that the reconstruction is based on, in contrast to the voltage-based reconstruction. However, the adjustment of $k_f = 4.0$ was useful for the depiction of the geometry of the precipitates, which were found in the $TP500$ specimen in figure 34.

Since precipitation during LPBF was especially of interest, it will be discussed in the following. As could be seen in figure 25, a significant hardness increase of both as-built LPBF conditions occurred upon ageing, which is a clear indication for a *Mo*-supersaturated matrix in the as-built condition. Accordingly, μ -phases precipitate from the supersaturated matrix during ageing, which are responsible for the hardness increase. Furthermore, there are no visible primary μ -phase precipitates in the SEM micrographs of both as-built specimens in figures 27 and 28, which

is also a sign for supersaturation. However, the resolution of SEM is not sufficient to visualise early stages of μ -phase precipitation.

It is known that the first stage of precipitation in a FeCoMo alloy is related to spinodal decomposition. Incidentally, the inherent heating and cooling cycles in LPBF are useful for the study of spinodal decomposition and precipitation behaviour in the investigated FeCoMo alloy. Moreover, the layer-wise build-up yields multiple conditions, from various stages in spinodal decomposition to particle growth. Accordingly, the significant hardness increase with increasing x in the T_P500_{03} specimen in figure 29 points towards precipitation in bottom layers. It is assumed that the effect of IHT increases with the number of thermal cycles from the weld passes during LPBF. Therefore, ageing effects are typically more pronounced in bottom layers of LPBF parts. Additionally, if platform preheating is applied, bottom layers are exposed for a longer time and may experience temperatures closer to the nominal T_P than top layers due to limited heat conduction to areas farther away from the platform.

The T_Pnone specimen in figure 32 exhibited a homogeneous parent material at $x = 0$ mm with no concentration fluctuations of Mo in the matrix between the Mo segregations. Moving away from the top layer, periodic Mo -concentration fluctuations arose in the parent material and became more pronounced with increasing x , which is depicted by the volume renderer in figure 32. These Mo -concentration fluctuations are likely to be early stages of spinodal decomposition (cf. section 2.2.2) [60]. The increasing amplitude of these periodic fluctuations with x in the T_Pnone specimen could indicate advancing stages of spinodal decomposition, as Cahn [12] predicted an increase in wavelength and amplitude with further progression of decomposition. Both the absence of concentration fluctuations at $x = 0$ mm and the decomposition with additional energy input from thermal cycling encourage the assumption of a supersaturated parent material after one rapid heating and cooling cycle. Although the deposition of subsequent layers triggered spinodal decomposition, the driving force in the T_Pnone specimen did not suffice for the formation of precipitates that were unequivocally distinguishable from the matrix in the Mo -isosurface depiction in figure 32. This may be attributed to insufficient amplitudes of the Mo -concentration fluctuations.

When $T_P = 500$ °C was applied, however, various stages of precipitation were observed within the T_P500_{02} specimen, see figure 33. While the top layer ($x = 0$ mm) exhibited supersaturated parent material with no noteworthy Mo -concentration fluctuation in the Mo volume renderer, the onset of spinodal decomposition can already be made out at $x = 2$ mm. The wavelength and amplitude of this fluctuation are already larger than in each of the T_Pnone reconstructions, which indicates a later stage of spinodal decomposition [12, 13]. At $x = 4$ mm, the increased amplitude of the Mo -concentration fluctuation yields small precipitates ($R \approx 1$ nm) with ~ 41 at.% Mo , which are represented by 20 at.% Mo isosurfaces in figure 33. The degree of precipitation is additionally represented by Mo -SDMs. Both ZY- and Z-SDMs show the increasing localisation of Mo -ions with smaller inter-atomic distances with increasing x , i.e. progressing precipitation. As precipitation advances, the Mo -content in the matrix decreases, because a larger amount of Mo is needed to form μ -phase precipitates. At $x = 7.5$ mm, the composition of the precipitates

5 Discussion

reaches the nominal chemical composition of the μ -phase $(Fe, Co)_7Mo_6$ ($\cong 46$ at.% Mo) [22]. The small deviation in chemical composition of the precipitates, compared to the precipitates at $x < 7.5$ mm, could indicate a composition near the equilibrium of the μ -phase. The significant increase in number density and size also point towards later stages in decomposition and early stages of particle growth. Therefore, these precipitates at $x = 7.5$ mm are considered to be μ -phase precipitates that have already undergone the beginnings of particle growth. Impurity elements such as Si (4 at.%) and C (1 at.%) are preferably enriched within the precipitates. This was previously observed by Leitner *et al.* [56] in APT studies regarding the precipitation behaviour of solution annealed conventionally manufactured material during ageing. It should be addressed at this point that, while the reconstructed specimen tips at the respective positions in figures 30, 32 and 33 are prepared from the same specimen blank, they do not stem from the same APT measurement. Due to the wildly inhomogeneous melting, solidification and remelting conditions during LPBF, the appearance of the tips, even from the same specimen blank, varies, as contaminations accumulate near the weld bead boundaries, as is shown schematically in figure 37. Additionally, IHT conditions have may been different in adjacent parts of the specimen blank, resulting in various appearances in the reconstruction, as only a small volume is viewed with APT.

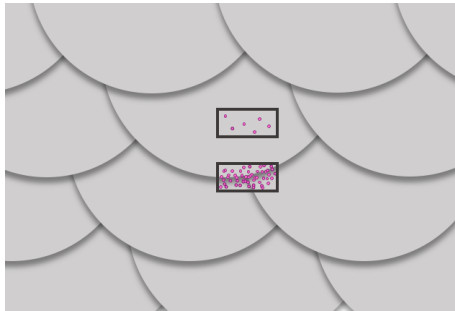


Figure 37: The inhomogeneous melting, solidification and remelting conditions during LPBF result in different nanostructures within the same specimen blank.

In figure 33 at $x = 7.5$ mm in the T_P500 specimen, the 20 at.% Mo isosurfaces visualised μ -phase precipitates with 46 at.% Mo . A closer look at the precipitates in figure 34 a revealed a flattened, rod-shaped geometry in the reconstruction using $k_f = 3.3$. In the following, the flattened shape of the precipitates in the APT reconstruction will be discussed and whether an adjustment of k_f yields a more truthful geometry will be argued. Stergar [62] observed a cube-like network in Fe-25Co-15Mo alloys with additions of 4 wt.% Cr, 1 wt.% Nb, 2 wt.% Nb, 2 wt.% V and 4 wt.% V, respectively, using voltage-mode APT. With further ageing, the precipitates grew and coarsened but kept a flat appearance and remained interconnected. It should be noted, however, that Mo has a higher evaporation field (Mo^{2+} 41 V/nm) than Fe^{2+} (33 V/nm) and Co^{2+} (37 V/nm). As a result, Mo -rich precipitates experience a higher lateral magnification in APT, which causes lateral distortion of the precipitate shape [43]. Additionally,

5 Discussion

the comparison with the tip profile-based reconstruction in figure 31 suggested a geometrical longitudinal compression of the voltage-based reconstruction. However, after the adjustment of $k_f = 4.0$, larger precipitates at $x = 7.5$ mm still retained their flattened shape while smaller ones attained a spherical shape. Cahn predicted in multiple publications [12, 13, 16] that the mechanisms of spinodal decomposition and subsequent particle coarsening in cubic crystals are first activated in the $\langle 100 \rangle$ directions. In later stages, other orientations are activated as well, however, they are slower-growing than the $\langle 100 \rangle$ orientations. This preference in orientation is explained through the elastic anisotropy in cubic crystals, where the $\langle 100 \rangle$ directions are the elastically softest directions. Hence, it is favourable for solutes and precipitates to align in these directions. Because of the preferred spinodal decomposition in those crystallographic directions, precipitates are first formed the same directions. The flattened, rod-shaped geometry of larger precipitates could be the result of this directional preference of precipitate growth. Moreover, coherent stresses between precipitate and matrix increase with increasing precipitate volume. For larger precipitates, it could be therefore more convenient to form a flattened, rod-shaped geometry in the elastically softer $\langle 100 \rangle$ directions. For smaller precipitates, surface energy minimisation may be more effective than the minimisation of coherency energy. Hence, small precipitates may display a spherical geometry.

In the T_P500 specimen, an exception regarding the above-mentioned trends in precipitation was found at $x \approx 15$ mm (i.e. near the platform). There were no prominent precipitates and the SDMs showed a less pronounced localisation of Mo . An attempt was made to imitate the precipitation behaviour during LPBF with $T_P = 500$ °C using dilatometer measurements of conventionally produced material. Holding HIP material at 500 °C for various dwell times resulted in no difference in hardness (458 HV), which is shown in table 5. As $M_s < 500$ °C, it can be assumed that no μ -phase precipitates from the austenite phase in conventionally produced material. The slight shift of M_s to lower temperatures with increasing dwell time (see figure 36 b and table 5) may be due to alloying elements diffusing towards primary μ -phase particles. However, the conditions during LPBF could not be recreated with dilatometry. The specimens could not be rapidly solidified from the melt and the IHT-cycles were disregarded. Nevertheless, the dilatometer measurements could explain the decrease in precipitate density, size and Mo -localisation at $x \approx 15$ mm compared to $x = 7.5$ mm. The precipitation of μ -phase may have been suppressed in the T_P500_{02} specimen near the platform with a nominal $T_P = 500$ °C. However, Huber *et al.* [63], who studied microstructure and hardness after LPBF of a AISI H11 hot work tool steel with platform preheating with a SLM 280^{H1}, found that the nominal T_P was not reached on the platform surface. Instead of the nominal $T_P = 500$ °C, they only measured 381 ± 8 °C at the platform surface. If the nominal T_P was not reached at the platform surface during LPBF of the investigated FeCoMo alloy, it could explain the high hardness (730 ± 40 HV) at $x = 15$ mm. If $M_f < T < M_S$ at $x = 15$ mm, the microstructure would be partially austenitic and partially martensitic. Precipitation could occur in the martensite phase where a large number of dislocations act as nuclei, resulting in a hardness increase. In the austenite phase, however, precipitation would be suppressed, which could lead to the small number density and

5 Discussion

size of precipitates that was observed in figure 33. Despite the small size and number of precipitates at $x = 15$ mm in the T_P500 specimen compared to $x = 7.5$ mm, its hardness does not decrease. It is assumed that the small precipitates at $x = 15$ mm are more effective than the larger ones at $x = 7.5$ mm, regarding their hardening effect. The relation between shear stress, and consequently hardness, and precipitate size is shown in figure 38. When a critical radius R_{crit} is reached, further increasing precipitate size results in a hardness decrease, as the mechanism for dislocation interaction changes from cutting to circumventing [64]. Hence, it is assumed that the radius of the precipitates at $x = 15$ mm in the T_P500 specimen is smaller than R_{crit} , while the precipitates at $x = 7.5$ mm are larger than R_{crit} , resulting in similar hardness at both positions.

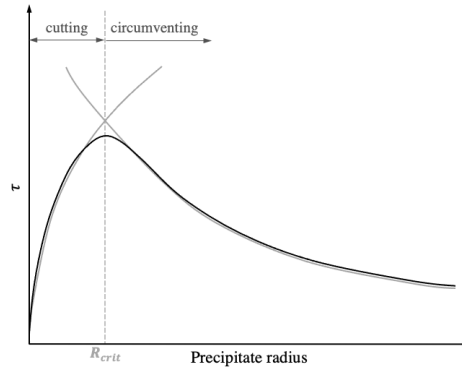


Figure 38: Dependency of shear stress for cutting and circumventing precipitates by dislocations from precipitate size (cf. [64]).

With increasing distance from the platform, limited heat conduction of fused material may have prevented the attainment of T_P and precipitates were able to form in an increasingly martensitic microstructure. Moreover, the loose metal powder surrounding the fused part may also have a cooling effect, as it has significantly lower heat conduction properties than the fused material [65]. As a consequence, the temperature T_N that the N-th layer experienced at some distance from the platform may have dropped below M_s , or even below M_f , and μ -phase may have precipitated from the martensite phase. Moreover, the rapid solidification from the melt during LPBF could not be imitated during the dilatometer measurements. Hence, there could have been an increase in M_s when the material solidified from the melt in LPBF, which would have allowed precipitation at higher temperatures. However, the dwell time at T_N during LPBF decreases with increasing distance from the platform and there may not have been enough time for the formation of precipitates. Also, there may have been a critical distance from the platform, where T_N is not high enough to provide the necessary driving force for precipitation. This could result in a similar nanostructure as in the T_Pnone specimen. This temperature gradient during LPBF with $T_P = 500$ °C is schematically shown in figure 39.

5 Discussion

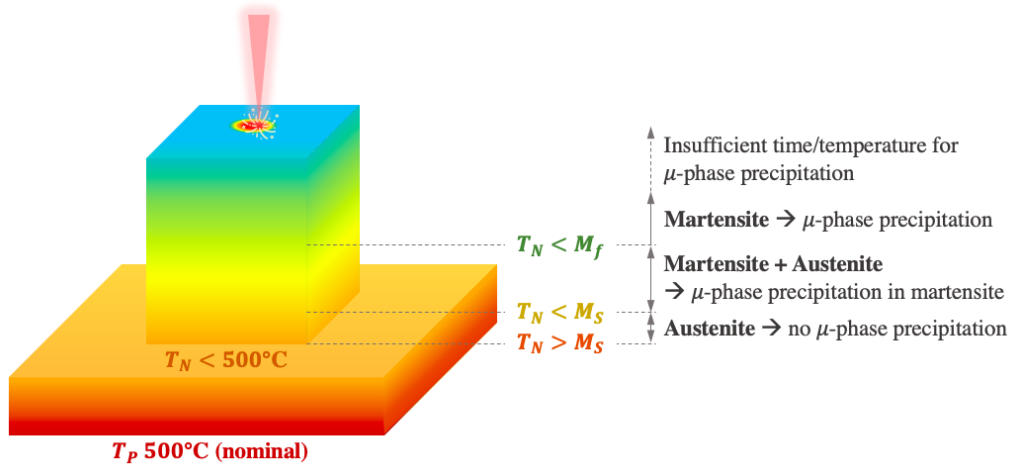


Figure 39: Schematic depiction of the temperature gradient in the building platform according to Huber *et al.* [63] and the temperature gradient in the fused part due to imperfect heat conduction, along with the microstructures in the part during LPBF.

The effect of the various stages of spinodal decomposition and precipitation in the as-built specimens will now be correlated to their ageing responses and their hardness will be compared to the heat-treated HIP material. The onset of spinodal decomposition in the T_{Pnone} specimen (see figure 32) and the presence of various stages of precipitation in the T_{P500}_{03} specimen (see figure 33) may be one reason for the inferior ageing response of both as-built specimens compared to conventional material, which is shown in figure 25. The parameters for the ageing treatment have been optimised for conventional SA material. As IHT during LPBF has triggered spinodal decomposition in the T_{Pnone} specimen, the ageing treatment may result in a slightly overaged state. Overaging could be even more pronounced in the T_{P500} specimen where precipitates are already present in the as-built condition. This is mirrored in its hardness, which is even lower than that of the aged T_{Pnone} specimen, as can be seen in figure 25. Of course, the defect structure resulting from LPBF may also contribute to the inferior hardness, but the superior hardness of SA+aged LPBF specimens in figure 25 disproves a significant impact of defects on the measurement. The slightly higher hardness of SA+aged LPBF specimens could be a result of the absence of coarse primary μ -phase particles. Accordingly, more Mo may be in solution after SA and a higher density of fine μ -phase particles could precipitate during ageing. These fine precipitates are more effective for strengthening, see figure 3. However, without primary μ -phase particles to hinder grain boundary movement during SA, grain coarsening is likely to take place.

The existence of μ -phase and its preliminary stages in the T_{P500}_{03} sample is not only accounted for by the hardness increase with x (see figure 29) but it is also in agreement with the results from the preceding DSC-measurements in section 1, which suggested the presence of Mo -rich domains in the AM500 sample [8]. Precipitation leads to an increase in hardness, which could

5 Discussion

promote embrittlement and cracking during LPBF. This is supported by the increasing number density in the T_{P50002} specimen with increasing x in figure 16 b.

As it is impossible to select the ROI during electrolytic preparation, impurities were incidentally found in the course of the APT measurements. Figure 35 proves the presence of nm-sized *Si*-oxides in the T_{Pnone} specimen. *Si*-oxides may have formed due to oxidation of *Si* in the melt during powder atomisation or during LPBF. The high-magnification SEM micrographs of as-built specimens in figures 27 b, d and figures 28 b, d revealed a quantity of *Si*-oxides (dark dots) embedded in the matrix. However, the APT analysis in figure 35 showed that their chemical composition was not in accordance with SiO_2 , as there was not twice as much *O* as *Si*. During APT, the bonds between *Si* and *O* may have been broken. Both elemental and molecular ions may have arrived at the detector, if not both *Si* – *O* bonds were broken. In detail D of the APT mass spectrum in figure 20, there is a SiO^{1+} -peak at ~ 44 Da. This could be an indication for a partial breakup of SiO_2 during APT. The separated *O*-ion could have been lost in the background noise or due to the insufficient detection efficiency of the LEAP ($\sim 37\%$ [43]), resulting in chemically imperfect *Si*-oxides in the reconstruction. The shape of the *Si*-oxides appeared flattened in the reconstruction in figure 35 a. However, after the adjustment of $k_f = 4.0$ to account for the temperature increase during laser-APT, they attained a spherical shape (figure 35 b), which is more likely to reflect reality due to surface energy minimisation. The presence of dispersed *Si*-oxides could contribute to embrittlement of the material and ultimately to cracking during LPBF. The effect of these *Si*-oxides on the cracking behaviour of the FeCoMo alloy during LPBF remains to be studied.

6 Conclusions

The causes for cracking of the investigated FeCoMo alloy during LPBF may be embrittlement due to the presence of brittle ordering phase, *Si*-oxides, precipitates and/or coarse grains. Previous DSC measurements (see section 1) proved the absence of ordering phase in as-built specimens. However, they suggested the presence of *Mo*-rich domains or preliminary stages of precipitates. In this thesis, the precipitation behaviour of the FeCoMo alloy during LPBF was studied with APT and linked to the hardness of as-built specimens and their hardening response during ageing. Two as-built conditions were examined: T_{Pnone} with no platform preheating and T_{P500} with a preheating temperature of 500 °C. The following conclusions can be drawn:

- *Mo* and impurity elements segregated to interdendritic spaces during LPBF and formed *Mo*-rich chain-like structures in the APT reconstruction, which were also visible in the high-magnification SEM micrographs. In the T_{P500} specimen, the *Mo*-chains were generally broader than in the T_{Pnone} specimen due to less steep thermal gradients. These segregations dissolved during IHT. Their density, size and *Mo*-content decreased with increasing x . The dissolution of these segregations could have been the reason for the slight decrease in hardness with increasing x in the T_{Pnone} specimen.
- In the T_{Pnone} specimen, no μ -phase precipitation occurred during LPBF. In the as-built condition, the matrix was super-saturated with *Mo*, despite small concentration fluctuations indicating early-stage spinodal decomposition. Hence, the directly aged specimen was slightly overaged and exhibited a lower hardness than the fully heat treated HIP material.
- The increasing hardness in the as-built T_{P500} specimen with x was the result of precipitation in bottom layers. Various stages of precipitation were observed at different x . μ -phase precipitates were homogeneously dispersed in the matrix at $x = 7.5$ mm. The presence of μ -phase precipitates and its preliminary stages was in agreement with preceding DSC measurements and it was also responsible for the inferior hardness of the directly aged specimen, compared to the fully heat treated HIP material due to overaging.
- The dilatometer measurements showed that no precipitation occurred from the austenite phase in conventionally produced material. Hence, precipitation was hindered near the platform in the T_{P500} specimen, as the nominal $T_P > M_S$. It could be possible, however, that the nominal T_P was not reached at the platform surface. If $M_f < T_N < M_S$, precipitation could have occurred in the martensite phase and simultaneously been suppressed in the austenite phase. As a result, the hardness near the platform was high, but the number density and size of precipitates was small. However, the conditions during LPBF (i.e. rapid cooling from the melt and IHT) could not be reproduced with dilatometry.
- The longitudinal compression in voltage-based reconstructions with $k_f = 3.3$ could have been caused by the heat input during laser-mode APT. The evaporation fields of individual

6 Conclusions

species may have been lower than the IVAS database suggested. An adjustment to $k_f = 4.0$, which was determined to be in accordance with the tip profile-based reconstruction using a SEM image, could account for the temperature increase at the tip apex.

- In the *Tpnone* specimen, nm-sized *Si*-oxides were found. After adjusting k_f , they attained a globular shape in the reconstruction.

Although there were no precipitates in the *Tpnone* specimen, it cracked during LPBF. This suggests that precipitation is not the main reason for cracking.

7 Outlook

Of the four possible reasons for cracking during LPBF of the investigated FeCoMo alloy (i.e. coarse grains from epitaxial growth, brittle ordering phase, in-process μ -phase precipitation and embrittlement by *Si*-oxides), the precipitation behaviour during LPBF was investigated with APT. The absence of brittle ordering phase in the as-built condition has already been proven with previous DSC measurements [8]. The results of this thesis showed that in-process precipitation occurs with platform preheating of 500 °C. However, when no preheating was applied, the driving force from IHT did not suffice to form precipitates with enough *Mo*-content to visualise them with *Mo*-isosurfaces in the APT reconstruction. Although no precipitates were found without preheating, the specimen still cracked during LPBF. Hence, it is assumed that the μ -phase precipitates are not the main reason for cracking. In order to produce crack-free LPBF parts from the investigated FeCoMo alloy, it will be attempted to use *Si*-free powder. The assumption is that the occurrence of *Si*-oxides and their embrittling effect can be avoided. By adjusting the parameters of the LPBF process, strongly pronounced epitaxial growth could be minimised, which could result in smaller grain sizes and prevent transgranular fracture. Applying preheating temperatures $T_P \gg M_S$ could prevent martensite formation and hence precipitation during LPBF, however, preheating above 200 °C is not yet practical in the industry [66].

Because LPBF exposes the material to previously unconventional conditions, the problems arising during the process also require unconventional solutions. Although metal-AM opens the door to potentially industry-reforming possibilities, a lot of research still has to be done to make it applicable for a wide range of materials.

References

- [1] D. Gu, *Laser additive manufacturing of high-performance materials* (Springer, Germany, 2015).
- [2] J. O. Milewski, *Additive manufacturing of metals* (Springer, Switzerland, 2017).
- [3] G. A. Roberts et al., *Tool steels* (ASM International, USA, 1998).
- [4] W. Sha et al., *Maraging steels - modelling of microstructure, properties and applications* (Woodhead Publishing in Materials, USA, 2009).
- [5] J. Martin, *Precipitation Hardening* (Reed Elsevier, UK, 1998).
- [6] W. Betteridge, *Cobalt and its alloys* (Ellis Horwood Limited, UK, 1982).
- [7] Y. Geller, *Tool steels* (Mir Publishers Moscow, Russia, 1978).
- [8] D. Rainer, "Bachelor thesis, Montanuniversität Leoben", 2020.
- [9] W. Bleck, *Spezielle Werkstoffkunde der Stähle* (Springer, Germany, 2009).
- [10] H.-E. Arntz et al., *Werkstoffkunde Stahl Band 2: Anwendung* (Verein Deutscher Eisenhüttenleute, Germany, 1985).
- [11] H. Danninger et al., "Powder metallurgy carbon free tool steels Fe-Co- Mo with varying Co and Mo contents", *Powder Metallurgy Progress*, 47–56 (2013).
- [12] J. W. Cahn, "On spinodal decomposition", *Acta Metallurgica*, 795–801 (1961).
- [13] J. W. Cahn, "On spinodal decomposition in cubic crystals", *Acta Metallurgica*, 179–183 (1962).
- [14] J. S. Langer, "Theory of spinodal decomposition in alloys", *Annals of Physics*, 53–86 (1971).
- [15] J. S. Langer et al., "New computational method in the theory of spinodal decomposition", *Physical Review A*, 1417–1429 (1975).
- [16] J. W. Cahn, "The later stages of spinodal decomposition and the beginnings of particle coarsening", *Acta Metallurgica*, 1685–1692 (1966).
- [17] T. Miyazaki et al., "The phase decomposition of iron-molybdenum binary alloys by spinodal mechanism", *Acta Metallurgica*, 1143–1153 (1979).
- [18] M. Doi et al., "Development of ultra high strength steels based on spinodal decomposition", *Journal of Materials Science*, 1328–1334 (1987).
- [19] T. Kozakai et al., "Spinodal decomposition in Fe-Mo-Co and Fe-Mo-V ternary systems", *Transactions ISIJ*, 159–164 (1985).
- [20] T. Massalski et al., *Binary alloy phase diagrams: Volume 1* (American Society for Metals, USA, 1986).
- [21] T. Massalski et al., *Binary alloy phase diagrams: Volume 2* (American Society for Metals, USA, 1986).

References

- [22] W. Köster et al., “Das System Eisen-Kobald-Molybdän”, *Archiv für das Eisenhüttenwesen*, 627–630 (1932).
- [23] C. Turk, “Ausscheidungshärtbarer Schneidwerkstoff mit Hartphasen”, PhD thesis (Montanuniversität Leoben, 2016).
- [24] G. Raynor et al., “Critical evaluation of ternary alloys of iron and molybdenum with cobalt, chromium, manganese, and nickel”, *International Metals Reviews*, 329–376 (1984).
- [25] V. Brostrom et al., “The alloying of high-speed alloys hardened with intermetallics”, *Metal Science and Heat Treatment*, 32–37 (1970).
- [26] A. Edneral et al., “Effect of cobalt on aging of martensite and ferrite in Fe-Co-W and Fe-Co-Mo alloys”, *Metal Science and Heat Treatment*, 840–843 (1974).
- [27] W. Sha et al., “Phase chemistry and precipitation reactions in maraging steels”, *Metallurgical and Materials Transactions A*, 1251–1256 (1993).
- [28] F. Cajner et al., “Surface modifications of maraging steels used in the manufacture of moulds and dies”, *Materials and Technology*, 85–91 (2010).
- [29] I. Gibson et al., *Additive manufacturing technologies* (Springer, USA, 2015).
- [30] C. Li et al., “Residual stress in metal additive manufacturing”, *Procedia CIRP*, 348–353 (2018).
- [31] W. E. Frazier, “Metal additive manufacturing: a review”, *Journal of Materials Engineering and Performance*, 1917–1928 (2014).
- [32] W. Beard et al., “Fatigue performance of additively manufactured stainless steel 316L for nuclear applications”, *Conference: 30th Annual International Solid Freeform Fabrication Symposium*, 2144–55 (2020).
- [33] T. Allam et al., “Tailoring the nanostructure of laser powder bed fusion additively manufactured maraging steel”, *Additive Manufacturing*, 101561 (2020).
- [34] M. Glicksman, *Principles of solidification* (Springer, USA, 2011).
- [35] K. Sofinowski et al., “Layer-wise engineering of grain orientation (LEGO) in laser powder bed fusion of stainless steel 316L”, *Additive Manufacturing*, 101809 (2021).
- [36] R. R. Dehoff et al., “Site specific control of crystallographic grain orientation through electron beam additive manufacturing”, *Materials Science & Technology*, 931–938 (2015).
- [37] H. Helmer et al., “Grain structure evolution in Inconel 718 during selective electron beam melting”, *Materials Science and Engineering A*, 180–187 (2016).
- [38] K. Kempen et al., “Producing crack-free, high density M2 HSS parts by selective laser melting: pre-heating the baseplate”, *24th International Solid Freeform Fabrication Symposium*, 131–139 (2013).

References

- [39] C. Tan et al., “Microstructural evolution, nanoprecipitation behavior and mechanical properties of selective laser melted high-performance grade 300 maraging steel”, *Materials and Design*, 23–34 (2017).
- [40] R. Casati et al., “Aging behaviour and mechanical performance of 18-Ni 300 steel processed by selective laser melting”, *Metals*, 218 (2016).
- [41] E. Jäggle et al., “Precipitation and austenite reversion behavior of a maraging steel produced by selective laser melting”, *Journal of Materials Research*, 2072–2079 (2014).
- [42] A. Jarfors et al., “On the nature of anisotropy of maraging steel (1.2709) in additive manufacturing through powder bed laser-based fusion processing”, *Materials and Design*, Article in Press (2021).
- [43] W. Lefebvre-Ulrikson et al., *Atom probe tomography - put theory into practice* (Elsevier, UK, 2016).
- [44] B. Gault et al., *Atom Probe Microscopy* (Springer, USA, 2012).
- [45] M. K. Miller et al., *Atom-probe tomography: the local electrode atom probe* (Springer, USA, 2014).
- [46] L. Rigutti, “Laser-assisted atom probe tomography”, *Advances in Imaging and Electron Physics*, 29–53 (2019).
- [47] G. S. Gipson, “An improved empirical formula for the electric field near the surface of field emitters”, *Applied Physics*, 3884–9 (1980).
- [48] D. R. Kingham et al., “Some predictions of a theory of post-ionization of field-evaporated ions”, *Surface Science*, L194–L198 (1981).
- [49] P. S. Technology, *Verfahren Plasmapolieren und Elektropolieren*, <https://www.plasotec.de/verfahren.html>, visited on March 26th, 2021.
- [50] M. Buhlert, *Elektropolieren - Elektrolytisches Glänzen, Glätten und Entgraten von Edelstahl, Stahl, Messing, Kupfer, Aluminium und Titan* (Eugen G. Leuze Verlag, Germany, 2009).
- [51] D. J. Larson et al., *Local electrode atom probe tomography - a user's guide* (Springer, USA, 2013).
- [52] Cameca, *LEAP 5000 Atom Probe*, <https://www.cameca.com/products/apt/leap-5000>, visited on September 10th, 2021.
- [53] E. Marquis et al., “Applications of atom-probe tomography to the characterisation of solute behaviours”, *Materials Science and Engineering R*, 37–62 (2010).
- [54] L. Stephenson et al., “New techniques for the analysis of fine-scaled clustering phenomena within atom probe tomography (APT) data”, *Microscopy and Microanalysis*, 448–463 (2007).

References

- [55] R. Hu et al., “Revealing Solute Clusters in Coalescence by Atom Probe Tomography Analysis”, *Microscopy and Microanalysis*, 1–9 (2020).
- [56] H. Leitner et al., “Precipitation behaviour of an Fe-Co-Mo-alloy during non-isothermal ageing”, *International Journal of Materials Research*, 367–374 (2008).
- [57] N. Haghdadi et al., “Additive manufacturing of steels: a review of achievements and challenges”, *Materials Science*, 1–44 (2020).
- [58] H. Alexander, *Physikalische Grundlagen der Elektronenmikroskopie* (Teubner Studienbücher, Germany, 1997).
- [59] D. Isheim et al., “Atomic-scale study of second-phase formation involving large coherency strains in Fe-20 at.% Mo”, *Scripta Materialia*, 645–651 (2000).
- [60] E. Eidenberger et al., “Spinodal decomposition in Fe-25 at.%Co-9 at.%Mo”, *Intermetallics*, 2128–2135 (2010).
- [61] P. Bajaj et al., “Steels in additive manufacturing: A review of their microstructure and properties”, *Materials Science and Engineering A*, 138633 (2020).
- [62] E. Stergar, “Influence of alloying elements on the precipitation behavior of an Fe-25 m%Co-15 m%Mo base alloy”, PhD thesis (Montanuniversität Leoben, 2010).
- [63] F. Huber et al., “Laser beam melting and heat-treatment of 1.2343 (AISI H11) tool steel – microstructure and mechanical properties”, *Materials Science and Engineering A*, 109–115 (2019).
- [64] G. Gottstein, *Physikalische Grundlagen der Materialkunde* (Springer, Germany, 1998).
- [65] L. Wei et al., “Thermal conductivity of metal powders for powder bed additive manufacturing”, *Additive Manufacturing*, 201–208 (2018).
- [66] L. Caprio et al., “Defect-free Laser Powder Bed Fusion of Ti-48Al-2Cr-2Nb with a high temperature inductive preheating system”, *Journal of Physics Photonics*, 1–26 (2020).

Appendix

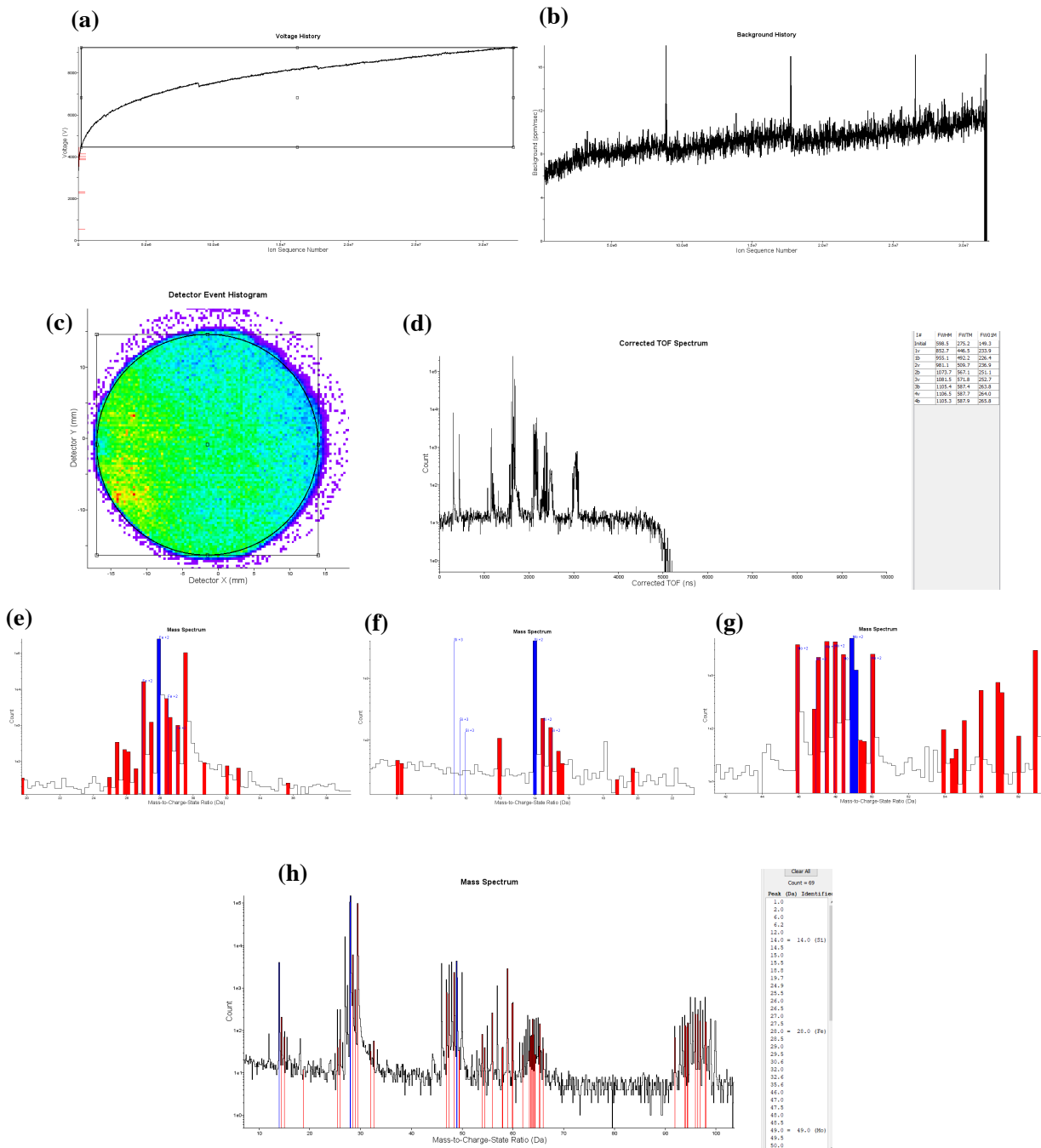


Figure 40: IVAS reconstruction wizard:

(a) Voltage and (b) background history during APT measurement, (c) detector event histogram, (d) TOF correction, (e–g) mass spectrum fitting: (e) Fe^{2+} , (f) Si^{2+} and (g) Mo^{2+} and (h) fitted mass spectrum.

Appendix

Table 6: Heat treatments and corresponding hardness.

	SA 1180 °C/10 min/ H_2O	Ageing 560 °C/3 h/air	Final condition	Hardness [HRC]	St. dev. [HRC]
HIP	no	no	normalised	40.2	0.31
HIP	yes	no	SA	43.8	0.25
HIP	yes	yes	SA and aged	68.0	0.05
$T_{Pnone300}$	no	no	as-built	40.0	0.56
$T_{Pnone300}$	yes	no	SA	45.0	0.33
$T_{Pnone300}$	no	yes	aged	67.3	0.14
$T_{Pnone300}$	yes	yes	SA and aged	68.3	0.33
T_{P50003}	no	no	$T_P = 500$ °C as-built	54.8	1.25
T_{P50003}	yes	no	$T_P = 500$ °C SA	44.8	0.17
T_{P50003}	no	yes	$T_P = 500$ °C aged	66.3	0.19
T_{P50003}	yes	yes	$T_P = 500$ °C SA and aged	68.9	0.08

Appendix

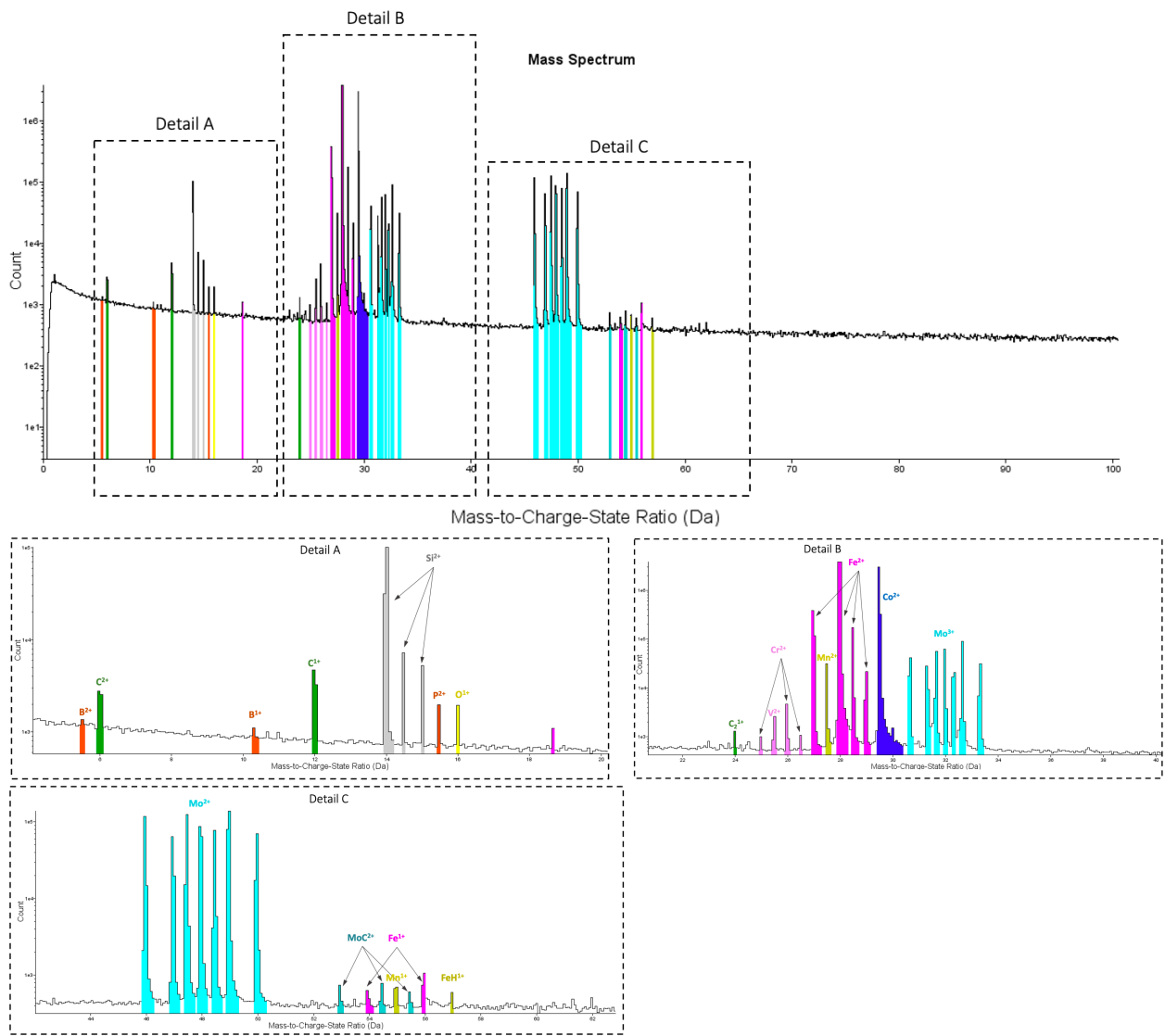


Figure 41: Ion species allocated to their corresponding peaks in the mass spectrum (voltage mode):
Mass spectrum overview and details A–C from the mass spectrum.

Appendix

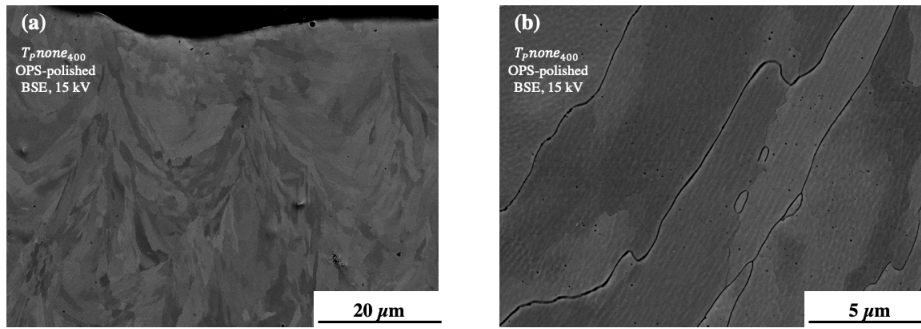


Figure 42: SEM micrographs of the as-built $TPnone_{400}$ specimen at the top layer, OPS-polished.

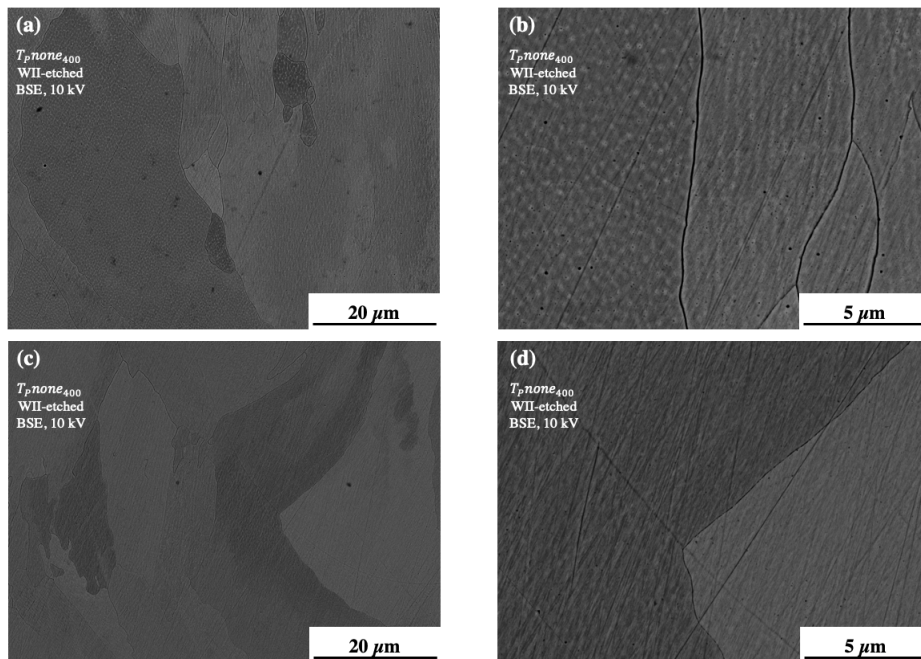


Figure 43: SEM micrographs of the as-built $TPnone_{400}$ specimen, etched with 20% WII.
(a, b) Top layer.
(c, d) Middle section.

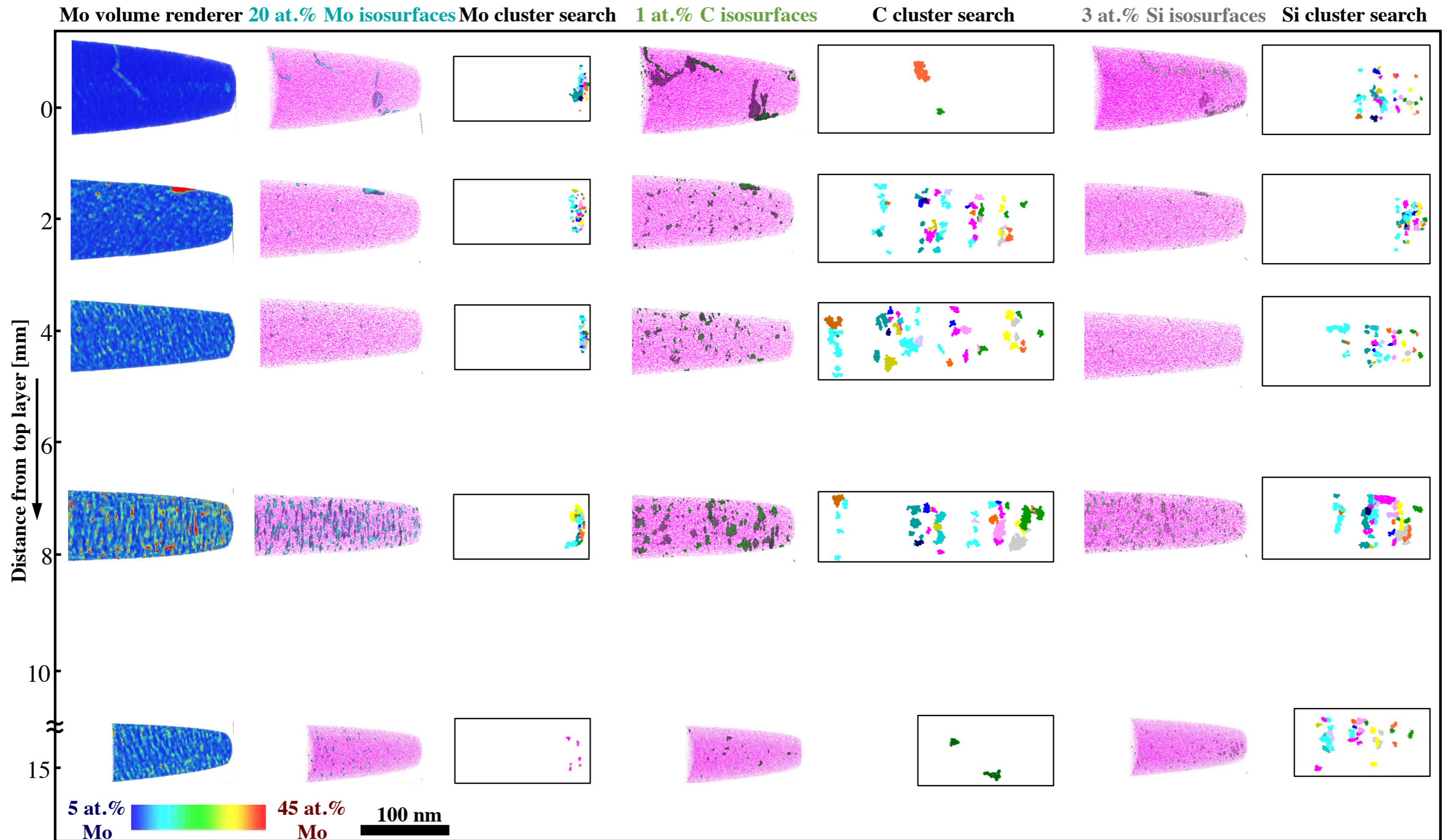


Figure 44: Results from the cluster search with the maximum separation algorithm for *Mo*, *C* and *Si* for the *Tp50003* specimen.

- 1st column: *Mo* volume renderer.
- 2nd column: 20 at.% *Mo* isosurfaces.
- 3rd column: Cluster search for *Mo*.
- 4th column: 1 at.% *C* isosurfaces.
- 5th column: Cluster search for *C*.
- 6th column: 3 at.% *Si* isosurfaces.
- 7th column: Cluster search for *Si*.